DISLOCATION DENSITY REDUCTION IN CADMIUM TELLURIDE AND MERCURY CADMIUM TELLURIDE GROWN ON SILICON USING THERMAL CYCLE ANNEALING

by

Stuart Bennett Farrell

A Dissertation
Submitted to the
Graduate Faculty
of
George Mason University
in Partial Fulfillment of
The Requirements for the Degree
of
Doctor of Philosophy
Physics

Committee:

Mulpuri, V. Rao — Dr. Rao V. Mulpuri, Dissertation Director

Yuri Mishin — Dr. Yuri Mishin, Committee Member

John Schreifels — Dr. John A. Schreifels, Committee Member

Gregory Brill — Dr. Gregory Brill, Committee Member

Michael E. Summers — Dr. Michael E. Summers, Department Chair

R Diecchio — Dr. Richard Diecchio, Associate Dean for Academic and Student Affairs, College of Science

Vikas Chandhoke — Dr. Vikas Chandhoke, Dean, College of Science

Date: April 26th 2011

Spring Semester 2011
George Mason University
Fairfax, VA

Dislocation Density Reduction in Cadmium Telluride and Mercury Cadmium Telluride Grown on Silicon Using Thermal Cycle Annealing

A dissertation submitted in partial fulfillment of the requirements for the degree of Doctor of Philosophy at George Mason University

By

Stuart Bennett Farrell
Master of Science
George Mason University, 2008
Bachelor of Science
Lynchburg College, 2001

Director: Dr. Rao V. Mulpuri, Professor
Department of Electrical and Computer Engineering

Spring Semester 2011
George Mason University
Fairfax, VA

Dedication

I dedicate this dissertation to my wife Ginger for all of her patience and support through this whole process.

Acknowledgments

I would like to acknowledge and thank all of those people who helped me through the process of this work. My adviser Dr. Mulpuri, for all of his support, help and patience throughout this process. Without his help and detailed reviewing all of my work and admittedly difficult writing style, I would never have been able to complete this. I wish to thank the other committee members Dr. Mishin and Dr. Schreifels for their help and comments.

I would also like to thank all of the people whom I have worked with at Army Research Laboratories for the various ways that they helped me with my research. Dr. Chen for teaching me MBE growth and sample characterization. Dr. Brill for being on my committee and for the many discussions and comments on my research and projects, also for all of the samples he provided for me to study. Dr. Dhar and Wijewarnasuriya for their help in efforts to make sure that I stayed on track and was continuing to be productive, among many other things.

I would like to thank the U.S. Army Research Office (ARO) who supported my work at George Mason University (GMU) under grant no. W911NF-07-2-0055 and also the Penn State Electro-Optics Center and K. Harris for the same.

Lastly to my wife and family for their support and encouragement while I worked so hard on completing this project.

Without the support of all of these people, this work would never have been possible.

Table of Contents

List of Tables

List of Figures

Abstract

DISLOCATION DENSITY REDUCTION IN CADMIUM TELLURIDE AND MERCURY CADMIUM TELLURIDE GROWN ON SILICON USING THERMAL CYCLE ANNEALING

Stuart Bennett Farrell, PhD

George Mason University, 2011

Dissertation Director: Dr. Rao V. Mulpuri

Mercury Cadmium Telluride (HgCdTe) is a material of great importance for infrared focal plane array applications. In order to produce large format detector arrays this material needs to be grown on a large area substrate, with silicon being the most mature substrate, it is the optimal choice for large format arrays. To help mitigate the effect of the lattice mismatch between the two materials, cadmium telluride (CdTe) is used as a buffer layer. The CdTe itself has nearly the same lattice mismatch (19.3%) to silicon, but due to the technological advantages it offers and compatibility with HgCdTe, it is the best buffer layer choice. The lattice mismatch between HgCdTe/CdTe and the silicon substrate leads to the formation of dislocations at densities in the mid 10^6 to low 10^7 cm^{-2} range in the epilayers. Such a high dislocation density greatly effects detector device performance quantities such as operability and sensitivity. Hence, the dislocation density should be brought down by at least an order of magnitude by adopting novel *in situ* and *ex situ* material processing techniques.

In this work, *in situ* and *ex situ* thermal cycle annealing (TCA) methods have been used to decrease dislocation density in CdTe and HgCdTe. During the molecular beam epitaxial (MBE) growth of the CdTe buffer layer, the growth was interrupted and the layer was subjected to an annealing cycle within the growth chamber under tellurium overpressure. During the annealing cycle the temperature is raised to beyond the growth temperature ($290 \rightarrow 550$ °C) and then allowed to cool before resuming growth again. This process was repeated several times during the growth. After growth, a portion of the material was subjected to a dislocation decoration etch in order to count the etch pit density (EPD) which has a direct correspondence with the dislocation density in the crystal. The crystalline quality was also characterized by x-ray diffraction rocking curves and photoluminescence. The *in situ* TCA resulted in almost a two order of magnitude reduction in the dislocation density, and factor of two reduction in the full width at half maximum of the x-ray rocking curves. Photoluminescence also suggested a decrease in the number of dislocations present in the material. This decrease is attributed to the movement of the dislocations during the annealing cycles and their subsequent interaction and annihilation.

To decrease the dislocation density in HgCdTe layers grown on CdTe/Si composite substrates, *ex situ* TCA has been performed in a sealed quartz ampoule under a mercury overpressure in a conventional clam-shell furnace. The reduction in the dislocation density has been studied as a function of growth/annealing parameters such as the initial (as grown) dislocation density, buffer layer quality, Hg overpressure, annealing temperature, annealing duration, and the number of annealing cycles. It was found that the primary parameters that affect dislocation density reduction are the annealing temperature and the number of annealing cycles. Some secondary affects were observed by varying the duration spent at the maximum annealing temperature. Parameters such as the initial dislocation density and buffer layer quality did not play a significant role in dislocation reduction. Though no correlation between Hg overpressure and dislocation density was

found, it did play a vital role in maintaining the quality of the surface.

By using the *ex situ* TCA, a dislocation density of 1×10^6 cm^{-2} could be reliably and consistently achieved in HgCdTe layers that had a starting density ranging from $0.5 - 3 \times 10^7$ cm^{-2}. Examination of the annealing parameters revealed an exponential decay in the dislocation density as a function of increasing number of annealing cycles. In addition, a similar exponential decay was observed between the dislocation density and the annealing temperature. The decrease in the dislocation density is once again attributed to moving dislocations that interact and annihilate. This behavior was modeled using a second order reaction equation. It was found that the results of the model closely agreed with the experimental values for a wide range of annealing temperatures and number of annealing cycles.

Chapter 1: Introduction

1.1 HgCdTe: Properties and Uses

HgCdTe is a highly desirable material for infrared (IR) detectors. It is often referred to as the third most studied semiconductor behind silicon and gallium arsenide. Despite the many competitors that can be used for infrared detectors, $Hg_{1-x}Cd_xTe$ has remained the dominant material of choice. $Hg_{1-x}Cd_xTe$ is an alloy of CdTe, which is a wide band gap semiconductor, and HgTe which is a semi-metal. By varying the mercury-cadmium ratios it is possible to tune the band gap from 0 to 1.5 eV, allowing for it to be used over a large spectral range. HgCdTe is almost ideal for IR detectors due to several key factors: (1) the ability to tune the band gap for sensing wavelengths from $1 - 30$ μm, (2) a direct band gap and high optical absorption coefficient both of which lead to a high quantum efficiency, (3) favorable inherent recombination mechanisms that lead to long carrier lifetimes and low thermal generation rates which reduce noise.

1.1.1 Infrared Detectors

The infrared wavelengths of light are those that fall between the visible and microwave spectra. Due to atmospheric absorption, the IR wavelengths are broken up into 3 general categories:

1. short wavelength infrared (SWIR): $1 - 3$ μm
2. middle wavelength infrared (MWIR): $3 - 5$ μm
3. long wavelength infrared (LWIR): $8 - 12$ μm

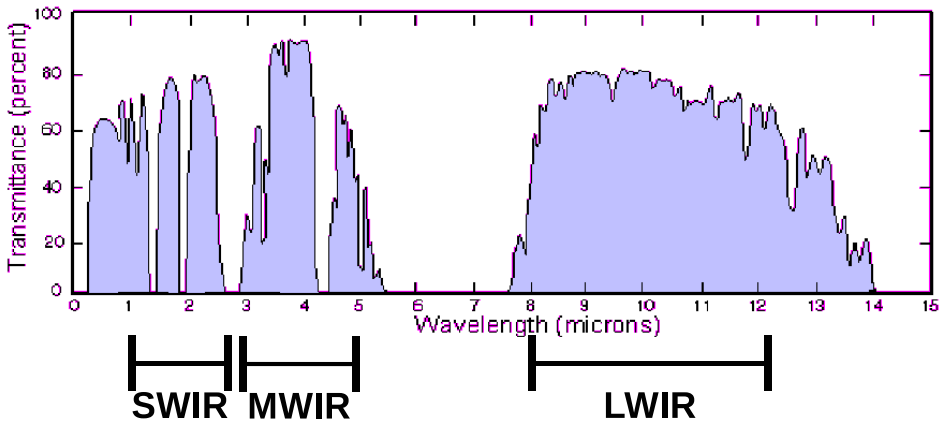

Figure 1.1: Chart of the transmission of the IR spectra through atmosphere with the regions of SWIR, MWIR, and LWIR note.

The atmospheric transmittance and regions of interest is shown are figure 1.1. Due to the transmittance profile, these three IR regions are the wavelengths of interest for IR detectors. Of particular interest in this work is the LWIR wavelengths. Objects at room temperature emit black body radiation in the $8-25$ μm range with a peak emission at ~ 9.5 μm. Thus, LWIR is the ideal range for thermal imaging (night vision) cameras. In addition, the LWIR wavelengths are particularly good at penetrating dust, smoke, fog and other vapor, making them the ideal wavelengths for astronomers, firefighters, and military personnel with a wide host of other uses.

The SWIR and the MWIR materials are ideally suited for detecting higher energy photons. The wider band gap of the materials leads to detectors with much less noise and they operate with lower leakage currents. LWIR detector materials have a narrower band gap, and hence are more susceptible to noise problems due to thermal generation and/or imperfections in the detector. This requires that high quality LWIR detectors be made of materials that are of the highest quality.

1.1.2 Substrate

Epitaxial semiconductor growth, in general, is ideally performed on a substrate that has perfect lattice constant and thermal expansion coefficient match with the epilayer. This allows for ease of growth and low defect density in the epilayer. The best substrate for $Hg_{1-x}Cd_xTe$ growth is a $Cd_{1-y}Zn_yTe$ substrate, where the zinc composition is chosen to yield a lattice constant that is matched to that of the HgCdTe ($y \approx 4\%$ for LWIR). While many properties of CdZnTe are ideal for HgCdTe growth, it has many mechanical properties that are far from ideal. CdZnTe substrates are very brittle and can be damaged very easily during handling. In addition, due to difficulties in the growth of high quality bulk CdZnTe crystals, substrates are prohibitively expensive and availability is limited. Another result of it's brittle nature and difficulty to grow, is that the size of the substrates is limited to a 6×6 cm square. The square shape causes difficulties in production because the majority of chip manufacturing apparatus are set up to handle circular wafers. Lastly the small size of the substrate limits the development of next generation photodetectors. For example Raytheon has developed a 256×2024 MWIR focal plane array (MWIR FPA), whose width is 6.5 cm and hence, simply cannot be made using CdZnTe substrates. Thus, it is necessary to move to a large area substrate for next generation commercial production.

For all the above mentioned reasons why CdZnTe is not an ideal substrate for growing HgCdTe, silicon is the ideal substrate. Silicon is cheap, robust, and large area, with 12 inch wafers being regularly used in chip manufacturing. However, the growth of HgCdTe material on Si has significant hurdles to overcome. Figure 1.2 shows the lattice constant and band gap of several semiconductor material systems. It can be seen that there is a large lattice mismatch between HgCdTe (6.48 Å) and silicon (5.43 Å). This is a lattice mismatch of $\sim 19.3\%$. As a direct result of this mismatch, HgCdTe layers grown using a Si substrates have a high dislocation density that impedes device performance and reduces uniformity among FPA pixels.

It has been shown by Johnson et al[1] that the resistance at zero bias times the junction

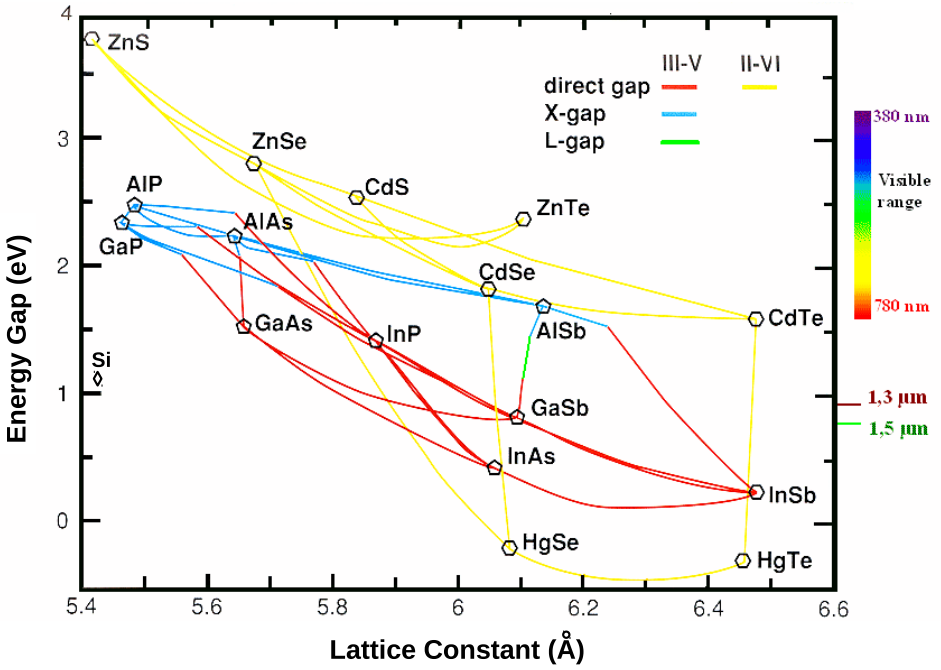

Figure 1.2: Variation of lattice constant with band gap for several materials and their alloys.

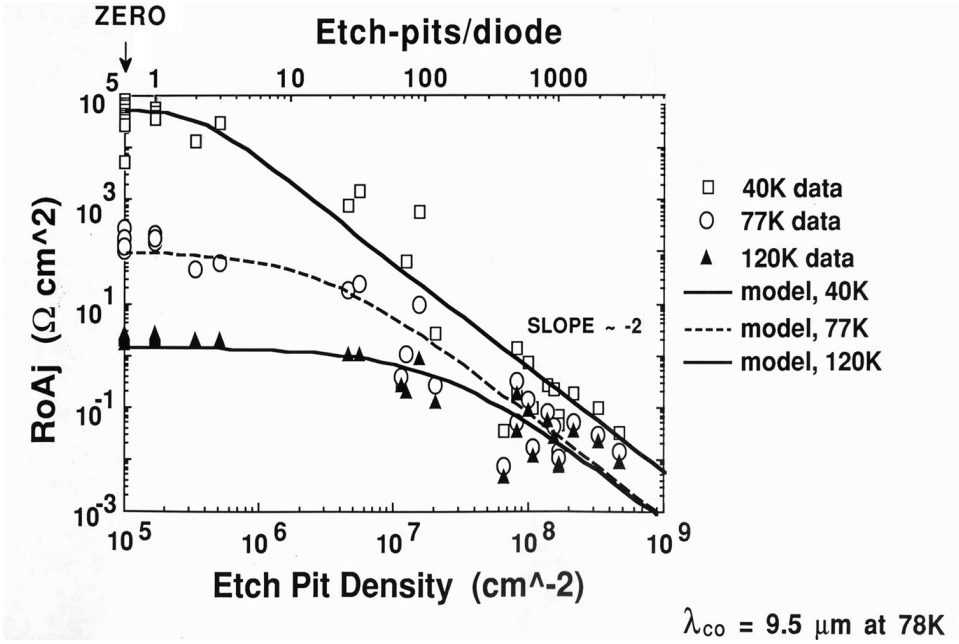

Figure 1.3: R_0A_j vs EPD, showing data measured from an array with a junction cut off of 9.5 μm. (From S. M. Johnson et al, 1992)

area (R_0A_j) of an LWIR FPA pixel is influenced heavily by the dislocation density (which is equivalent to the etch pit density), as shown in figure 1.3. This is believed to be directly related to the non-uniformity issue that impedes HgCdTe/Si LWIR-FPAs. The standard as grown dislocation density of HgCdTe on Si layers is $5 - 10 \times 10^6$ cm^{-2}, while layers grown on CdZnTe have a dislocation density of $0.5 - 5 \times 10^5$ cm^{-2}. The difference in R_0A_j for these two dislocation densities was measured to be roughly two orders of magnitude. The reduction in dislocation density of HgCdTe on Si to 1×10^6 cm^2 would result in an order of magnitude improvement in junction resistivity and thus, improve over all detector performance and uniformity to the point where it would be competitive with HgCdTe grown on CdZnTe substrates.

1.1.3 Molecular Beam Epitaxy Growth of HgCdTe

The HgCdTe and CdTe layers used for this work were grown by molecular beam epitaxy (MBE) on silicon substrates. A brief overview of the process of MBE growth is presented here. A substrate (Si or CdTe/Si in this case) is chemically cleaned and placed in an ultra high vacuum ($10^{-7} - 10^{-10}$ torr) growth chamber. Once in the growth chamber the surface is thermally cleaned and prepared prior to growth. The source materials for growth (CdTe, Cd, Te, Hg, etc) are heated to the point of sublimation. At these pressures the mean free path of an atom is on the order of several meters to several kilometers, so that the sublimating material can be considered to be a beam of non-interacting particles. These beams are directed onto the substrate where the atoms stick and under proper conditions results in the growth/deposition of a single crystal layer. By varying the temperature of the source materials the flux of particles can be controlled. This allows the growth rate to be varied and controlled from as low as several monolayers per second up to several microns per hour.

The preferred orientation for MBE growth of HgCdTe is on the (211) plane. This orientation is superior to the lower index planes for a couple of reasons. Growth on lower

index planes, such as (100) and (111), often leads to twinning and double domains which are a form of 2 and 3 dimensional defects, that limit device performance. Twinning problems can often be mitigated by growing on substrates that are slightly off-cut/tilted ($1 - 5$ °) from the true orientation[2]. Another issue with low index planes is that the Hg sticking coefficient (flux verses amount deposited) is very low on the lower index planes. This means that a very high Hg flux is required for growth and, thus, several more complications arise. Additionally, doping was found to be easier to control for growth on higher index planes.

The samples are removed after growth and characterized by several different means. Fourier transform infrared spectroscopy (FTIR) is used to measure the layer thickness via fringe patterns formed by the interfaces. The surface is characterized using Nomarski optical microscopy to determine the concentration of defects such as voids, micro voids, and other various surface defects as well as examining the overall surface morphology that is indicative of good growth. Further characterization of the crystal quality using x-ray diffraction and/or etch pit density (EPD) is also performed.

1.1.4 Summary of Materials Used

For the sake of brevity and clarity, the following presents a summary of some of the general characteristics of materials and layers used throughout the experimentation presented in this work. (Particulars and explanations of the concepts and relevance's within are deferred to latter sections.)

Substrate

The substrates used were 3 inch p-type (211) silicon. The substrates have a nominal (± 0.5 °) off cut, have a resistivity of $1 - 15$ Ω/cm, and are 500 μm thick. Some experiments were performed with layers grown on lattice matched CdZnTe substrates, and are noted as such in the text.

Buffer Layers

The majority of buffer layers used are MBE grown CdTe. The CdTe layers are undoped and $8-10$ μm thick. The layers have an EPD ranging from $0.5-30\times10^6$ cm^{-2}, with the majority of layers in the low 10^6 cm^{-2} range. X-ray rocking curves have a FWHM in the range of $50-200$ arcsec.

$Cd_{1-x}Se_xTe$ buffer layers were frequently used as well. They have a Se composition of $\sim 4\%$ as measured by x-ray diffraction. The Se composition is tailored to be lattice matched to LWIR HgCdTe. Due to the lack of a reliable EPD etch for CdSeTe, the EPD is unknown, but x-ray FWHM values are a bit higher but comparable to the CdTe buffer layers.

HgCdTe

The majority of $Hg_{1-x}Cd_xTe$ layers used in this study are of a composition suited for LWIR ($x\approx0.2$) applications, with thicknesses ranging from $8-12$ μm. The Layers have a MWIR cap layer that is ~ 0.2 μm thick (this layer is thin enough that it's effects can be ignored). Layers are n-typed doped *in situ* with indium, concentrations range from $10^{14}-10^{16}$ cm^{-3}. Several MWIR ($x\approx0.33$) and SWIR ($x\approx0.4$) layers are also used, and are noted where relevant through out the text.

Chapter 2: Crystal and Dislocation Structure

2.1 Crystal Lattice

The ideal crystal is a periodic arrangement of atoms in a lattice. Though there are many different lattice structures, the CdTe and HgCdTe crystal have the zincblende structure. In this chapter the simple cubic model is also included due to it being the simplest, and is very useful for discussing dislocations and other basic aspects of crystallography. The face centered cubic (FCC) lattice will also be discussed because it's simplicity lies between the zincblende and the simple cubic, it shares many properties of both types of lattices without becoming overly complicated. Zincblende is the lattice type of CdTe, HgCdTe and their alloy HgCdTe, in addition Si is a special case of this lattice with all atoms being of the same type and is called the diamond lattice.

In a perfect lattice there are no missing atoms, substituted atoms, or extra atoms in the interstitial positions present in the lattice. However a perfect lattice structure does not exist in any semiconductor system. All crystals contain defects, both point and line type. During growth, the bulk of the semiconductor crystals has several trace impurities enter in to the crystal through the source materials and growth method that is used. Also point defects such as vacancies, interstitial and substitutions exist with in the crystal. Finally, it is impossible to perfectly form an extended crystal lattice, and thus dislocations and other extended defects will also be present.

2.1.1 Simple Cubic Lattice

The simple cubic lattice is a Cartesian lattice. An atomic position is located at the integer coordinates in 3 dimensions. Because every point in a crystal looks the same as any other

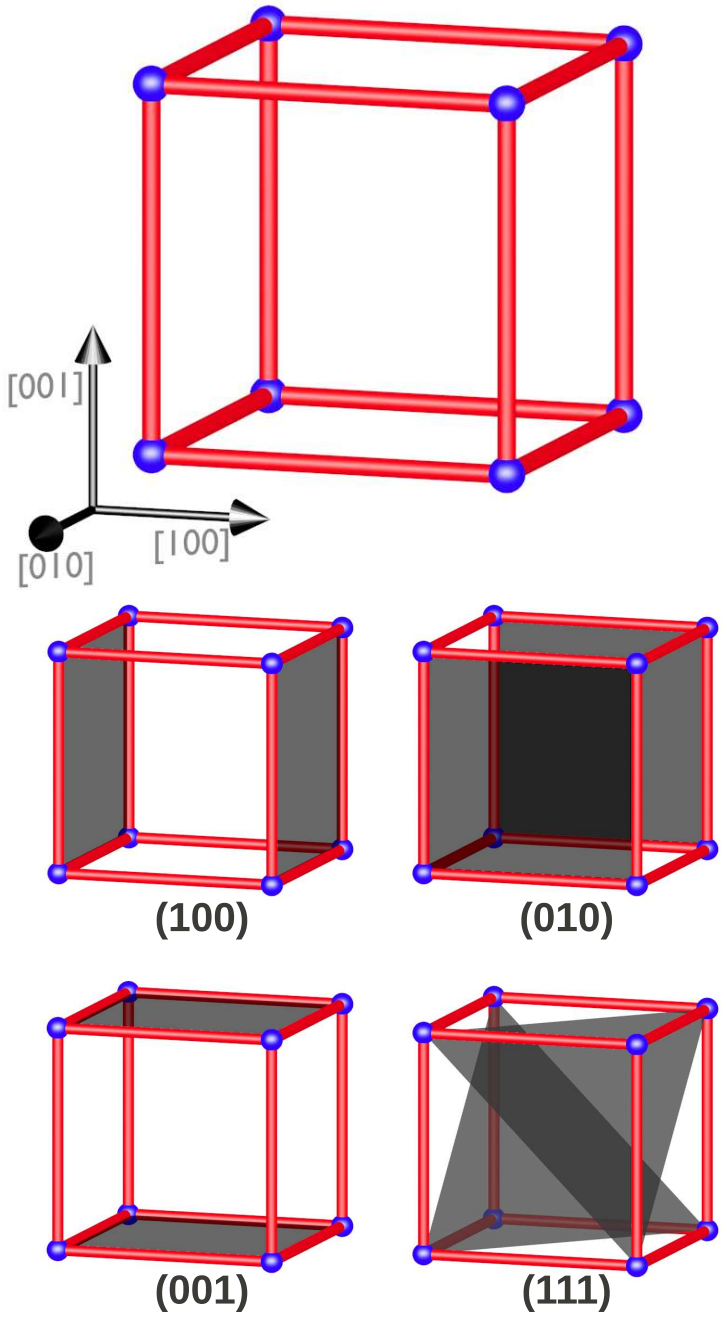

Figure 2.1: A diagram of a simple cubic unit cell with the basis vectors labeled, and several examples crystal planes.

point, the positions of the atoms themselves are irrelevant, but rather crystallographic directions and planes within the crystal are referenced. The unit cell is the simplest form of a lattice. The unit cell can be stacked in repeated arrangements to make the full crystal structure, the unit cell of a simple cubic lattice is shown in figure 2.1. Standard convention labels the x, y, and z directions as [100], [010], and [001] respectively. Generalizing these results, an arbitrary vector in a cubic system is denoted as $[hkl]$ and is the vector $h\hat{x}+k\hat{y}+l\hat{z}$. Lattice planes are denoted with reciprocal space vectors. The plane (hkl) is the plane that intersects the positions located at $\frac{1}{h}\hat{x}$, $\frac{1}{k}\hat{y}$ and $\frac{1}{l}\hat{z}$, in the case of a cubic systems any given lattice vector is normal to a lattice plane with the same indices. This notation of lattice vectors and planes is called *Miller indices*, and by convention lattice vectors are denoted with square brackets, $[hkl]$, and planes with round brackets, (hkl). If lattice vectors or planes are equivalent by symmetry, then they are said to be part of the same *family*. A family of lattice vectors or planes are denoted with angle brackets, $\langle hkl \rangle$, and curly brackets, $\{hkl\}$, respectively. Also by convention negative numbers are denoted by a bar (ie $\bar{h}$) rather than with a negative sign.

2.1.2 Face Centered Cubic Lattice

The FCC lattice structure is pictured in figure 2.2. As it's name suggests, it is the same as the simple cubic lattice but with additional atoms in the center of each of it's faces. Each lattice has a nearest neighbor that can be found at $a/2\langle 110 \rangle$, where a is the length of the sides of the cube (also known as the lattice constant). The FCC is known as a close packed structure, the arrangements of the atoms is such that they are as tightly packed as it is possible to pack a set of hard spheres. Figure 2.3 shows an FCC crystal with a cut showing the close packed $(11\bar{1})$ plane. For several applications it is useful to think of the zincblende lattice as an FCC lattice.

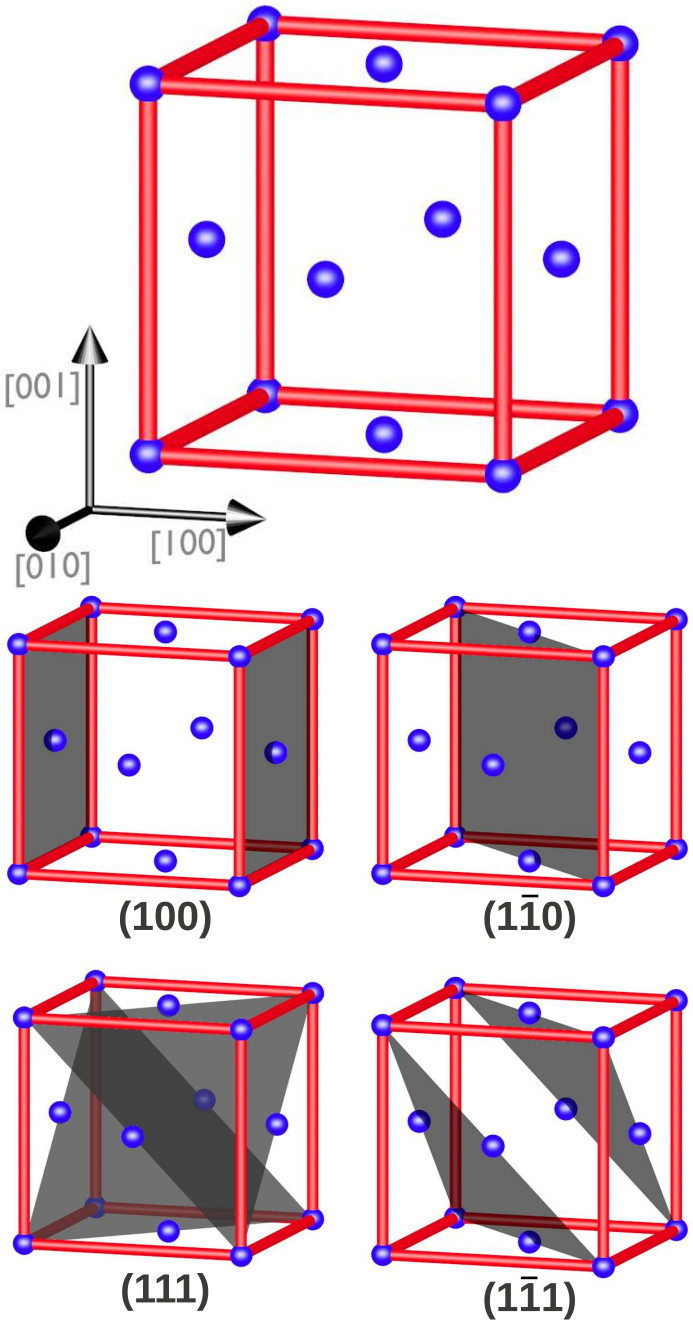

Figure 2.2: A diagram of the FCC unit cell with the basis vectors labeled, and several examples crystal planes.

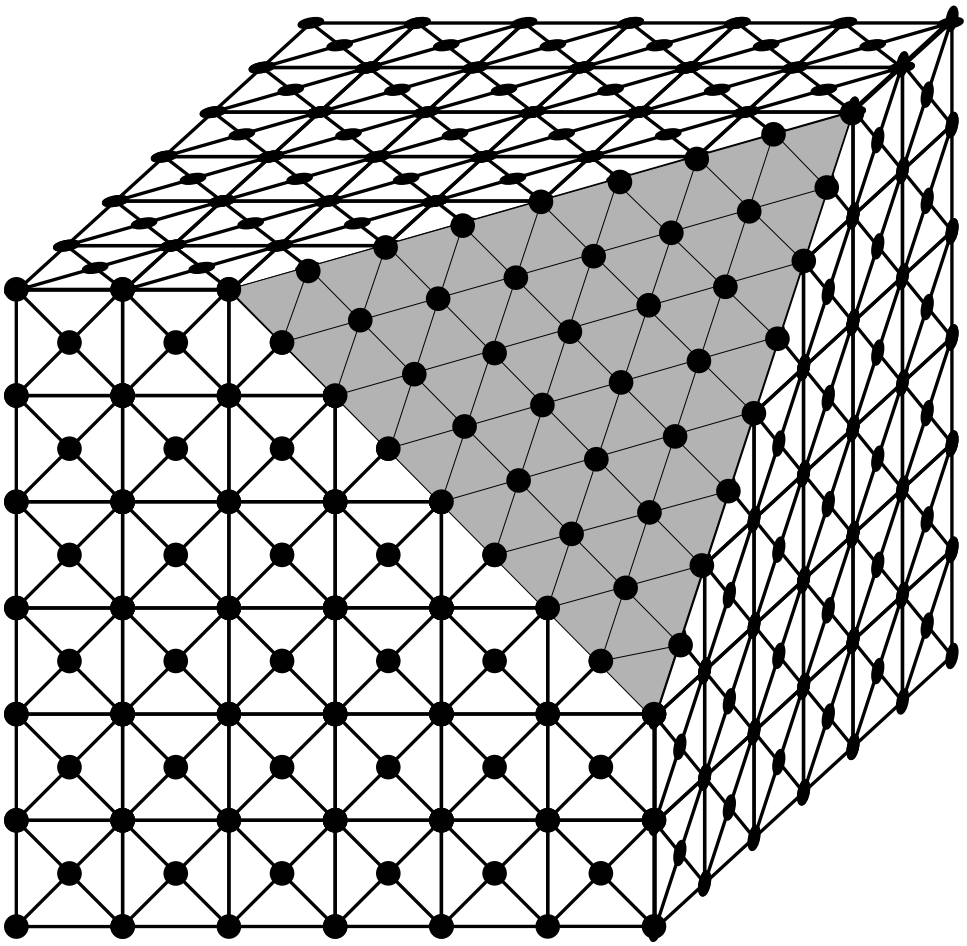

Figure 2.3: A diagram of an FCC lattice with a cut along {111} plane to show the the close packed plane.

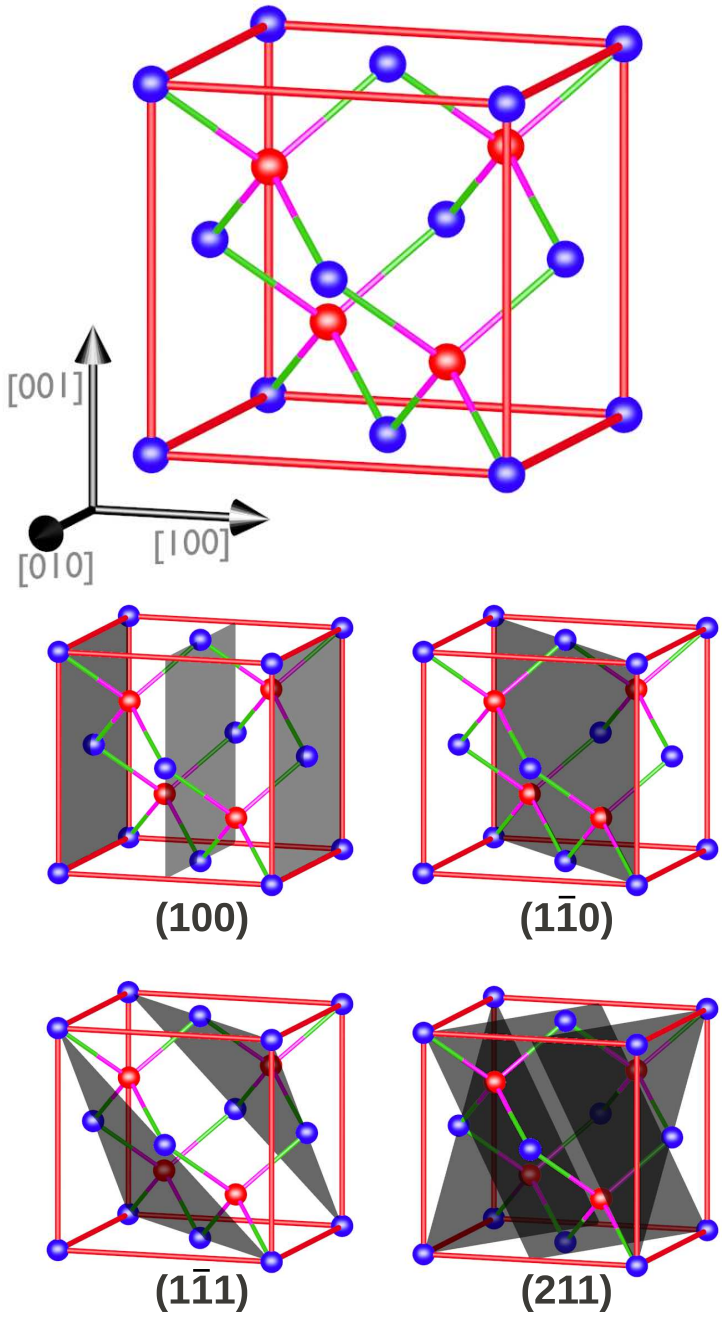

Figure 2.4: A diagram of the zincblende unit cell with the basis vectors labeled, and several examples crystal planes.

2.1.3 Zincblende Lattice

CdTe and HgTe have a zincblende lattice. The simplest way to understand this lattice is either to overlay a Cd/Hg FCC lattice with a Te FCC lattice and offset one of the lattices by $a/4\hat{x} + a/4\hat{y} + a/4\hat{z}$, or by placing 4 Te atoms in the appropriate position in the interior. The basic zincblende structure is shown in figure 2.4 The atomic bonds that hold the crystal together are between the Cd/Hg and Te atoms. Thus, each of the Cd/Hg atoms are bonded to 4 Te atoms, and each Te atom is bonded to 4 Cd/Hg atoms. In the case of HgCdTe, we will find a portion of the Cd atoms replaced with Hg atoms.

The silicon substrates used in the growth of HgCdTe have a diamond lattice. This can be considered to be a special form of the zincblende structure. In this case both of the interpenetrating FCC lattices are composed of the same element. Thus, the two lattices are compatible.

2.2 Point Defects

The first and simplest of the imperfections that can exist in a lattice are known as point defects. There are several different types of point defects that will be briefly described here, namely: interstitials, vacancies, substitutions, and impurities.

An interstitial defect is an atom with in the crystal lattice that does not reside at a proper lattice position, but rather is found in the empty space between lattice points. A vacancy is when a lattice cite that normally has an atom is empty, thus the lattice cite is vacant. These types of defects are often created and annihilated in pairs, where an atom migrates away from it's position as an interstitial and leaves behind a vacancy. These forms of defects are an unavoidable result of any thermal treatment. As a result of a high temperature anneal, many of the atoms will escape their bonds to a lattice and become vacancy-interstitial pairs.

In HgCdTe, the majority of interstitial and vacancies are a result of the Hg atoms. The interstitials that are formed are very mobile, and will quickly travel to the surface of the

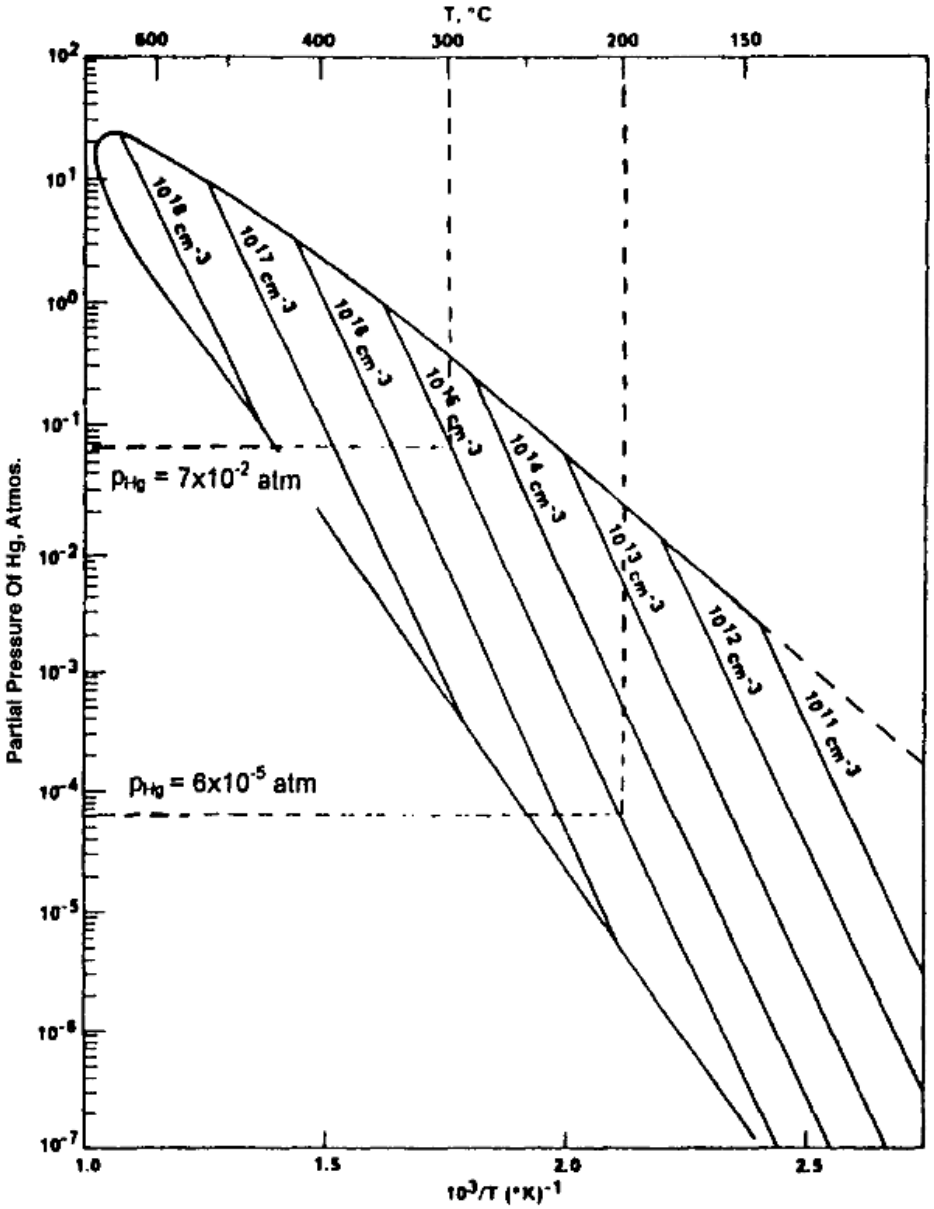

Figure 2.5: P-T curve and isohole concentration lines for $Hg_{0.8}Cd_{0.2}Te$ from $T = 150 \rightarrow 655$. The upper bound of the curve represent the Hg vapor pressure, while the lower bound represents the lower limit of Hg overpressure needed to maintain the crystal structure. (From Vydyanath and Hiner, 1989)

sample and out diffuse as Hg vapor, thus at high temperature there will be a high concentration of vacancies, but only an insignificant number of interstitials[3,4]. If the interstitials are not allowed to leave the crystal by either a cap layer or high Hg overpressure, then they will move though out the crystal and fill in vacancies. Thus the vacancy concentration will be lower when a sample is annealed in the presence of a high Hg over pressure. The equilibrium vacancy concentration for HgCdTe for any given temperature and pressure is shown in figure 2.5[5].

The other two forms of point defects are of much less importance, namely substitutions and impurities. Substitutions are when a tellurium atom sits in a mercury position and vice versa. These sorts of defects are rather rare in HgCdTe due to their highly ionic nature. Impurities in a lattice occur when a foreign atom resides in the lattice. These are generally in the form of dopants, and are incorporated in the lattice on purpose. The common dopants for HgCdTe are indium for n-type and arsenic for p-type doping.

2.3 Dislocation Properties

A dislocation is caused by a deformation of the crystal lattice. The deformation consist of areas of *plastic deformation*, where the lattice bonds are broken and reattach at an other location, and *elastic deformation*, where the lattice bonds are strained and distorted but not broken. The line about which the plastic deformation of the lattice occurs is called the dislocation line vector. Dislocation types can be divided in to three different categories: **edge type**, **screw type**, and **mixed**.

2.3.1 Dislocation Types: Screw, Edge, Mixed

The formation of edge dislocations can be visualized by making a cut in a perfect crystal and either inserting or removing a half plane of material, the latter case is pictured in figure 2.6 (a). After the half plane is removed, the area around the missing portion of the crystal is joined together. This results in a strained region around the edge of the half plane that

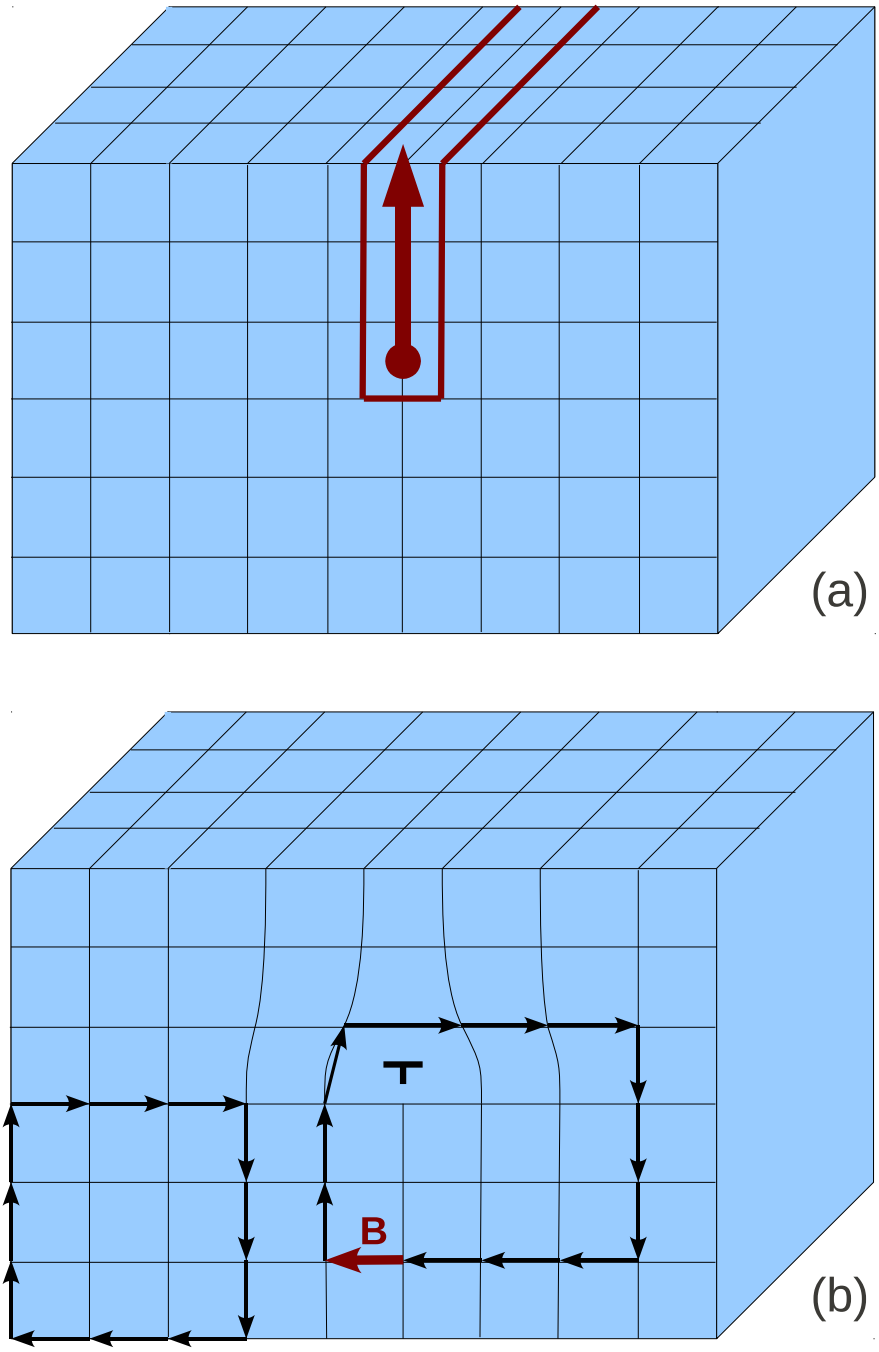

Figure 2.6: Diagram of an edge dislocation being formed by removing a half plane of atoms. Burgers circuit around an un-dislocated section and around the dislocation are shown to illustrate the Burgers vector. Note that the dislocation vector is perpendicular to the Burgers vector in the case of an edge dislocation.

remained in the crystal, with the dislocation line extending from one end of the crystal to the other along the edge of the half plane. Figure 2.6(b) shows the resulting structure of an edge dislocation. Symbolically, edge dislocations are commonly denoted by the symbol "⊥" pointing in the direction of the extra half plane or away from the missing half plane.

If a cut is made in a perfect crystal, and a shear stress is applied as shown in figure 2.7(a), the result is a screw dislocation. In this case the dislocation line follows the strained region along the edge of the cut. The dislocated planes are no longer strictly parallel to each other but rather have a screw shape, this can be pictured to be like a parking deck with each successive loop made around the dislocation line arriving at a level above the starting point. A diagram of the structure of a screw dislocation is shown in figure 2.7(b).

The last type of dislocation is the mixed dislocation. A mixed type dislocation is the combination of a screw and edge type. It is not as simple to describe as the edge and screw type, and it is the opinion of the author that it is more easily understood mathematically than visually. While the dislocation line can be easily understood as the vector along which the crystal is strained, a different vector is needed to characterizes the direction of strain in the dislocation. For this the concept of the Burgers vector is needed.

2.3.2 Burgers Vector

The Burgers vector of a dislocation is indicative of the direction of the deformation that forms the dislocation. The Burgers vector can be determined by comparing a path traced around the dislocation to a path traced around a perfect crystal. The vector needed in order to complete the circuit around the dislocation compared to the same path around the perfect crystal is called the the Burgers vector; examples of such paths can be seen in figures 2.6(b) and 2.7(b). The direction that the Burgers circuit is traced around the dislocation does not matter, but the circuit direction must be consistent through out the analysis, the paths in figures 2.6(b) and 2.7(b) were both traced clock-wise around the dislocation line. The fundamental difference between a screw and edge dislocation is the direction of the Burgers vector compared to the line vector. In the case of a screw dislocation, the

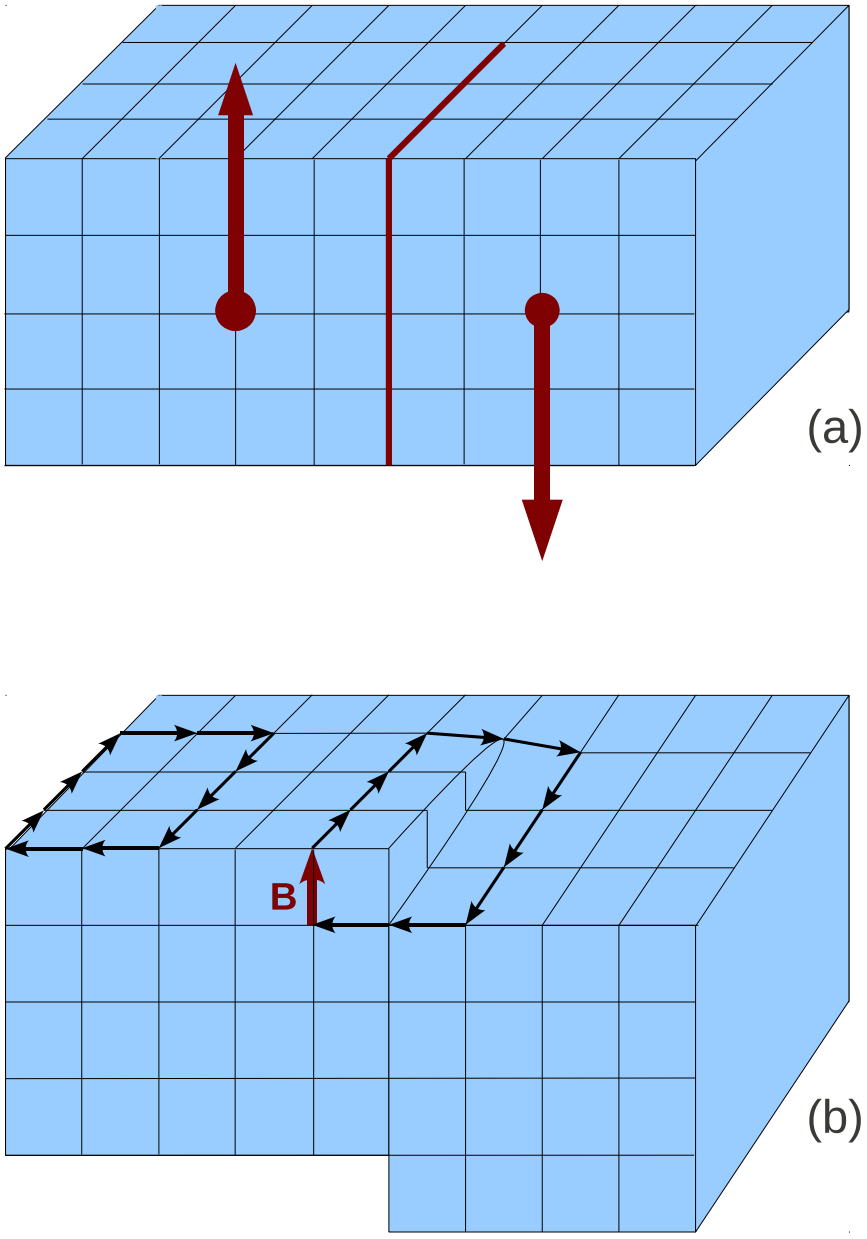

Figure 2.7: Diagram of a screw dislocation being formed by making a cut and exerting a sheer stress around the cut. A Burgers circuit around an un-dislocated section and around the dislocation are shown to illustrate that the Burgers vector is parallel to the dislocation vector in the case of a screw dislocation.

Burgers vector and line vector are parallel, and in the case of an edge dislocation they are perpendicular. A mixed dislocation has a line vector and Burgers vector that are neither parallel nor perpendicular but of some angle in between. In an FCC and zincblende crystal one of the most common types of dislocations is the 60 ° dislocation where the dislocation line is in the $\langle 110 \rangle$ direction and has a burgers vector in the appropriate $a/2\langle 110 \rangle$ direction. For example a 60 ° dislocation with a line vector of $\vec{t} = [1\bar{1}0]$ has a Burgers vector of $\vec{b} = a/2[10\bar{1}]$.

2.3.3 Dislocation Motion

Dislocations can move by one of two means. These forms of motion are described as either being *conservative* or *non-conservative*. Conservative motion is the result of the shifting of atomic planes and causing the dislocation to glide from one atomic plane to another, hence it is also known as dislocation *glide*. Glide is the result of a stress being applied to the crystal and is pictured in figure 2.8. The motion results from a strain causing a slight deformation on the crystal and allowing the bonds around the dislocation to switch position. The amount of energy required to move the dislocation is equal to the amount of energy it takes to strain the crystal far enough that the bonds will reform. This sort of motion has a small temperature dependence, as the stress of deformation relates directly to the elasticity/hardness which vary with temperature.

Several factors govern glide type motion. Glide only occurs on *slip* planes. Slip planes are the highest density planes of the crystal, in the case of the simple cubic crystal this is the $\{100\}$ plane, for FCC and zincblende the slip planes are the $\{111\}$ plane. The glide direction normally takes the form of the more closely spaced atomic directions, in the case of simple cubic this remains in the $\langle 100 \rangle$ directions, but for FCC and zincblende materials this is the $\langle 110 \rangle$ directions. In order for dislocation glide to be possible, the line vector ($\vec{t}$) and the Burgers vector($\vec{b}$) must both lie on a slip plane. This means that edge dislocations that can move have a unique slip plane because the Burgers vector is always perpendicular

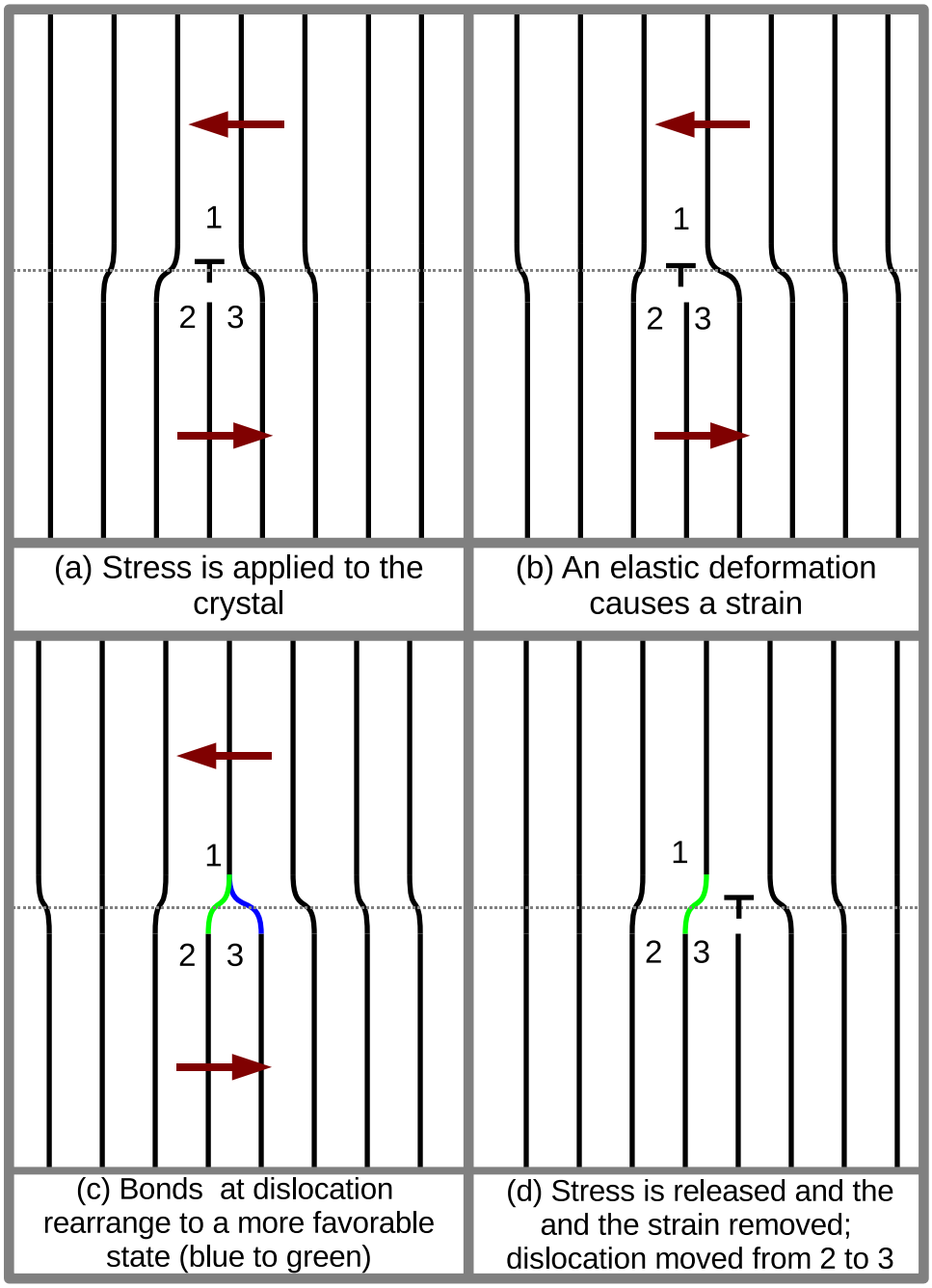

Figure 2.8: Diagram of how a dislocation (in this case pictured as an edge dislocation) glides from position 2 to 3 due to a stress placed on the crystal.

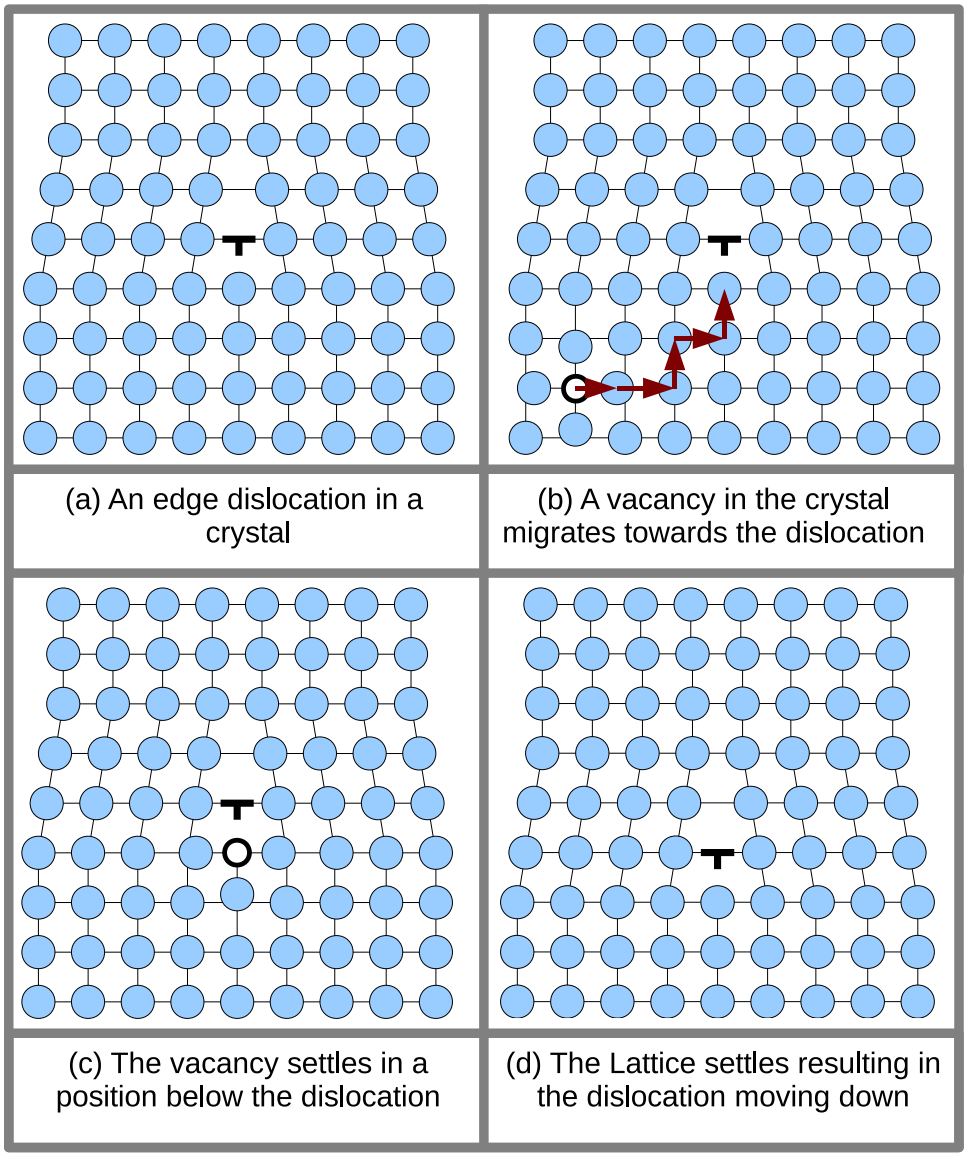

Figure 2.9: Diagram of how a dislocation moves from position 2 to 3 due to a stress placed on the crystal.

to the line vector. Likewise, mixed dislocations will have a unique slip plane due to the edge component of their Burgers vectors. On the other hand, the Burgers and line vector of a screw dislocation are parallel, thus, they do not have a well defined slip plane. This means that edge and mixed type dislocations can only move along a single vector if they can move at all, while screw dislocation can move in any close spaced vector.

Non-conservative motion of dislocations is called *dislocation climb* and is primarily caused by the dislocation interacting with point defects. Climb due to a vacancy is shown in figure 2.9. In this case, a vacancy within the crystal migrates into the position below the dislocation and effectively causes the dislocation to move down, this is referred to as *positive climb* because part of the half-plane that forms the dislocation is effectively being removed. The opposite effect could be achieved if an interstitial were to migrate to a position above the original dislocation position, this is referred to as *negative climb*. This sort of motion is highly temperature dependent, and is very weakly dependent on stress (i.e. the opposite of glide). At high temperatures and during rapid temperature changes point defects like interstitials and vacancies are mobile and will move throughout the crystal causing this form of dislocation motion (climb) to be common.

Positive climb occurs when a vacancy diffuses to the dislocation and annihilates an edge atom of the half plane, but it can also occur by that atom in the half-plane taking an interstitial position and diffusing away. Similarly, negative climb can be described as an interstitial diffusing towards the dislocation and adding to the half-plane or it can be described as an adjacent atom taking the edge location and the vacancy it leaves behind diffusing away. This mechanism is the reverse of what is depicted in figure 2.9. Therefore it can be generalized that dislocation climb generates or destroys point defects. Because the area around a dislocation is strained and often has a dangling bond, the energy necessary to form an interstitial-vacancy pair is less than in a perfect lattice. Thus, when point defect levels are not in equilibrium, generation of new point defects will occur preferentially at dislocations and induce climb.

For the case of HgCdTe, the dominant point defects are Hg vacancies. This is due to the high mobility of Hg interstitials, which have a diffusion activation energy of $0.54 - 0.61$ eV[6], and as a result diffuse out of the crystal as a gas when vacancy-interstitial pairs are formed within the crystal. The vacancy concentration is highly dependent on temperature, the vacancy concentration at a particular temperature is referred to as the equilibrium vacancy concentration. During the heating of a layer new vacancies need to be generated to

return the crystal to equilibrium. The generation of new vacancies causes a chemical force per unit length (f) on the dislocation[7, 8]

$$f = \frac{bk_bT}{\Omega} \ln\left(\frac{c}{c_0}\right), \tag{2.1}$$

where b is the edge component of the Burgers vector, k_b is Boltzmann's constant, T is temperature, Ω is the volume of a vacancy, and c and c_0 are the current vacancy concentration and equilibrium vacancy concentration respectively. Thus, the *chemical stress* on the dislocation is defined as f/b. Dislocation motion occurs when a stress greater than the *critical shear stress*, τ, is reached. For HgCdTe this has been demonstrated to be $\tau \approx 1.5 - 2.0$ MPa at 300 °C.[4] Solving for c/c_0 in equation 2.1, reveals that if the vacancy concentration is out of equilibrium by $\sim 0.2\%$, it will give rise to a large enough stress to induce dislocation climb. For the case of the annealing present later in this work, the temperature is increased from 250 to 500 °C linearly over 5 minutes. By using the isohole concentrations in figure 2.5 the chemical force can be calculated. This results in a rough estimate of the chemical force of 37 to 17 MPa over the course of the temperature change, much greater than the critical shear stress.

2.3.4 Dislocation Stress, Strain, and Energy

At an atomistic level, dislocations are the result of a missing or inserted half plane of atoms or a twist in the perfect crystal that causes a plastic deformation. Dislocations can also be treated as stress/strain fields in a continuum model. This section will examine the different dislocation types, and their stress/strain fields as a continuum. To help envision this theory, the stress and strain will be examined with reference to Volterra tubes as pictured in figure 2.10. Volterra tubes consist of a hollow cylinder that is cut down the side. The area around the cut is then shifted and the sides are joined together again, and the stress/strain in the tube is representative of a dislocation.

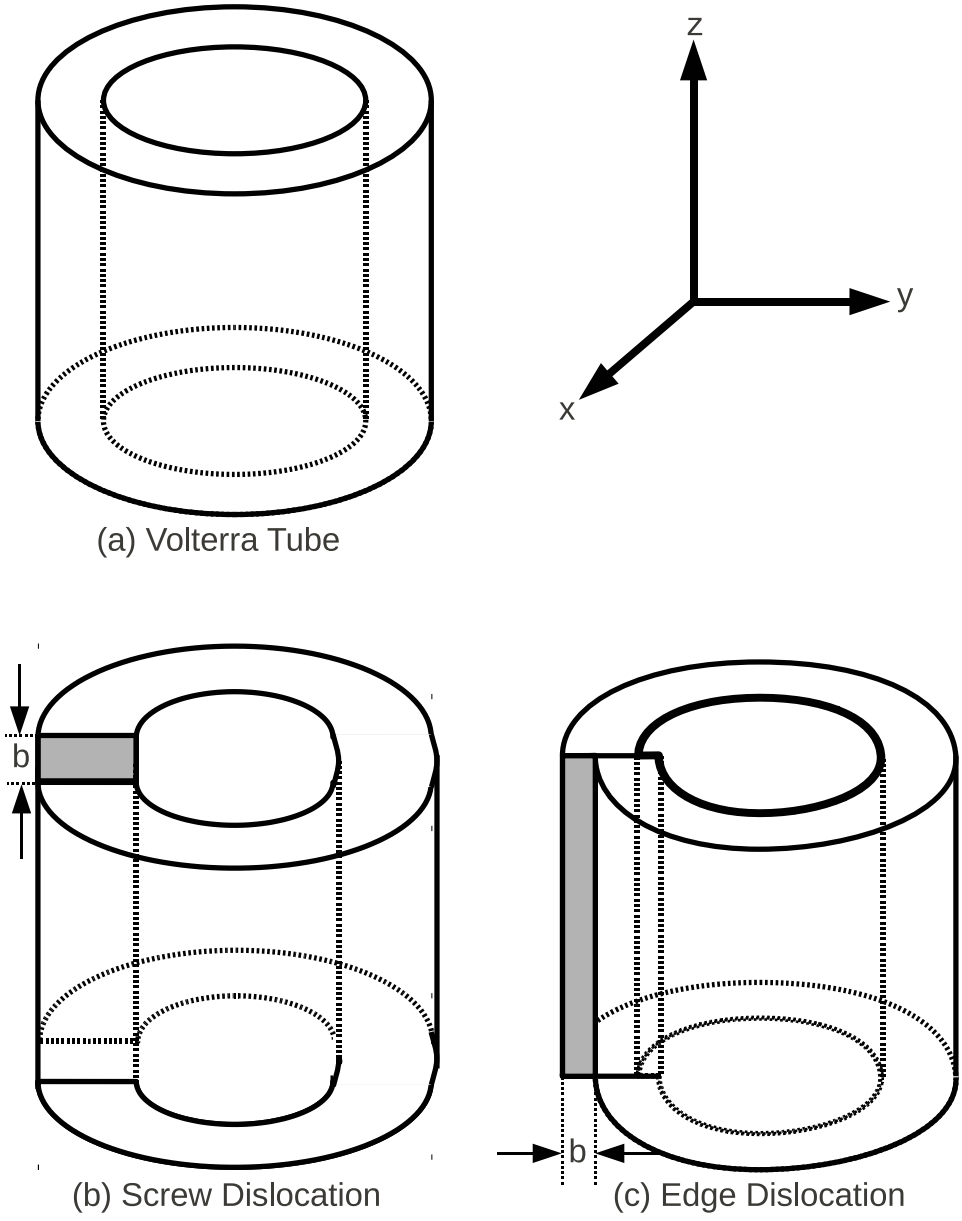

Figure 2.10: Diagrams of a Volterra tubes that represent (b) screw dislocations, and (c) edge dislocations.

Screw Dislocation

The Volterra tube for a screw dislocation is represented in figure 2.10(b). The sides around the cut in the tube are displaced by $\pm b/2\,\hat{z}$ to make a total displacement of $b\hat{z}$. The parallel between the atomistic model (figure 2.7) and the continuum model can be easily seen. It can bee seen that there is no displacement in the x or y direction and, written in polar coordinates, the displacement, u, in the z direction is [7, 8]

$$u_z = \frac{b\theta}{2\pi} = \frac{b}{2\pi}\tan^{-1}\left(\frac{y}{x}\right). \tag{2.2}$$

Using standard elastic theory, the strain can be quickly determined to be

$$\begin{aligned}
&\epsilon_{xx} = \epsilon_{yy} = \epsilon_{zz} = \epsilon_{xy} = \epsilon_{yx} = 0 \\
&\epsilon_{xz} = \epsilon_{zx} = -\frac{b}{4\pi}\frac{y}{(x^2+y^2)} = -\frac{b}{4\pi}\frac{\sin\theta}{r} \\
&\epsilon_{yz} = \epsilon_{zy} = -\frac{b}{4\pi}\frac{x}{(x^2+y^2)} = -\frac{b}{4\pi}\frac{\cos\theta}{r}.
\end{aligned} \tag{2.3}$$

From the strains the stresses can also be determined as

$$\begin{aligned}
&\sigma_{xx} = \sigma_{yy} = \sigma_{zz} = \sigma_{xy} = \sigma_{yx} = 0 \\
&\sigma_{xz} = \sigma_{zx} = -\frac{\mu b}{4\pi}\frac{y}{(x^2+y^2)} = -\frac{\mu b}{4\pi}\frac{\sin\theta}{r} \\
&\sigma_{yz} = \sigma_{zy} = -\frac{\mu b}{4\pi}\frac{x}{(x^2+y^2)} = -\frac{\mu b}{4\pi}\frac{\cos\theta}{r}.
\end{aligned} \tag{2.4}$$

Where μ is the shear modulus.

Edge Dislocation

The stress and strain equations of an edge dislocation are much more complicated than those of a screw dislocation. For this reason the derivation of the displacements is omitted and the resulting strain equations are as follows:

$$\begin{aligned}
\epsilon_{xx} &= \frac{by}{2\pi}\frac{\mu y^2 + (2\lambda+3\mu)x^2}{(\lambda+2\mu)(x^2+y^2)^2}, \\
\epsilon_{yy} &= \frac{by}{2\pi}\frac{(2\lambda+\mu)x^2 - \mu y^2}{(\lambda+2\mu)(x^2+y^2)^2}, \\
\epsilon_{xy} &= \frac{b}{2\pi(1-\nu)}\frac{x(x^2-y^2)}{(x^2+y^2)^2}, \\
\epsilon_{zz} &= \epsilon_{xz} = \epsilon_{yz} = 0.
\end{aligned} \tag{2.5}$$

Where λ is the first Lamé constant and ν is Poisson's ratio. The stresses calculated from these strains are:

$$\begin{aligned}
\sigma_{xx} &= \frac{\mu b}{2\pi(1-\nu)}\frac{y(3x^2+y^2)}{(x^2+y^2)^2}, \\
\sigma_{yy} &= -\frac{\mu b}{2\pi(1-\nu)}\frac{y(x^2-y^2)}{(x^2+y^2)^2}, \\
\sigma_{zz} &= \nu(\sigma_{xx}+\sigma_{yy}) = \frac{\mu\nu by}{\pi(1-\nu)(x^2+y^2)}, \\
\sigma_{xy} &= -\frac{\mu b}{2\pi(1-\nu)}\frac{x(x^2-y^2)}{(x^2+y^2)^2}, \\
\sigma_{xz} &= \sigma_{yz} = 0.
\end{aligned} \tag{2.6}$$

In cylindrical coordinates this reduces to :

$$\sigma_{rr} = \sigma\theta\theta = \frac{\mu b}{2\pi(1-\nu)}\frac{\sin\theta}{r},$$

$$\sigma_{zz} = \frac{\mu\nu b}{\pi(1-\nu)}\frac{\sin\theta}{r}, \tag{2.7}$$

$$\sigma_{r\theta} = \sigma\theta\theta = \frac{\mu b}{2\pi(1-\nu)}\frac{\cos\theta}{r},$$

2.3.5 Self Energy of a Dislocation

The elastic energy stored in a unit volume of strained material is proportional to the product of the stress and strain components within it. So for a particular volume the energy is

$$W = \frac{1}{2}(\sigma_{xx}\epsilon_{xx} + \sigma_{yy}\epsilon_{yy} + \sigma_{zz}\epsilon_{zz} + \sigma_{xy}\epsilon_{xy} + \sigma_{yz}\epsilon_{yz} + \sigma_{zx}\epsilon_{zx}). \tag{2.8}$$

Using the relations between strain and stress for an isotropic medium, the energy can be written in terms of the stresses alone as:

$$\begin{aligned} W =& \frac{1}{2\mu}\left[\frac{\lambda+\mu}{3\lambda+2\mu}(\sigma_{xx}^2+\sigma_{yy}^2+\sigma_{zz}^2) + (\sigma_{xy}^2+\sigma_{yz}^2+\sigma_{zx}^2)\right. \\ & \left. -\frac{\lambda}{3\lambda+2\mu}(\sigma_{xx}\sigma_{yy}+\sigma_{yy}\sigma_{zz}+\sigma_{zz}\sigma_{xx})\right] \end{aligned} \tag{2.9}$$

The only non-zero components of the stress in screw dislocation are σ_{xz} and σ_{yz}. Thus the energy is

$$W = \sigma_{xz}^2 + \sigma_{yz}^2 = \frac{1}{2\mu}\left(\frac{\mu b}{2\pi}\right)^2\frac{1}{x^2+y^2} = \frac{1}{2\mu}\left(\frac{\mu b}{2\pi}\right)^2\frac{1}{r^2}. \tag{2.10}$$

Thus, the energy per unit length can be obtain by integrating over r:

$$\xi = \frac{1}{2\mu}\left(\frac{\mu b}{2\pi}\right)^2 \int_{5b}^{R} \frac{2\pi r\, dr}{r^2} = \frac{\mu b^2}{4\pi} \ln \frac{R}{5b}. \tag{2.11}$$

The upper limit of integration R is a distance such that the stress field goes to zero and is usually taken to be the edge of the crystal that the dislocation resides in. In this case a variation in R does not effect the energy much due to it's position in the logarithmic term. The lower limit of integration is $5b$ because towards the center of the dislocation the integral (thus the energy) goes to infinity, this is due to the elastic continuum model breaking down. So the integral is cut off at $5b$ and the stress with in the core is assumed to be constant at $\mu/30$. Thus the total energy is the result from equation (2.11) plus the core energy,

$$\xi_{tot} = \xi + \frac{\mu}{30}\int_0^{5b} dr \approx \xi + \frac{\mu b^2}{10}. \tag{2.12}$$

To determine the self energy of an edge dislocation the substitute the stresses from equation (2.6) into equation (2.9). This is a rather long and tedious calculation, with a result of:

$$\xi = \frac{\mu b^2}{4\pi(1-\nu)} \ln \frac{R}{5b}. \tag{2.13}$$

Again, the core energy of the dislocation is assumed to be the same as in the case of the screw dislocation, and must be added to obtain the total energy. Comparing the self energy of the screw (equation (2.11)) and edge (equation (2.13)) dislocation, they only differ by a factor of $1/(1-\nu)$ which for HgCdTe is ~ 1.5. In most cases, it can be assumed that the two dislocations have approximately the same energy (i.e. same order of magnitude).

Finally, a mixed dislocation is the combination of an edge and screw dislocation, and it is possible to use the principle of superposition to determine the self energy. In this case θ is used to describe the angle between the Burgers vector and dislocation line. Meaning that

$\theta = 0$ describes an screw dislocation, $\theta = 90\ ^\circ$ an edge dislocation, and any other angle a mixed dislocation. By the principle of superposition, the energy of a mixed dislocation is

$$\xi = \frac{\mu b^2}{4\pi(1-\nu)}(1 - \nu\cos^2\theta)\ln\frac{R}{5b}. \tag{2.14}$$

Line Tension

The energy of a curved dislocation is higher that that of a straight dislocations. Two parallel dislocations with opposite Burgers vectors are attracted to each other, due to their stress fields being equal and opposite. Consider a circular dislocation loop that has a radius $\mathcal{R}$. Opposite edges of the dislocation loop are equivalent to parallel dislocations with opposite burgers vectors. In addition, all other sections of the dislocation loop will have a component of their Burgers vector that is equal and opposite, thus they will also induce an attractive force, promoting a shrinking of the dislocation loop. Thus the loop will act on itself to minimize energy. The force that causes the dislocation loop to shrink is called the *line tension* and is analogous to the surface tension felt by a soap bubble. The line tension produces a force with the effect to make a curved dislocation segment become straight.

Any curved segment (not just dislocation loop) of a dislocation will feel a line tension that will act to make it straight. The force felt by the dislocation is highly dependent on the radius of curvature of the curved segment. A rough approximation of this force is given by[7, 8]

$$\mathbf{F} = \frac{\mu b^2}{\mathcal{R}}, \tag{2.15}$$

where μ is the shear modulus, and b is the Burgers vector. So as the radius of curvature, $\mathcal{R}$, becomes large, the force is negligible, but for areas of small radius of curvature the large force will quickly cause them to straighten.

Image Force

If a dislocation is near a free surface, the stress field of the dislocation will extend outside the crystal. As this can not physically be the case, the solution is to use the method of image forces to ensure that the stress field is zero at the surface. This situation is analogous to the electrostatic image charge, where a charge that is placed near a conducting surface behaves as if there were an equal and opposite charge on the other side of the conductor. If a dislocation is near a free surface, then the total strain field is equivalent to the dislocation plus an equal and opposite image dislocation outside the surface.

As an example, if a screw dislocation lies close and parallel to the free surface of the crystal, the image dislocation would be a screw dislocation with opposite burgers vector outside the free surface. It is clear that the dislocation in the crystal would feel an attractive force towards the surface, ultimately causing the dislocation to leave the crystal.

For another example, invoking the theory of line tension from the previous section, it is easy to understand the concepts of image forces. Consider a semicircular dislocation at the surface of a crystal. The image force of the dislocation will be an equal in opposite half circle that is outside of the crystal. Thus, for all practical purposes the half-loop outside the crystal combined with the half-loop within the crystal can be treated as if they were a full dislocation loop, and would have a tendency to shrink.

2.4 Lattice Mismatch and Misfit Dislocations

Heteroepitaxy frequently implies that the crystal being grown has a different lattice constant than the substrate that it is being grown upon. The difference in lattice constant means that the atomic planes will either not line up perfectly and cause stress/strain at the interface. The lattice mismatch of a thin film can be shown to be

$$f_i = \frac{a_l - a_s}{a_s}, \tag{2.16}$$

where a_l and a_s are the lattice constants of the layer and substrate respectively. For the case of CdTe on Si, with lattice constants of 6.48 and 5.43Å, this is $f_i \approx 19\%$. Due to this being a thin film ($a_s \gg a_l$), for a strained layer the lattice mismatch is equivilent to the strain at the interface. If the lattice mismatch is positive there is a compressive strain, and if it is negative there is a tensile strain. Because the lattice mismatch is equivalent to the strain, the stress (σ_i) can be calculated as

$$\sigma_i = \mu f_i, \tag{2.17}$$

where μ is the shear modulus. As the epilayer grows thicker the stress in the crystal increases. At some *critical thickness* the stress is large enough that it is energetically favorable to form dislocations at the interface to relive the stress rather than continuing to grow a strained layer. This type of dislocations are called *misfit dislocations*. For materials with a small lattice mismatch, the critical thickness can be as large as several microns. On the other hand, for mismatches $> 10\%$ the critical thickness is reduced to less than a monolayer[2]. It is for this reason that the misfit dislocations are unavoidable in CdTe epilayers grown on Si.

In the case of CdTe, all of the strain from the lattice mismatch will result in a network of misfit dislocations at the interface. Ideally, misfit dislocations are supposed to extend across the entirety of the interface and as a result relive the misfit strain. In reality the formation of misfit dislocations is a random process resulting in a high concentration of short misfit dislocations scattered throughout interface. Because a dislocation can only terminate at a free surface (not spontaneously with in the bulk of the crystal), the edges of the misfit dislocations will curve up interference from other dislocations in the lateral directions. The final state of the dislocations will be a half loop extending from the surface to the interface and back to the surface again, this is depicted in figure 2.11. The stress relieving section at the interface is termed the *misfit component* and the sections that extend from the interface to the surface is called the *threading component*.

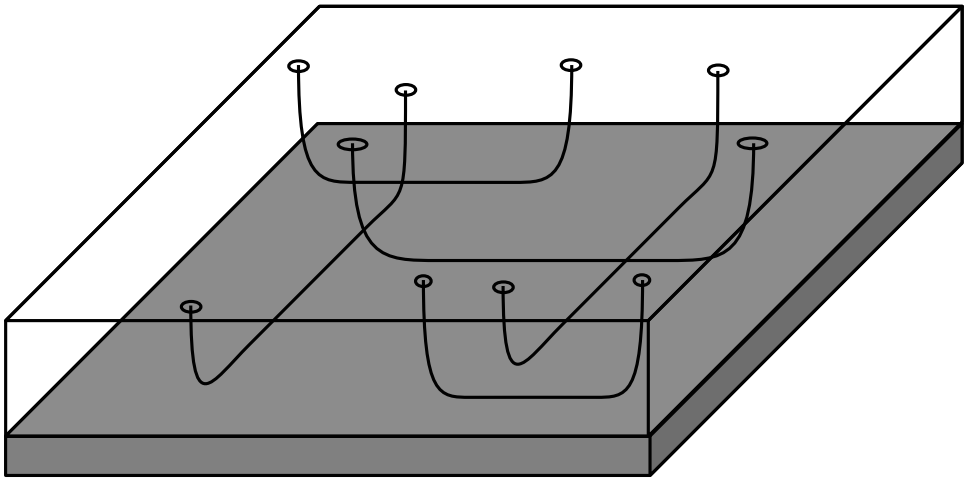

Figure 2.11: Depiction of dislocations formed at an interface resulting in a half-loop. The misfit components lie along the interface and the threading components terminate at the free surface.

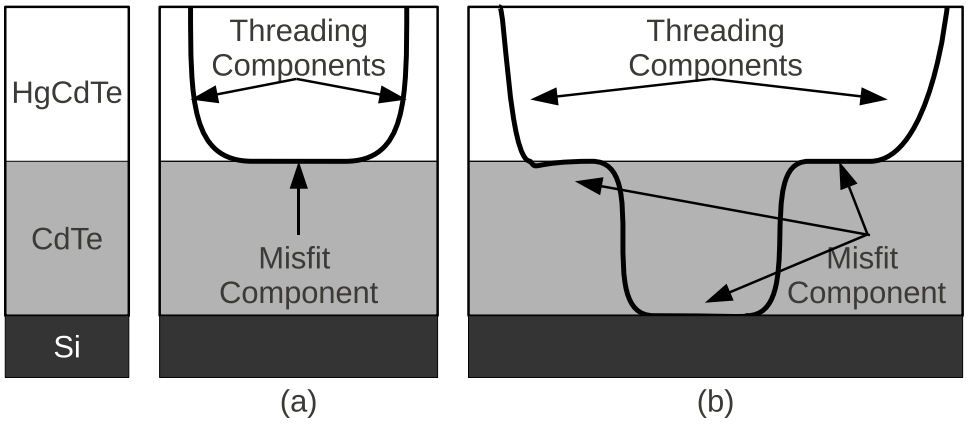

Figure 2.12: Schematic representations of (a) threading dislocations arising from a spontaneously generated misfit segment; and (b) a threading dislocation generated from misfit dislocation that is seeded by an existing dislocation from the buffer layer.

The lattice mismatch between CdTe and LWIR HgCdTe is $f_i \approx -0.04\%$ (a tensile stress). This also leads to a strain at the interface that is accommodated via misfit dislocations. In the case of HgCdTe/CdTe, misfit dislocation can occur in two basic geometries. Figure 2.12 (a) shows a spontaneously generated dislocation due to interface strain. The two ends of the misfit dislocation threads to the surface of the crystal. Figure 2.12 (b) shows the situation where threading dislocations from the CdTe layer extend along the HgCdTe/CdTe interface and produces a misfit. The misfit dislocation then threads up to the HgCdTe surface. In the scope of this work there is no effective difference between the two geometries of misfit dislocations depicted in figures 2.12 (a) and (b). Their behavior is the same in terms of dislocation motion and measurement of the dislocation density.

2.4.1 Dislocation Interaction

When a layer is subjected to mechanical or thermal stress, it is possible for the dislocations in the layer to become mobile. When dislocations move there is a statistical probability that they will move to within close proximity of each other. As a result the strain fields around the dislocations will overlap. If the overlapping of the fields leads to a higher energy state, then the dislocations will have a repelling force, if it leads to a lower energy state then the dislocations will have an attractive force.

The force on a dislocation by an external strain field can be calculated by using the Peach-Koehler formula[7, 8]

$$\vec{F} = \begin{vmatrix} \hat{i} & \hat{j} & \hat{k} \\ t_x & t_y & t_z \\ G_x & G_y & G_z \end{vmatrix} = \vec{t} \times \vec{G}, \tag{2.18}$$

where the t_i's are the line vectors of the dislocation. The G_i's are defined as

$$G_x = \sigma_{xx}b_x + \sigma_{xy}b_y + \sigma_{xz}b_z,$$

$$G_y = \sigma_{yx}b_x + \sigma_{yy}b_y + \sigma_{yz}b_z, \tag{2.19}$$

$$G_z = \sigma_{zx}b_x + \sigma_{zy}b_y + \sigma_{zz}b_z,$$

where the b_i's are the components of the Burgers vector of the dislocation and σ_{ij}'s are the components of the stress acting on the dislocation. In the case of two dislocations interacting with each other, the stresses in equation (2.19) are the stresses from the second dislocation that were given in section 2.3.4 and 2.3.4.

Rather than tediously calculating the force between two dislocations it is sufficient to generalize that dislocations that are in close proximity to each other will feel a force that is either attractive, repulsive or negligible. For the case of an attractive force the dislocations will interact and they either annihilate each other or coalesce. At a certain distance, the force between two dislocations is great enough that an interaction is guaranteed and this distance is called the *annihilation radius*.

The type of dislocation interaction, annihilation or coalescence, is determined by summing their Burgers vectors. These two types of reactions are depicted in figure 2.13. The sum of the Burgers vectors of any dislocation going into the dislocation knot must be equal to the sum of the Burgers vectors of dislocations leaving the knot, this is known as the conservation of Burgers vectors.

An example of Burgers vectors that result in dislocation annihilation is:

$$\frac{a}{2}[1\bar{1}0] + \frac{a}{2}[\bar{1}10] \rightarrow 0. \tag{2.20}$$

In this case two dislocations with opposite Burgers vectors combine to annihilate each other. This reaction is termed annihilation in thin films, because the result is that both dislocations

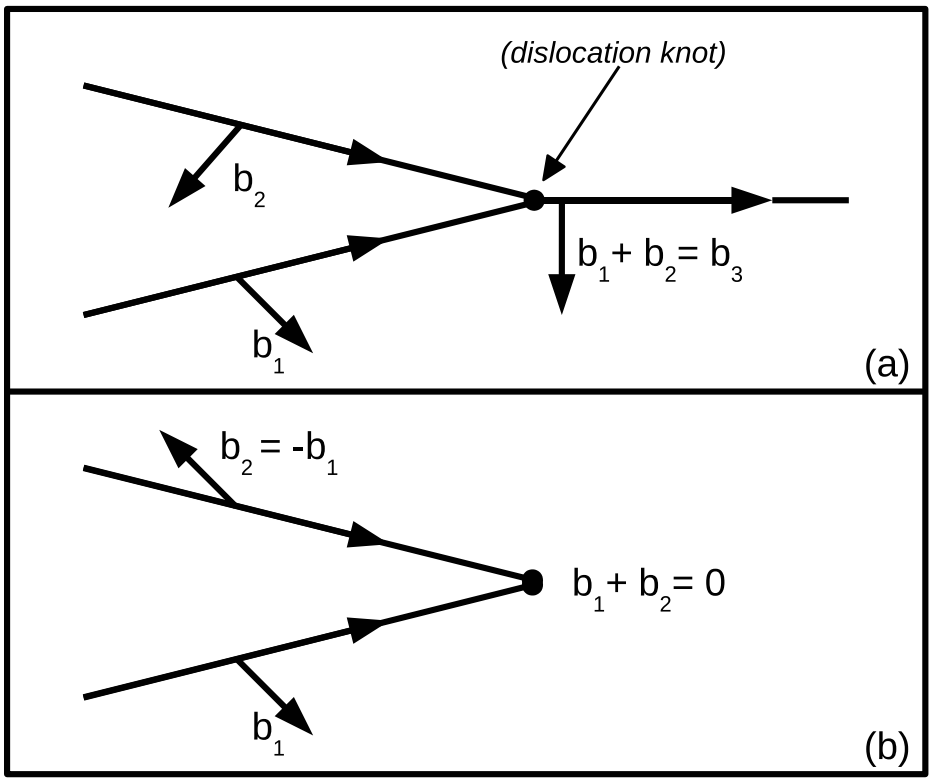

Figure 2.13: Graphic depiction of (a) dislocation coalescence, and (b) dislocation annihilation.

no longer intersect the surface, in essence annihilating the threading dislocations. It should be noted that there is an apparent paradox with dislocation annihilation. The result of this sort of interaction is that two dislocations join together to form a single dislocation. The result is that apparently the burgers vector switches sign at the knot (see figure 2.13 (b)), but really the line and Burgers vector need to be altered to show a continuous dislocation rather than two dislocations approaching the same point.

Coalescence occurs when the sum of the two Burgers vectors is non zero, and the result is that two dislocations transform into a single dislocation, this is pictured in figure 2.13 (a). The self energy of a dislocation is roughly proportional to the square of the Burgers vector. Thus it makes sense that coalescence will only occur when the resulting dislocation has a self energy that is lower that the two separate dislocations. Thus the condition

$$\vec{b_1}^2 + \vec{b_2}^2 \geq (\vec{b_1} + \vec{b_2})^2 \tag{2.21}$$

must be satisfied.

When two 60 ° dislocations coalesce the result can some times result in a dislocation where the burgers vector is perpendicular to the slip plane, noting that the slip planes in a zincblende crystal are the {110} planes. Thus the dislocation is an immobile dislocation, also called a *sessile dislocation*. Examples of such sessile dislocation coalescence are the Lomer lock

$$\frac{a}{2}[01\bar{1}] + \frac{a}{2}[101] \rightarrow \frac{a}{2}[110], \tag{2.22}$$

or a Lomer-Cottrell lock

$$\frac{a}{6}[\bar{1}2\bar{1}] + \frac{a}{6}[2\bar{1}1] \rightarrow \frac{a}{6}[110]. \tag{2.23}$$

2.5 The Half-Loop Relaxation Model

Having the described the methods of dislocation motion and interaction, it is now possible to develop the theory of how dislocation density reduction is possible. As it relates to

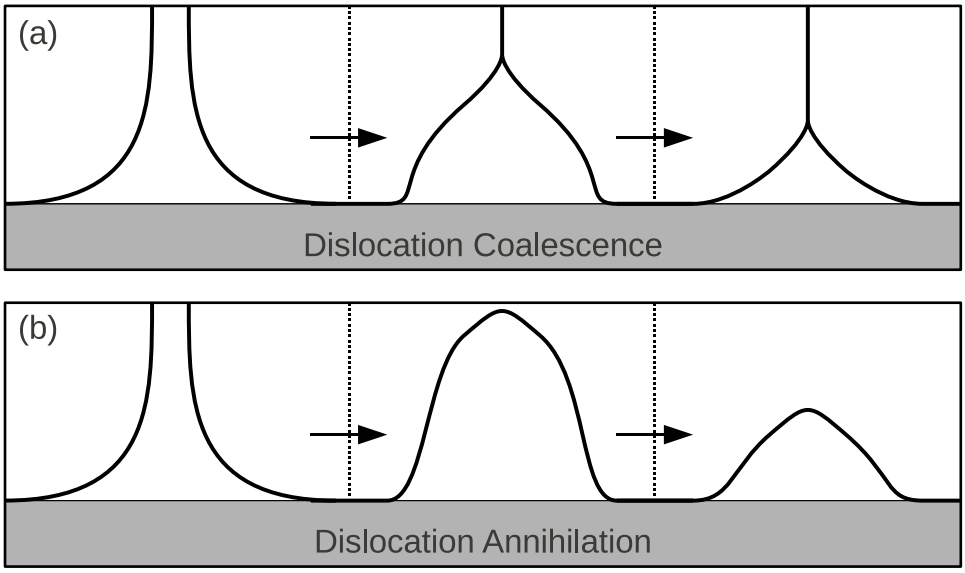

Figure 2.14: Schematic representations of (a) dislocation coalescence resulting in two dislocations combining to form a single dislocation of a different type; and (b) dislocation annihilation and loop relaxation.

this work, thermal stress is provided by the annealing process and allows for the threading dislocations to move via glide and/or climb. Dislocation density reduction results from annihilation and/or coalescence. Once activated, the dislocations move around and, at some point, approach close enough to each other for interaction to occur. The two adjacent threading dislocations, depending on their Burgers vectors, will then proceed to coalesce, annihilate, or disregard one another. In the latter case, the dislocations will continue moving until they approach other dislocation and a separate interaction occurs. Coalescence results in the two threading dislocations combining to create a single threading dislocation of a different type, as pictured in Figure 2.14 (a). Because the new dislocation segment is more energetically favorable than the two original segments, the coalescence will proceed like a zipper in an attempt to further minimize the energy. In the case of annihilation the dislocations combine into a single dislocation that no longer intersects the free surface, as pictured in Figure 2.14 (b). This forms a subsurface half-loop between the two misfit components.

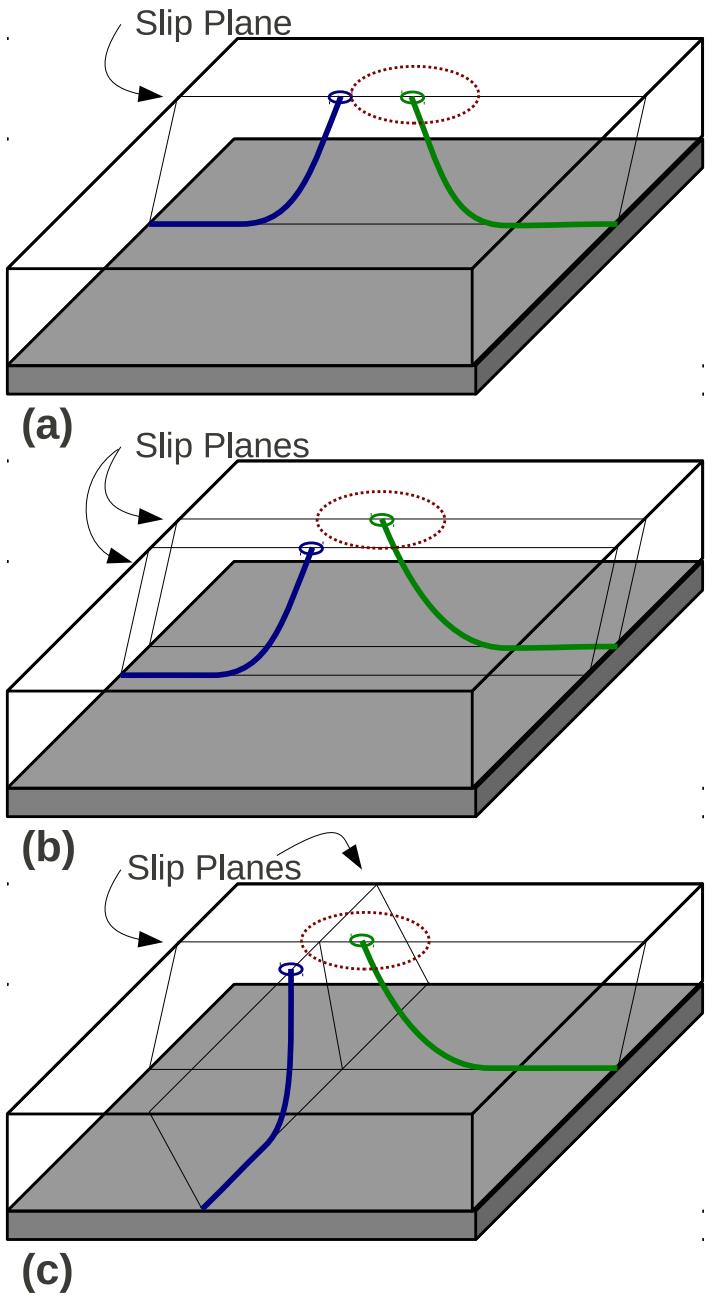

Figure 2.15: Schematic representations of the three basic geometries for threading dislocation interaction: (a) dislocation interaction occurring when two dislocations on the same slip plane move and intersect; (b) dislocations on parallel slip planes that move to within close proximity and interact via cross slip and/or climb type motion; and (c) two dislocations on intersecting slip planes that move and interact at the intersection.

The interaction between 2 dislocations can occur in 3 basic geometries as pictured in figure 2.15[9]. The simplest form is two dislocations that are on the same slip plane that move towards each other, this is shown in figure 2.15 (a). If two dislocations lie on parallel slip planes that are separated by a small distance, when the dislocations move into close proximity they will feel force from one another as pictured in figure 2.15 (b). If this is attractive they can move via either climb or cross slip and interact with each other. The maximum separation of the two slip planes where interaction can still occur is believed to be directly related to the amount of climb type motion that the dislocations are capable of. The third geometry is when the dislocations are on different non-parallel slip planes. During dislocation motion, it is possible for the dislocations to meet at the intersection of the two planes as pictured in figure 2.15 (c). The result of this sort of interaction can be a Cottrell-Lomer lock (see page 2.4.1).

The subsurface half-loop formed via annihilation is then subjected to a line tension (see section 2.3.5). The dislocation is pinned to the interface due to the misfit component, so the tension force acts to relax the half-loop away from the free surface and towards the interface in order to become as straight as possible, this process is depicted in figure 2.14 (b). The only other force that might counteract the line tension would be interaction with other dislocations. These could be in the form of threading or misfit dislocations or other subsurface half-loops that are already partially relaxed. If another dislocation with a Burgers vector that causes a repulsive force lies in the path of the relaxation, then the dislocation will be inhibited from further relaxation. As more and more half-loops relax in the same area, this will read to a pile up near the interface. The resulting pile up of these subsurface interactions are shown in figure 2.16.

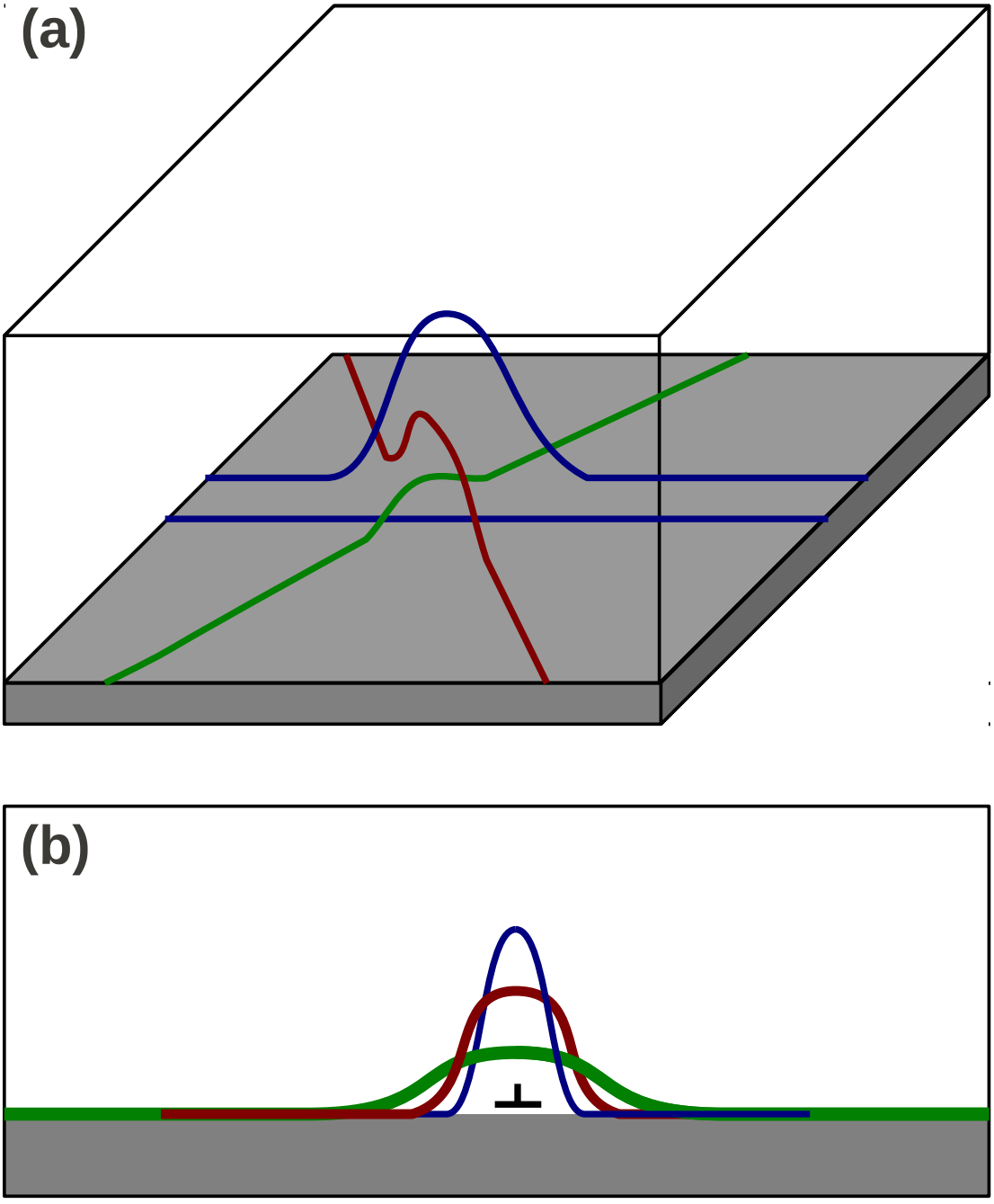

Figure 2.16: Schematic representations of relaxing subsurface dislocation half-loops interacting and resulting in a pile up near the interface.

2.6 Observation of Dislocations

In order to determine the dislocation density in a layer it is necessary to develop one or more methods of observing dislocations and counting them. Quite simply, dislocations are regions of strain that exist in the layer. This aspect allows for several methods of observation. The two main methods of observation are etch pit density and x-ray diffraction (XRD). The latter method has been developed to a great extent in several different material systems[10], but is relatively immature for CdTe and HgCdTe. The exact reasons for the immaturity are unknown, but it should be considered that the other material systems are generally grown with a low index orientation. This allows for many symmetric planes to be examined with XRD. In the case of CdTe and HgCdTe, the preferred orientation is in the [211] direction, and thus the majority of secondary planes that can be measured are highly asymmetric. Thus XRD is generally used as a non-destructive qualitative means of characterization. There has been some work on using XRD for quantitative measurements of dislocation density in CdTe[11], but it is beyond the scope of this work to explore this much further.

The first and foremost method for observing dislocations and measuring their density is the etch pit density (EPD). This method uses a *dislocation decoration etch* to reveal where dislocations intersect the surface, this is commonly referred to as an EPD etch. These etches are highly dependent on the material and crystal orientation for them to function. In the case of HgCdTe and CdTe, the result of an EPD etch is that small pits are formed around the dislocation line due to a difference in etch rate compared to the perfect crystal. The etch rate near the dislocation is faster due to the strain field surrounding the dislocation. The etch pits can be clearly seen under Nomarski optical microscopy and bright field microscopy as shown in figures 2.17 (a) and (b).

After a sample is etched with an EPD solution, the density is measured either by counting the number of pits within an area by hand, or using a computer program to count and calculate the density. In either case it is necessary for the pits to be of sufficient size to be easily visible, but not so large that they overlap. The size of the pits can be controlled by

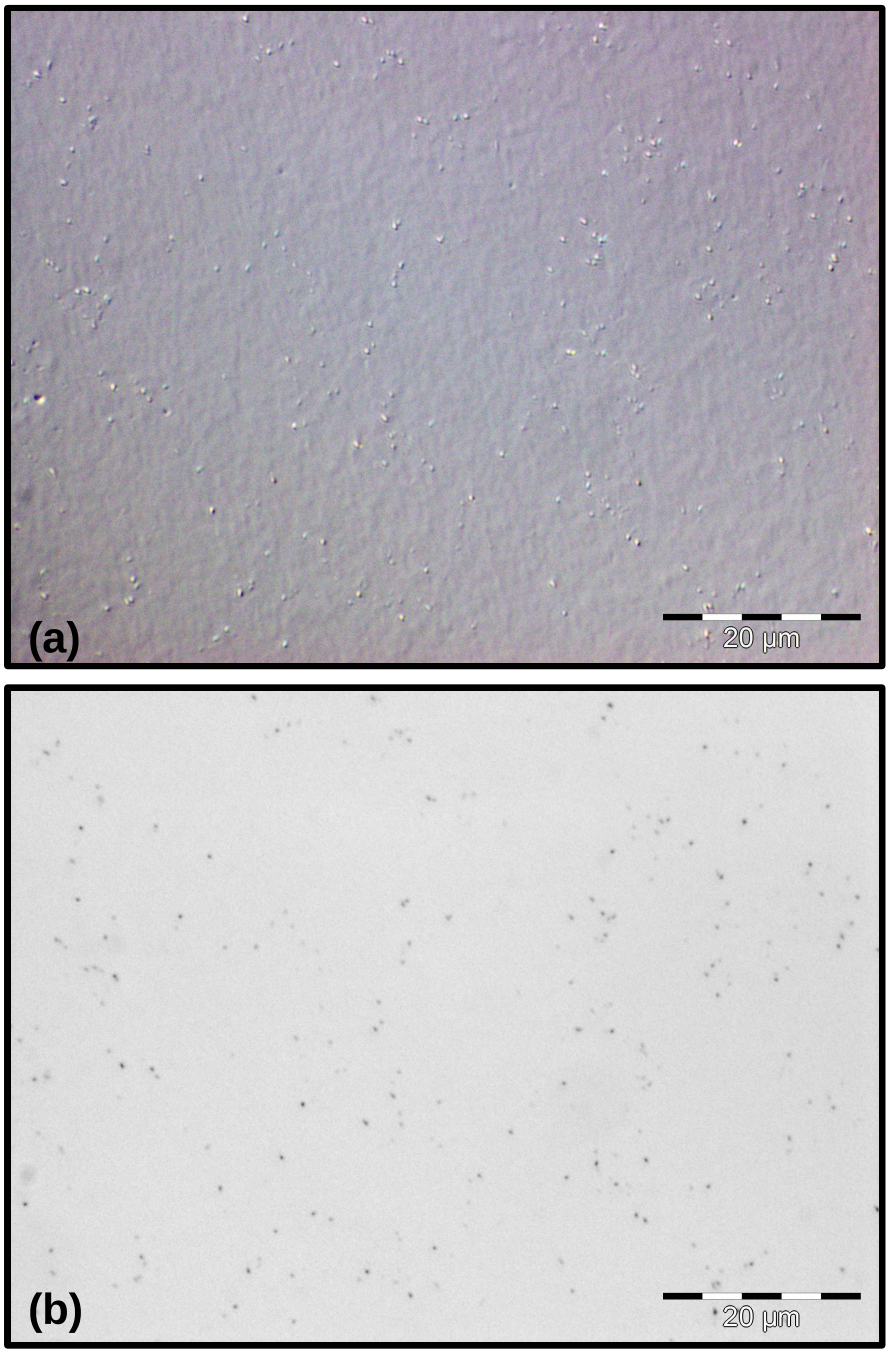

Figure 2.17: Pictures of a EPD etched HgCdTe sample using (a) Nomarski microscopy and (b) bright field microscopy. Sample was etched with the Benson etch and has a measured EPD of 3.3×10^6 cm^{-2}.

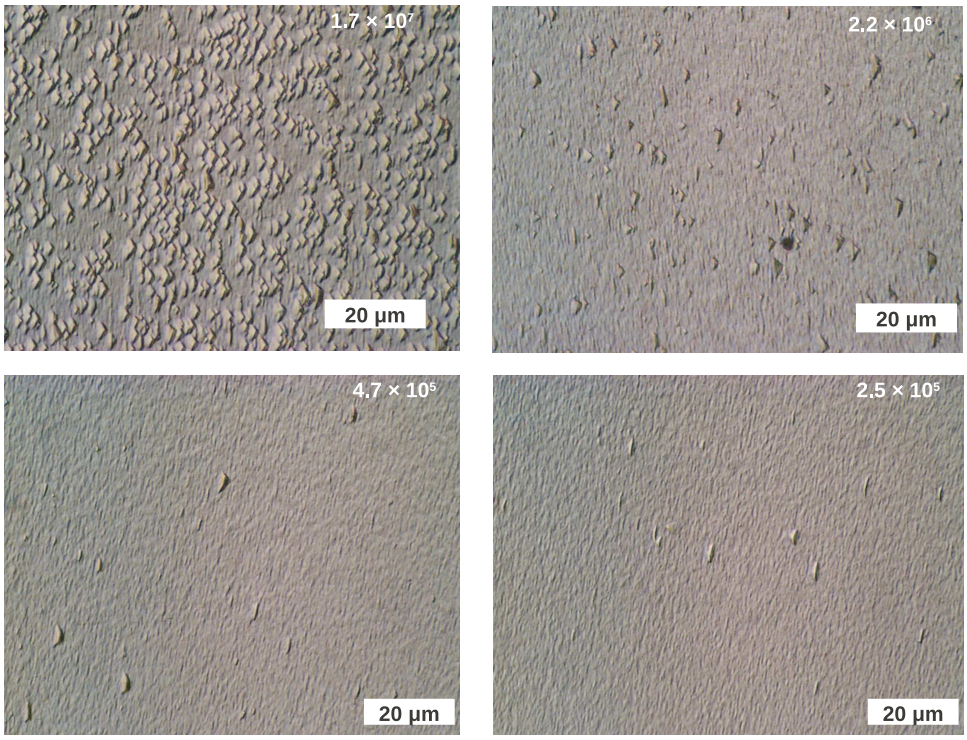

Figure 2.18: Pictures of 4 CdTe samples with different EPDs etched using the Everson etch.

varying the etch time. In this work, the etch times used were designed to form etch pits with a semi-major-diameter of $0.5 - 1$ μm.

2.6.1 Everson Etch

- Lactic acid:HNO_3:HF (25:4:1)

The Everson etch was developed by W. J. Everson[12], and is the standard EPD etch for CdTe layers. Typical Nomarski micrographs of the surface after a 40 s etch are shown in figure 2.18. It is clear that the etch pits take the form of isosceles triangles of various dimensions. Some triangles can be so thin that they appear as if they are just lines. Both broad and thin pits are large and easily visible under a microscope. One draw back of the Everson etch is that it has the tendency to leave the background surface roughened by nanoridges. These nanoridges have the effect of making it difficult to observe some of the

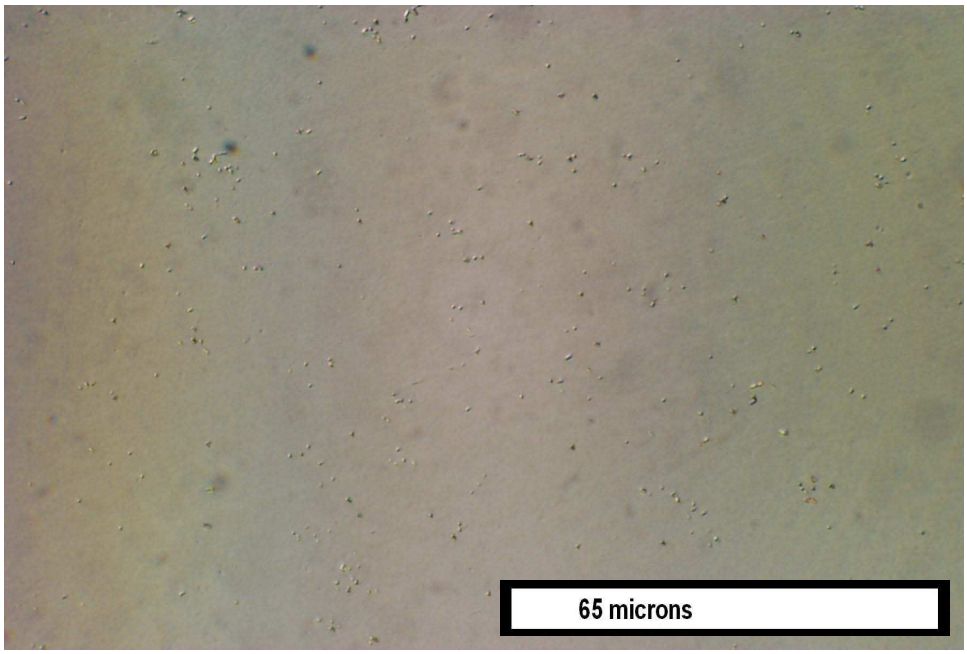

Figure 2.19: Picture of a typical HgCdTe surface after a 35 s Schaake etch as viewed by Nomarski microscopy.

etch pits on the sample. Studies done using atomic force microscopy (AFM) have shown that very small etch pits can be found hidden in the rough background[11, 13, 14]. For samples with extensive nanoridging, it is often practical to perform a quick $(2-3$ s) 0.5% bromine-methanol etch after the EPD etch to help smooth out background roughness in order to make counting easier.

2.6.2 Schaake Etch

- H_2O:HCl:CrO_3 (150ml:25ml:30g)

The Schaake Etch was developed by H. F. Schaake in the 1970's[1], and is the most commonly used EPD etch for HgCdTe samples. Under Nomarski microscopy the pits appear to be round or elliptically shaped and are clearly discernible from other defect structures that might be present on the surface. A typical Nomarski image from a 35 s etch is shown

[1] Though the Schaake EPD etch formula was not officially published, it has been spread via word-of-mouth through out the decades.

in figure 2.19. The Schaake etch gained popularity because it was shown to be a better dislocation etch than the Chen etch as it is capable of revealing pits that the Chen etch will not reveal[15]. It should be noted that EPD values from the Chen etch are up to a half an order of magnitude less than the Schaake etch, this can lead to a problem when comparing the EPD values reported in literature for different different etches.

2.6.3 Benson Etch

- H_2O:HCl:HF:HNO_3:CrO_3 (300 mL:10 mL:10 mL:10 mL:8 g)

The Benson etch was developed in early 2008 by J. D. Benson[13] in an effort to create a CdTe EPD etch that did not leave a rough surface and be a single EPD etch for CdTe and HgCdTe. Figure 2.17 and figure 2.20 show micrograph's of the effects of the Benson etch on HgCdTe and CdTe, respectively. The standard etching time for HgCdTe is 50 s, and the results are very similar to those of the Schaake etch as viewed by Nomarski microscopy. The resulting EPD from the Benson etch is also practically identical to that of the Schaake etch.

The Benson EPD etch, when used on CdTe, is highly aggressive and requires only ~ 10 s to produce proper sized pits. The rough background that results from the Everson etch is greatly suppressed by using the Benson etch. Although the etch pits are slightly blunted and less defined, they are still highly visible and easily counted. EPD data from CdTe layers normally results in higher densities when using the Benson etch rather than the Everson etch.

2.6.4 Etch Pit Characterization

By viewing samples that have been subjected to an EPD etch with a scanning electron microscope (SEM) it is possible to see features than are not visible with an optical microscope. In figures 2.17 and 2.19 the etch pits in HgCdTe sample appear to have an amorphous shape, though when viewed at higher resolution via SEM the etch pits have a clear and defined

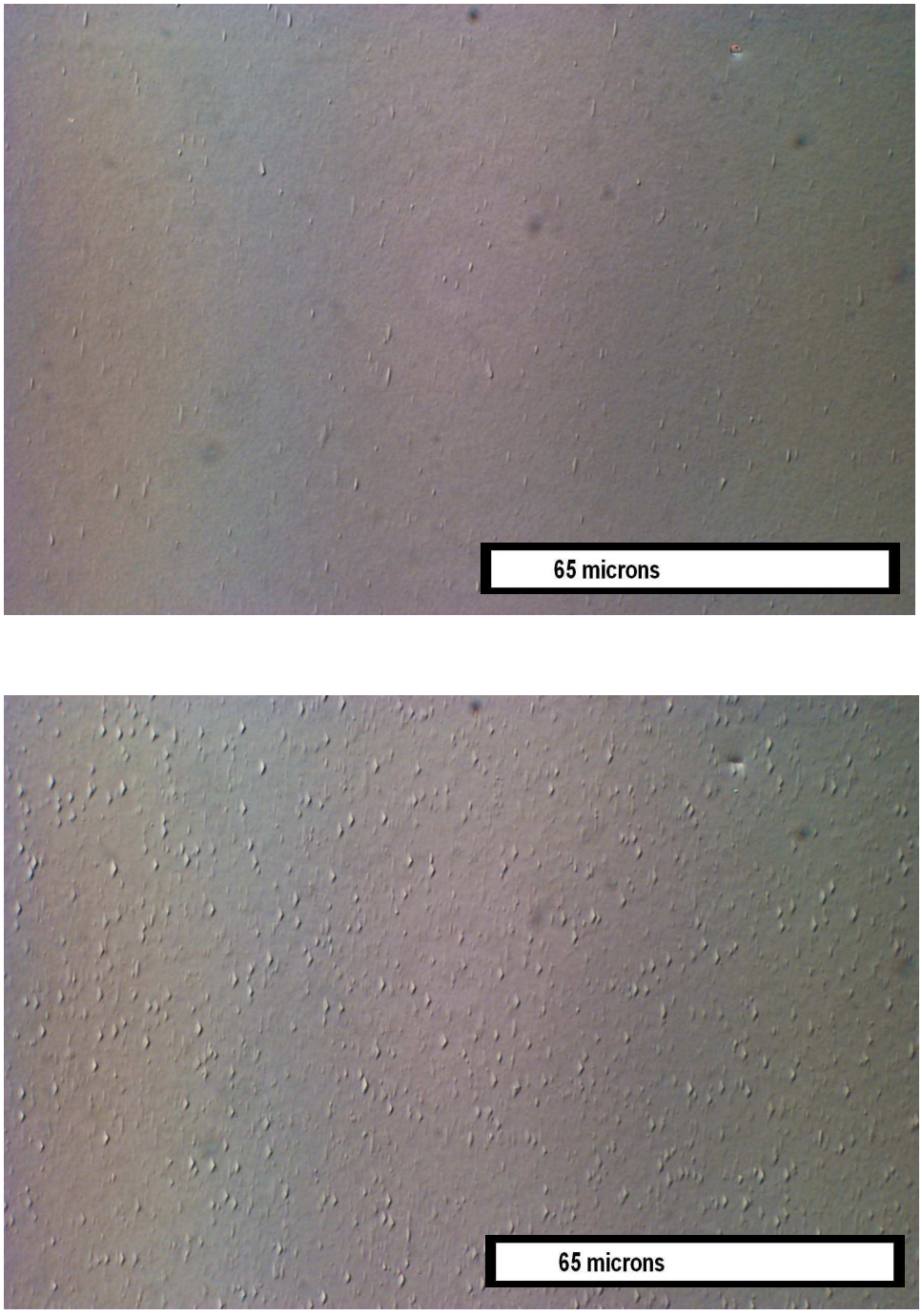

Figure 2.20: Pictures of a typical surface of a CdTe sample after a 10 s Benson etch as viewed by Nomarski microscopy.

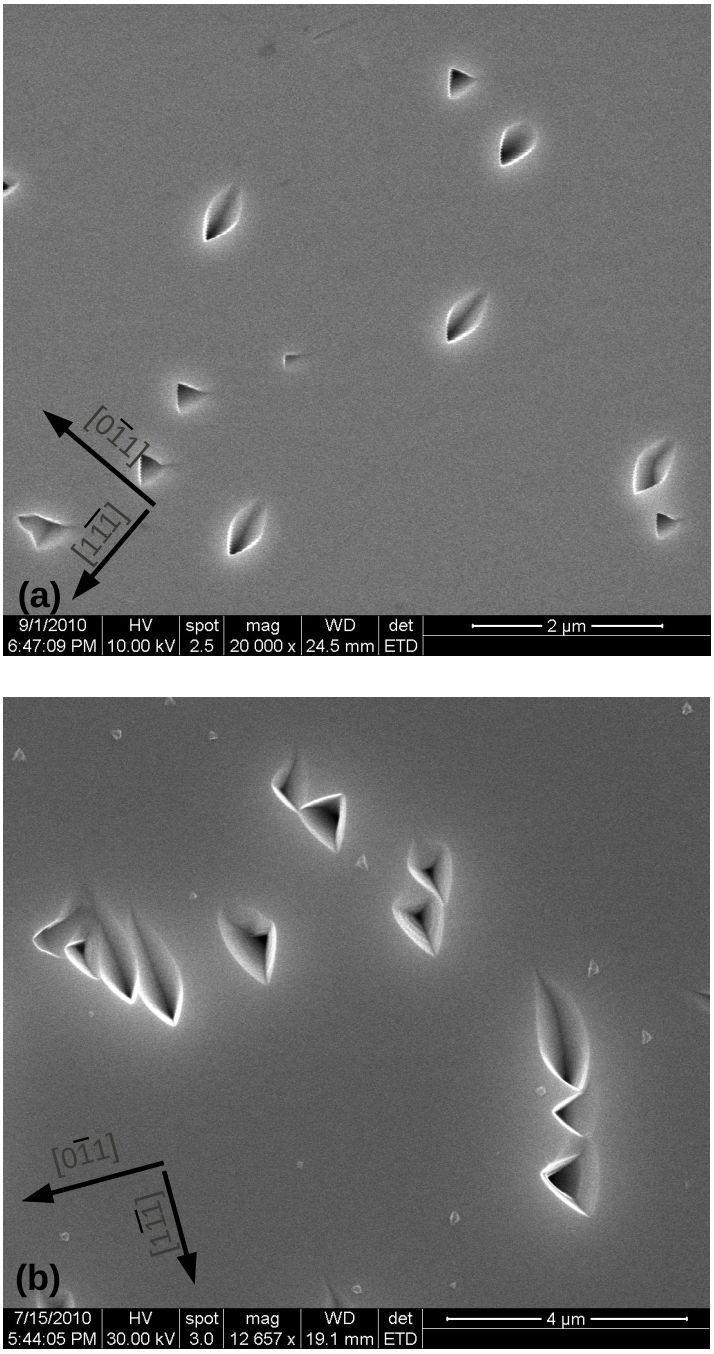

Figure 2.21: SEM images of HgCdTe samples with (a) etch pits from the Benson etch and (b) etch pits from the Schaake etch. Orientation was determined using x-ray diffraction.

range of shapes. Figure 2.21 shows SEM images from both the Benson and Schaake etch. In general the Schaake and Benson etches reveal pits with the same general shapes although it can be seen that the pits generated by the Schaake etch are more faceted and have sharper corners and edges.

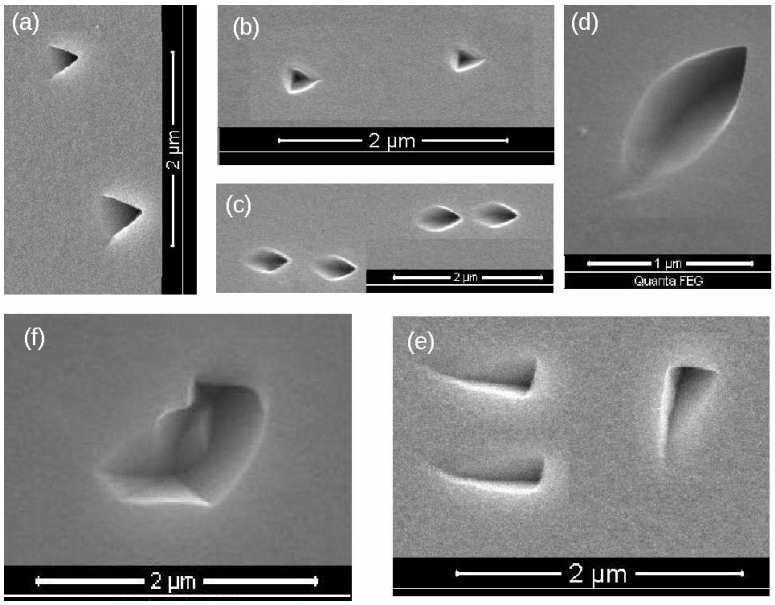

Figure 2.22: Several examples of the different shapes of etch pits that are visible via SEM. (a) and (b) Some examples of the triangular shaped, (c) and (d) fish shaped, (e) wedge shaped, and (f) other.

An examination of the etch pits by SEM in HgCdTe shows that several distinct shapes of pits are visible. The basic shapes, pictured in figure 2.22, are triangular, wedge shaped, fish shaped and other. Triangular shaped pits are pits that have a shape that is close to equilateral, while wedge shapes are any pits that are long and thin (though they can be triangular), both of these shapes can appear in many orientations. While the triangular and wedge shaped pits can be easily broken up in to several more categories, they have not yet been associated with a family of dislocations, so further classification has not been performed. A small number of pits are oddly shaped, and are likely due to several dislocation being in very close proximity but not distinctly any of the above shapes. .

The most distinctly shaped pits that are visible are the fish shaped pit. The longer

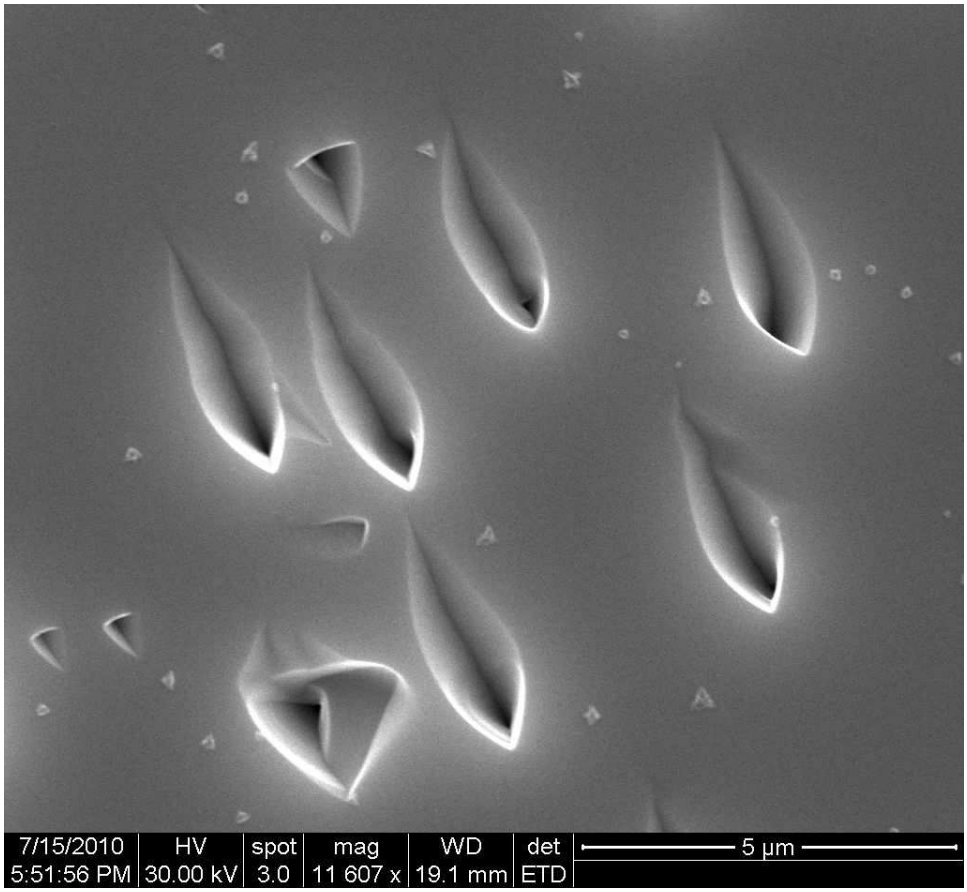

Figure 2.23: SEM image of an HgCdTe sample etched with the Schaake etch. The image depicts a grouping of "fish shaped" dislocations.

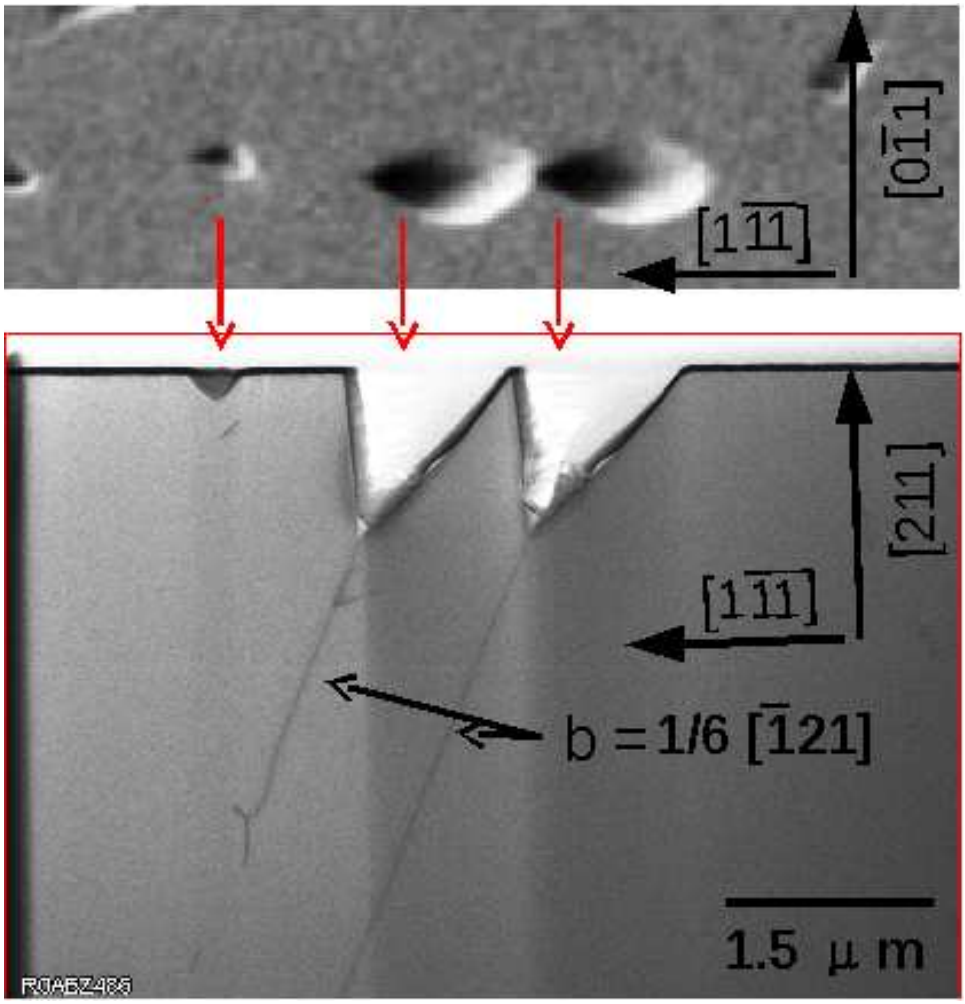

Figure 2.24: SEM and TEM images showing the dislocation associated with the "fish shaped" etch pits. The long dislocation segments correlated with "fish shaped" etch pits determined to be of type: $b = a/6\langle 112 \rangle$. These are Shockley partial type dislocations, which are mobile on their slip planes.

pits that point in the $[1\bar{1}\bar{1}]$ direction are referred to as "fish shaped" due to their unique appearance and tendency to cluster into groups all facing (swimming) in the same direction (see figure 2.23), The different shapes of the etch pits are believed to be directly associated with the line vector of the dislocation which is their source[15–17].

TEM analysis was performed by R. N. Jacobs et al at Night Vision Laboratory in an effort to understand the dislocation line vectors and Burgers vectors that are present in

HgCdTe. Figure 2.24 shows a cross sectional TEM near a fish shape dislocation. The fish shaped dislocations are the result of partial dislocations with a Burgers vector $b = 1/6[\bar{1}21]$ and a line vector $t \approx [511]$. Typing of dislocations in HgCdTe and the shape of their corresponding etch pits is an on going research topic at this time.

Chapter 3: Furnace Setup and Calibration

The overall goal of this work was to use annealing to apply a thermal stress to HgCdTe samples in hopes that the stress will be transferred to the dislocations. If enough force is applied to a dislocation, then it will move and hopefully be removed from the crystal through one means or another. One primary concern with HgCdTe is that when heated, mercury will out gas from the system leaving behind vacancies that affect electrical performance and/or seriously degrade the surface. At high temperatures the loss of an excessive amount of Hg from the crystal can severely damage the layer.

3.1 Annealing Setup

Due to the problem of mercury out diffusion, it is necessary to provide a high Hg over-pressure to preserve the surface morphology of the HgCdTe sample while performing high temperature annealing. Too low of a pressure causes surface to degrade due to excessive outdiffusion of Hg from within the crystal. When the saturated Hg over-pressure is maintained, the sample can withstand temperatures as high as $\sim$ 650 °C without noticeable surface damage. At high temperatures, the required saturated Hg over-pressure is quite large, approaching over 8 atm for a standard *ex situ* cycle annealing. The saturation pressure for any temperature is represented by the upper bound of the curve pictured in figure 2.5. For the annealing of this work, a closed tube system with a Hg over pressure was used. For this, samples were sealed in a quartz ampoule and placed in a furnace for the annealing process.

Schematics of the furnace and an ampoule with relevant dimensions that were used in this work are shown in figure 3.1. In the following sections, a detailed overview of the

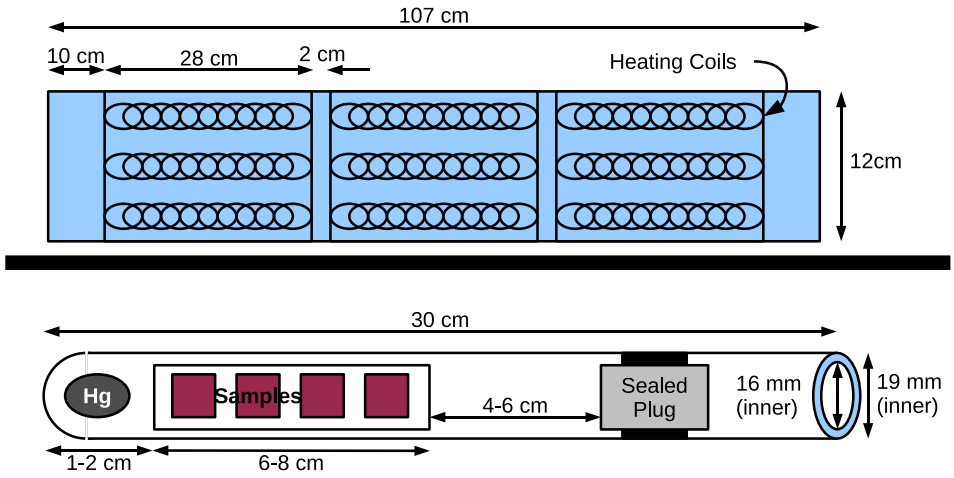

Figure 3.1: Schematic of furnace used for annealing of samples in the ampoule.

annealing setup and important factors and considerations that are needed to optimize the process are given.

3.1.1 Ampoule Sealing and Setup

Quartz ampoules were obtained from Quartz Plus Inc. The ampoules were 30 cm long and had an inner and outer diameter of 16 and 19 mm, respectively.

To ensure that no impurities were transferred to the samples during the annealing process, several cleaning techniques were used on the quartz hardware. Ampoules, inserts, and plugs were cleaned with hydrofluoric acid to etch off their outer layers and remove any contamination that might exist. After cleaning, the ampoules were rinse thoroughly with deionized water and wrapped in aluminum foil and baked at 500 °C in the oven overnight in order to out gas any impurities prior to the annealing process. These ampoules were then stored in the aluminum foil to prevent post processing contamination. The high temperature baking of the ampoules in aluminum foil did raise some concerns that the ampoules might be contaminated by trace amounts of aluminum. SIMS data taken from annealed samples have shown that there is no Al detectable in the layers, as was an initial concern given the use of aluminum foil.

Prior to sealing the ampoule, a small, specific amount of Hg was pipetted into the ampoule to provide the Hg overpressure during the anneal. The amount of Hg used varied based on the annealing temperature. The as grown samples (i.e. without any cleaning) were then placed into the quartz insert, which later is pushed to the end of the ampoule, but providing enough room for the Hg droplet to remain behind the samples. The plug is then inserted to a distance of no less than 4 cm from the closest sample.

The ampoules were then attached to the vacuum stage where mechanical and sorption pumps were used to reduce the pressure to $\sim 1 \times 10^{-5}$ torr. The quartz ampoule was melted onto the plug to create the seal using a medium flame from the O-H torch. It was found that during the sealing process, the ampoule remained cool up to a distance of about 3-4 cm from the plug. After sealing, a wet cloth was placed around the area of the ampoule where the samples reside to ensure that they did not heat up excessively due to any residual heat from the sealing process. Once the ampoule was cool enough to be safely handled, it was loaded into the furnace for annealing. Note, during the sealing process, the pressure would increase a moderate amount to $2 - 3 \times 10^{-5}$ torr.

After removing the samples, any Hg droplets, glass shards, and/or other debris were cleaned from the sample surface by means of an acetone spray gun and isopropyl rinse. In general it is rather rare to see significant damage to the sample due glass shards.

3.1.2 Furnace Calibration

External annealing experiments were performed in a Lindenburg 4.5 inch 3 zone furnace. The three zones have a type-K thermocouple located 1.5 inches from the top of the furnace, and each zone is controlled by it's own proportional-integral-derivative controller (PID). For the first half of experimentation Eurotherm controllers were used. The temperature was manually set for each step of the annealing process. For this reason, the ramp rate was not controllable during early experimentation. For the latter part of experimentation, the controllers were replaced with for Omega Cn8200 series Temperature and Process Controllers that had the capability of being computer controlled. Omega Solid State Relays (SSR's)

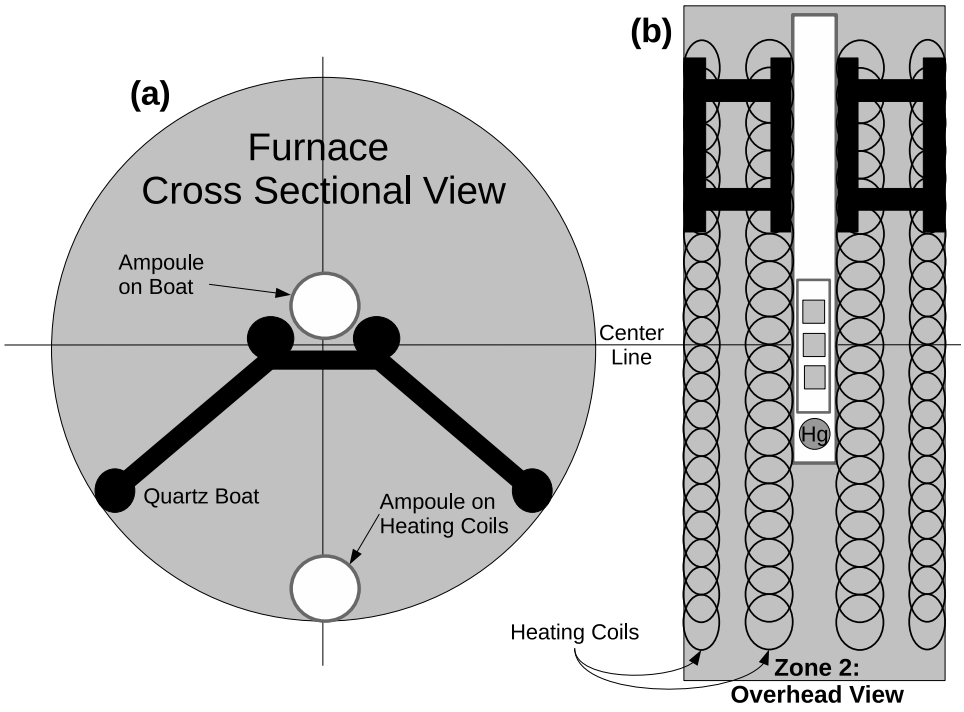

Figure 3.2: Cross sectional schematics of the furnace used for annealing.

were used for digital control of the current to the heating coils.

The furnace has several temperature profiles that are of importance to the reproducibility of annealing temperature. The radial profile causes temperatures to be higher when an ampule is placed in close proximity to the heating coils at the bottom of the furnace rather than floating at the center of the furnace, these two configurations are depicted in figure 3.2 (a). The horizontal profile causes the temperature to decrease slightly as ampoule is moved away from the middle of the furnace and towards areas between the zones. A picture of the ampoule with the samples in the middle of furnace is shown in figure 3.2 (b). This combined with thermocouple drift required extensive calibration in order to properly estimate actual annealing temperatures.

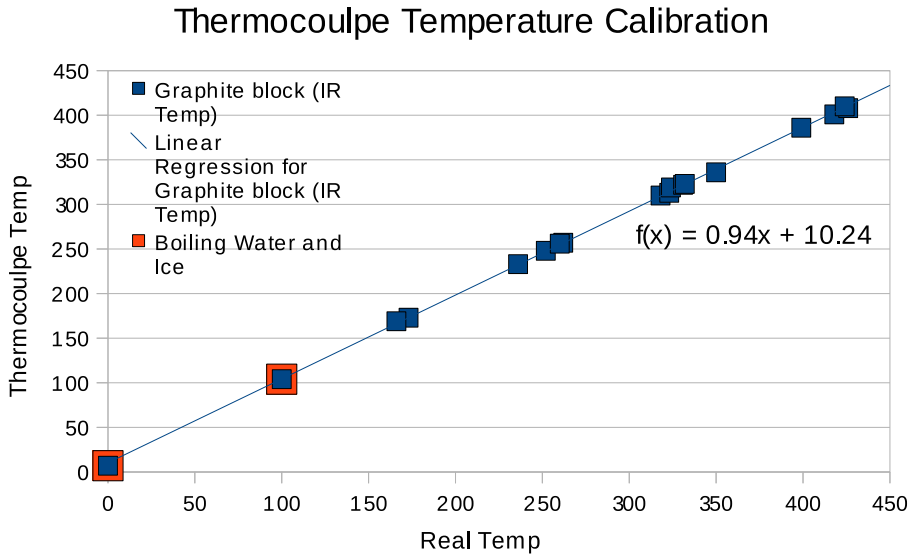

Figure 3.3: Calibration curve for the thermocouples. Note that the curve in highly linear.

Thermocouple Calibration

The type K thermocouples were calibrated by comparing their temperature to a known standard temperature. In this case the freezing and boiling points of water were used for initial calibration. For these, the thermocouples read 7 and 104 °C respectively. In order to perform the calibration at higher temperatures and ensure that a linear calibration would be sufficient, a thermocouple was attached to a cylindrical graphite block 1" thick and 4" in diameter. The graphite block was placed on to a hot plate and heated to different temperatures. The actual temperature of the block was measured with a Fluke 62 Mini Infrared Thermometer which is accurate to within $\sim$ 1.5 °C. The graphite was heated to temperatures ranging from 173 to 424 °C. The results from these calibrations are shown in figure 3.3.

Furnace Temperature Calibration

After a precise calibration for the thermocouples, it was then possible to determine the precise temperature of the sample and the Hg droplet inside the ampoule while in the

furnace. To achieve this, a calibration ampoule was made to simulate the temperature conditions for both the sample and Hg inside the ampoule. A fast drying porcelain cement was used to bond a thermocouple to the end of the ampoule in the position where the Hg droplet sits. To mimic the sample conditions, another thermocouple was bonded to a quartz insert and was placed inside the ampoule at a position indicative of where the sample would normally reside. One condition that could not be mimicked with this setup is that the samples would be sealed and annealed under a vacuum/Hg overpressure while the the thermocouples resided inside. It still remains unknown how the vacuum/ high Hg pressure (in excess of several atm for some temperatures) affects the temperature of the sample during the anneal. It is postulated that the high Hg pressure would lead to a more uniform temperature profile through out the ampoule due to convective heating. This is believed to be the case because gaseous Hg has a higher thermal conductivity than normal atmosphere.

To test the accuracy of the calibration ampoule, different metals (indium, tellurium, and zinc) were sealed into evacuated ampoules. The metals were placed on a piece of silicon and was sealed in the ampoules as if it were a sample. They were then loaded into the furnace and the temperature was incrementally increased until the metal melted. Due to the setup of the furnace it is difficult to visually observe the exact melting point, but the data obtained is judged to be accurate to within $5-10$ °C. Figure 3.4 show that the melting of the metals closely follows the temperatures measured using the test ampoule. It is noted that the melting point of tellurium was the most difficult to observe because during the test it sublimated and deposit onto the walls of the ampoule and partially obscured the view.

In addition to placing metals on a piece of silicon to represent sample temperature, metal were also placed at the end of the ampoule to represent the Hg. It was found that the melting point varied between the two. In the case of tellurium and zinc, a difference of 10 °C was observed between the melting of the metal placed at the Hg droplet and sample positions. Again, it is postulated that in a high Hg pressure the temperatures with in the ampoule will be more uniform. Thus, with an Hg over pressure the sample temperature

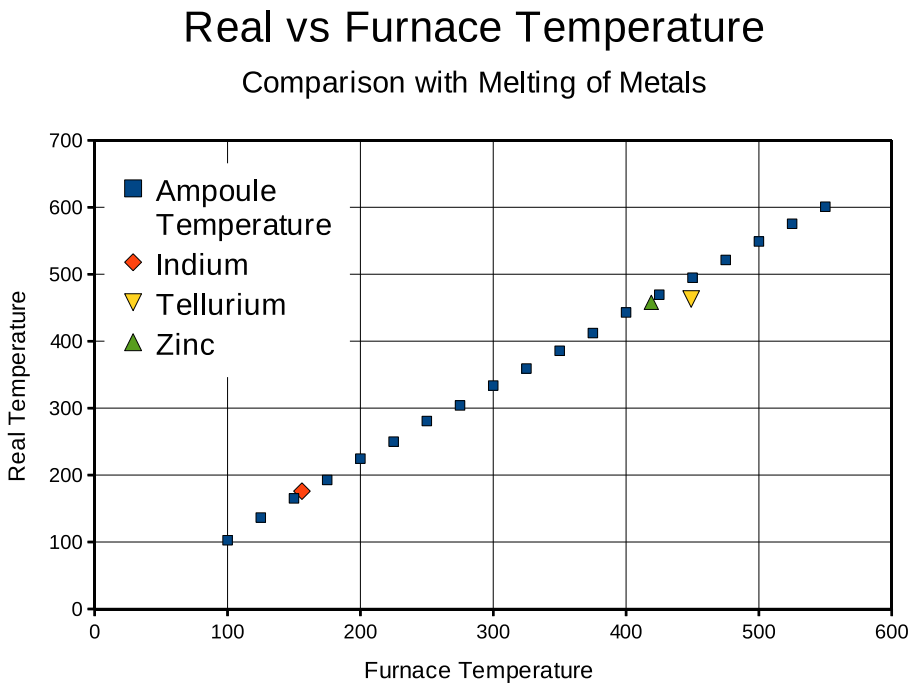

Figure 3.4: Calibration curve plotting the furnace set point temperatures compared with the temperatures from the calibration ampoule. Also included is the observed melting temperatures of different metals.

will be closer to the Hg temperature due to convective heating. Because these calibration experiments were performed in vacuum, there is a large temperature difference.

Position Calibration

The furnace is divided in to 3 zones, with zone 2 being in the middle (see figure 3.1). There is a 2 cm gap between the heating coils of each zone. This causes a temperature variation in the area near these gaps. For this profiling, all zones were set to the same temperature, and the ends of the furnace were left open. To measure this, a thermocouple was placed in an ampoule and moved across the furnace periodically measuring the temperature. The results are shown in figure 3.5. In an effort to prevent Hg from condensing on the samples, it is preferable to maintain the Hg at a slightly lower temperature than the samples. For this reason the optimal position was decided to be with the samples in the center of zone

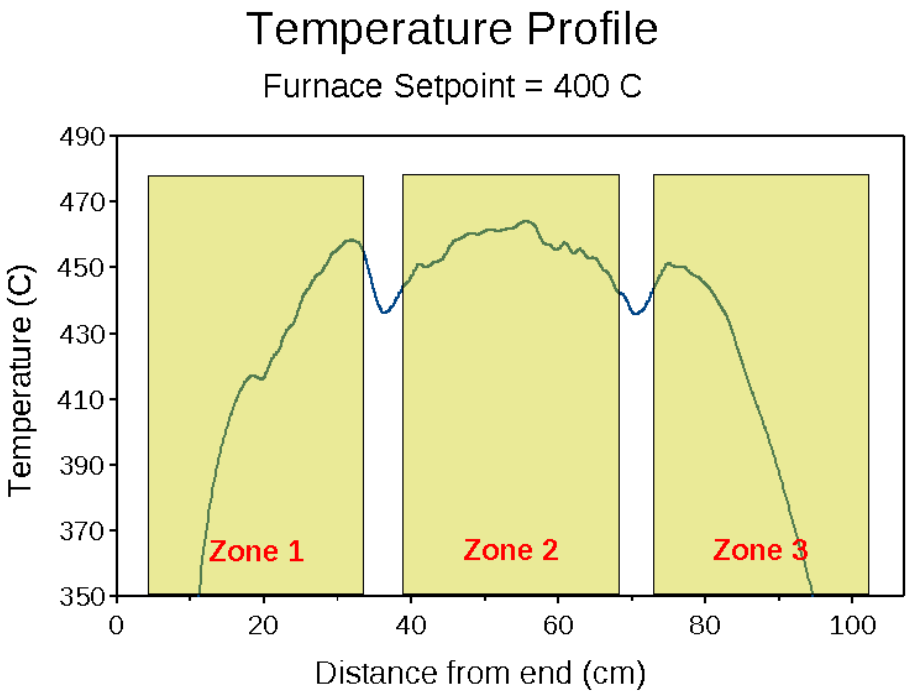

Figure 3.5: Comparison between the position of the ampoule and the resulting temperature for a fixed furnace set point. Temperatures are thermocouple temperatures rather than real temperature.

2, and the Hg sightly off center. All experiments that were performed have been with this positioning in mind.

Prior to the calibration, all anneals were performed by placing the ampoule directly on the furnace tube (close to the heating coils) and at the center of zone 2 of the furnace. All data obtained prior to the calibration has been modified to reflect the real temperatures within the system. One major concern about the previous process was the proximity of the ampoule to the heating coil. This was believed to cause the temperature to be higher than expected. The PID controllers and the SSR's control the furnace temperature digitally. Thus the heating coils were either on or off with max or no current. This caused a concern that the close proximity to the coils coupled with the digital control system would result in large variations in temperature during the heating process and while the furnace was maintained at a constant temperature. By placing the ampoule away from the heating

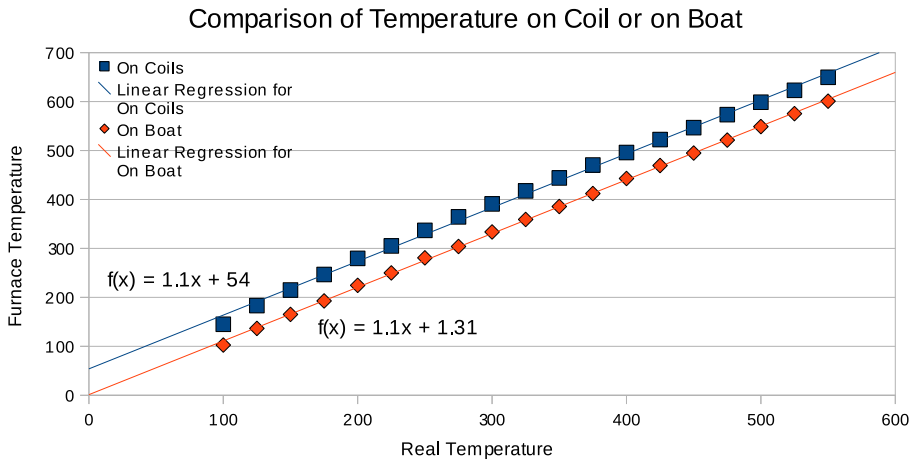

Figure 3.6: Comparison of furnace vs real temperature between placing the ampoule directly on the heating coils verse on a boat in the center of the furnace.

coils, the effect of the digital temperature control was mitigated.

Having decided that the optimal position for the samples would be in the center of zone two, both radial and longitudinal calibrations were performed to determine the sample temperature for both the old and new positions. A quartz boat was used to hold the ampoule near the radial center of the furnace (see figure 3.1). This position is believed to have the most consistent temperature. With the sample in the center of the zone, the calibration ampoule was used to compare the difference in temperatures between having the ampoule on the furnace tube verses the radial center of the furnace. Figure 3.6 shows the results of the real temperature verses furnace temperature when the ampoule is placed on the furnace tube verses the radial center of the furnace. The difference between the two positions is rather uniform (50 °C) within a furnace temperature range of 150 to 600 °C.

Chapter 4: In Situ Thermal Cycle Annealing of CdTe

The primary buffer layer used for HgCdTe growth is CdTe. In the cases of some semiconductor alloys (see examples in figure 1.2) the lattice constant will vary a significant amount depending on the composition of the alloy. In the case of CdTe and HgTe the lattice constant varies by only ~ 0.02 Å, and its variation is highly linear. This means that CdTe is nearly lattice matched to any composition of HgCdTe. In addition, their compositions are of the same elements, so there is no problem with diffusion of elements that would act as dopants.

Growth of HgCdTe on CdTe is not a simple issue, but the two layers are very compatible and that makes CdTe a buffer layer of choice for HgCdTe. But before CdTe/Si composite substrates is capable of sustaining high quality HgCdTe growth, the issues relating to CdTe growth on Si must be addressed. This is the reason why considerable effort has been made to increase the quality of CdTe on Si over the last two decades[2,18–22]. In this chapter the results of *in situ* growth interrupted thermal cycle annealing of CdTe on Si as a method of decreasing dislocation density and increasing buffer layer quality are presented.

4.1 CdTe Buffer layer

The large lattice mismatch (19%) between HgCdTe and silicon requires the formation of misfit dislocations at the interface in order to relieve strain. It not possible to achieve single crystal MBE growth HgCdTe layers directly on Si due to the disparity between the high temperature needed to achieve crystallinity and the low growth temperature required for Hg incorporation. Even if it were possible, the HgCdTe layer grown directly on silicon would result in layers with extremely high dislocation densities. For this reason a thick CdTe

buffer layer is used. Because CdTe is grown at a much higher temperature (290 °C) than that of HgCdTe(185 °C), it is much easier to grow single CdTe and obtain high quality layers. It is of great importance to obtain low dislocation densities in CdTe in order to subsequently grow high quality HgCdTe. A dislocation can only terminate at either a free surface or another dislocation. As a result, any threading dislocations in the buffer layer will continue to thread through the HgCdTe layer grown on the CdTe layer. Thus a low threading dislocation in the CdTe buffer layer is required in order to grow HgCdTe layers with a low defect density. Currently CdTe/Si substrates are used for state of the art SWIR and MWIR IRFPAs. [21, 23–25]

The 19% lattice mismatch between CdTe and Si presents a very difficult obsticle to the growth of high quality single crystal CdTe layers. Several techinques are used in standard CdTe growth in order to achive this goal. Techniques include deposition of intermediate layers (ZnTe and/or Ge) to help ease the lattice mismatch, using arsenic to passivate the intrinsic step morphology of the (211) Si surface, and optimization of growth parameters[2, 19, 20, 26, 27]. In this work *in situ* TCA as a means to further improve CdTe/Si quality and better understand dislocation dynamics during growth was studied.

In order to determine the quality of a CdTe/Si layer several techniques are used. The standard metrics of a good layer are a low EPD, low x-ray rocking curve FWHM, and a smooth surface that is relatively free of growth related defects. It has been found that the proper growth conditions and use of an intermediate ZnTe ($20 - 60$ Å) buffer layers and arsenic passivation are capable of producing layers with an EPD as low as $\sim 1 \times 10^7$ cm^{-2} and a FWHM of the (422) rocking curve of ~ 110 arcsec.

The rest of this chapter will be focused on a brief overview of the important standard practices and optimization that impact the growth of high quality CdTe layers. In addition particular attention is given to the characterization and comparison of *in-situ* cycle annealed materials, and showing that cycle annealing can be used as an important method to further improve crystal quality, and reduce dislocation densities.

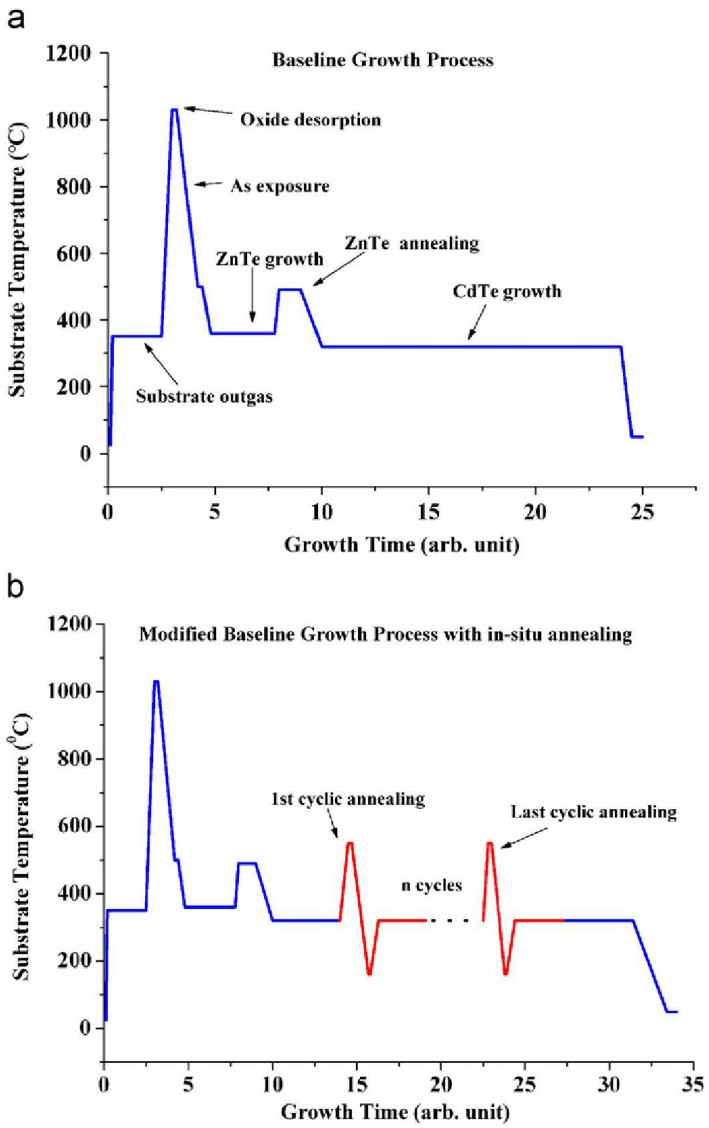

Figure 4.1: Temperature profiles of a baseline (a) and a baseline with in-situ cyclic annealing (b) growth process of CdTe on Si by MBE.

4.2 CdTe Cycle Annealing

4.2.1 Experimental

Three-inch Si(211) substrates were cleaned using a standard RCA cleaning process for Si wafers. This process cleans the surface and leaves an approximately 12 Å thick oxide layer

on the surface. The oxide layer is thermally removed in the growth chamber by raising the temperature above 850 °C prior to growth. The surface was then passivated with arsenic and a thin ZnTe layer was deposited. After the deposition of the ZnTe buffer, a CdTe seed layer was deposited on to the sample to a thickness of ~ 3 μm. Growth was then stopped and the temperature was raised to the annealing temperature. In order to maintain a good surface morphology the high temperature annealing was done under a Te flux (ie. overpressure). After 5 minutes of annealing the sample was allowed to cool to below the growth temperature ($\sim$ 160 °C). The sample was then heated to the growth temperature, after the temperature stabilized, CdTe growth was resumed. After an hour, growth was interrupted again in order to perform another annealing cycle. A schematic of the normal and cyclical annealing process is depicted in figure 4.1.

After completing all *in situ* annealing cycles, growth was continued until the thickness of the layer was approximately 9 μm thick. The thickness was kept constant so that any small changes in the stress from layer thickness would not effect the dislocation density study. All samples were grown with the CdTe flux calibrated to yield a growth rate of ~ 1.6 μm/hr, this metric was used to determine the growth time needed to reach 9 μm.

Ten consecutive growth runs were performed with different numbers of annealing cycles in order to determine what effect the number of cycles has on the dislocation density. The growth runs were performed consecutively to minimize variations that might occur over the course of a campaign. The layers were characterized using double crystal x-ray diffraction (XRD), EPD, and low temperature photoluminescence (PL) measurements.

XRD measurements of the layers were taken prior to any dicing of the wafer to ensure that resulting mechanical damage would not affect the results. A small sample was then cleaved from the wafer and the EPD was measured using the Everson etch (see section 2.6.1). The density was determined by manually counting pits using a Nomarski optical microscope.

Low temperature photoluminescence was performed on select samples by Naval Research Labs in an effort to explore the correlation between the 1.47 eV defect peak and measured

EPD. Samples were cleaned with an acetone methanol rinse and loaded in to an Oxford Microstat He cryostat. Samples were excited with the 808 nm line of a diode laser and the light emitted by the samples was dispersed and measured by a Princeton/Acton Trivista 557 triple spectrometer and measured by a liquid nitrogen cooled InGaAs detector.

Some samples were chosen to measure the EPD depth profile. For this purpose, many small samples (7×7 mm) were diced from the same general area of the wafer and etched with a 0.05% bromine methonal solution. The etch time was varried in order to remove different amounts of material from each sample. The layer thickness was determined by measuring their FTIR fringe effect. The samples were etch using the Everson etch and the EPD of each sample was then measured.

4.2.2 Results and Discussion

EPD of CdTe

The effects of the number of annealing cycles on dislocation density was explored by performing several growth runs, and varying the number of cycles from 0 to 15. This results in a clear exponential decrease in the measured EPD with respect to the number of annealing cycles as can be seen in figure 4.2. The results also show that a saturation seems to occur after about 10 cycles. In addition to testing the effect of the number of cycles, this study looked at the length of the annealing cycle. For a short length of 1 minute it can be seen that the annealing is slightly less effective than with 5 minutes, but still comparable in it's result. The layer grown with an extended annealing duration (10 min) did not show as much EPD reduction. At first glance, these results are counter intuitive, the expected results should be that the longer the duration the more reduction in EPD. To explain this conflict, it should be noted that with all other growth parameters the same, the layer with the longer annealing duration was measured to be a micrometer thinner than layers grown using the standard annealing duration. It is suspected that the longer anneal lead to a prolonged desorption phase during each annealing cycles. The desorption phase is believed to

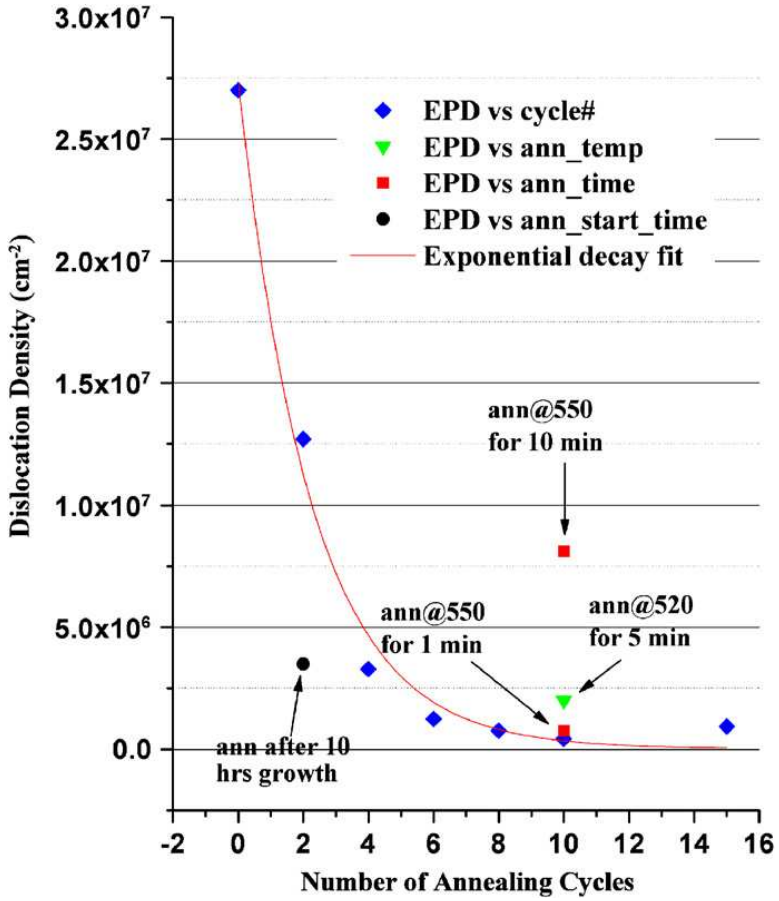

Figure 4.2: Surface dislocation densities of CdTe/Si layers grown with different in-situ annealing cycles and other annealing conditions as represented by the Everson etch. Dash line is exponential trend line fit to the data points labeled EPD vs. cycle #.

have roughened the surface and caused other crystal damage. As a result, longer annealing time generated new dislocations when CdTe growth was resumed.

One point that comes up often, and it should be mentioned before moving on is that EPD is not a perfect method of determining dislocation density. In practice, CdTe quality is mainly judged by two factors, x-ray rocking curves and Everson EPD results. Both metrics have their own flaws and virtues. As mentioned in section 2.6.1 the Everson etch leaves the CdTe surface with a rough surface in addition forming etch pits. It has been shown that the surface has a rough enough texture that small etch pits can be rendered invisible when viewed with Nomarski microscopy. It remains an open question as to if the pits that are

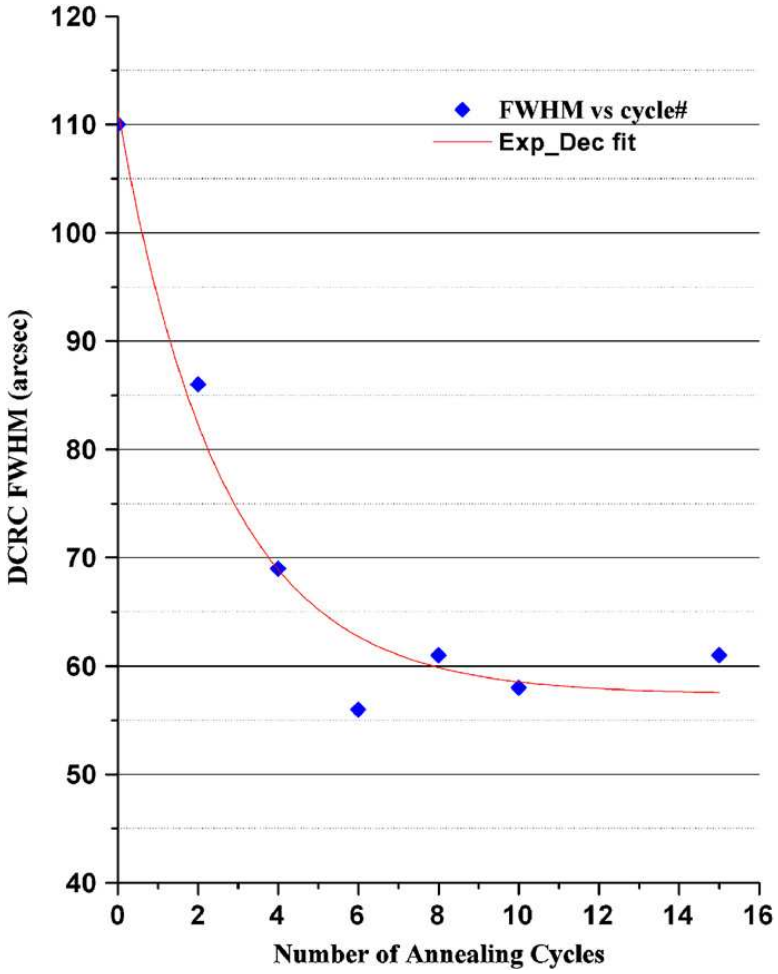

Figure 4.3: X-ray FWHMs of CdTe layers as a function of the number of in-situ annealing cycles.

hidden are due effects directly related to the surface roughness seen, or if they are simply a different class of dislocation than as the larger pits (different burgers vector or line vector).

X-Ray Analysis of CdTe

EPD is the foremost metric used for determining the quality of a CdTe layer due to it's simplicity and the lack of a need for costly equipment. As mentioned earlier, it is not an ideal characterization technique due to the subjectivity of the counting, variations in microscopes, and possible variations in etching solutions and times. Additionally, EPD is

a destructive characterization technique. There is always a desire to find a better form of characterization, one that is both non-destructive and completely non-subjective. One metric used is the full width at half maximum (FWHM) measurement of double crystal rocking curves (DCR) of the (422) plane. The broadening of the DCR is caused by several factors, but in the case of CdTe the primary factor is the dislocation density. Unfortunately using x-ray diffraction for quantitative measurements of dislocation densities has not been fully developed, but the data can be used for qualitatively comparison.

Our DCR curves were all taken from the symmetric (422) plane with the projection of the beam in the $[1\bar{1}0]$ direction which provides for the smallest FWHM possible. Figure 4.3 shows the x-ray rocking curve FWHM with respect to the number of cycles performed during the growth of CdTe/Si layers. An exponential decrease in the FWHM is observed as the number of annealing cycles increased from 0 to 6 cycles though it remains roughly the same for 6 or more cycles at ~ 60 arcsec. It has been shown that the dislocation density is roughly related/proportional to the square of the FWHM of the DCR.[10, 11] Using the numbers in figure 4.3, this corresponds to a decrease in dislocation density by roughly an order of magnitude. This is less than the decrease reported by EPD, the disparity could be due to the insufficiency of the Everson etch in measuring low dislocation densities[1]. Another explanation is that the subsurface dislocation density is much larger than that at the surface. Because the x-rays used in DCR measurements penetrate to a thickness of ~ 7 μm, thus dislocations that are not at the surface of the sample would effect the FWHM while not being detected by an EPD etch.

Photoluminescence of CdTe

Photoluminescence (PL) is a process which gives information about the defects in the semiconductor material. In this technique, a sample is bombarded with photons of a specific wave length, and then the luminescence emission of different wavelength associated with

[1] Evidence has shown that the Benson EPD etch could be a more accurate means of measuring dislocation density, but particular study wan performed in 2006, while the Benson etch was not developed till 2008.

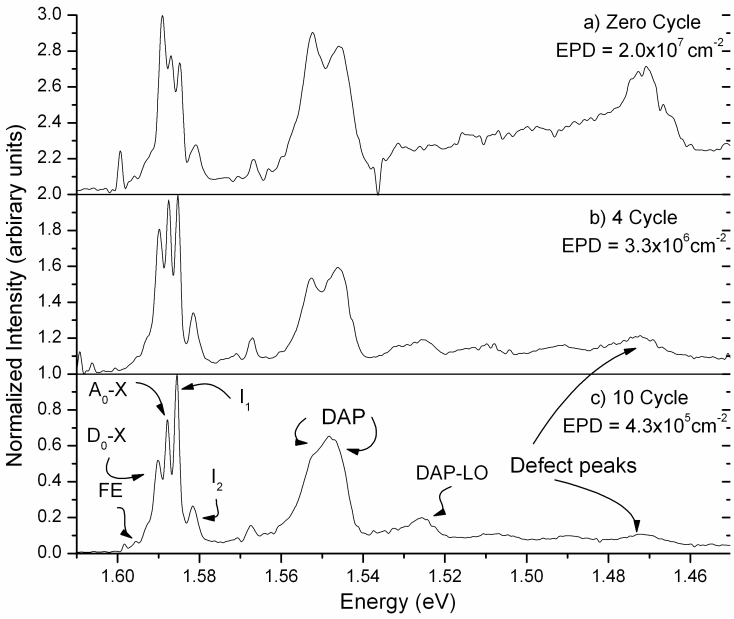

Figure 4.4: Normalized low-temperature (4 K) photoluminescence spectra of CdTe/Si layers grown with 0, 4, and 10 *in situ* cycles of annealing.

different defects are recorded. Using this method it is possible to probe the various energy levels within the band gap and gain knowledge about dopants, defects, dislocations, and other electrically active characteristics of the sample.

For CdTe it has been shown that the near band edge peaks correspond to different Cd and Te acceptor and donor levels ($A_0 - X$ and $D_0 - X$), followed by the ionized acceptors and donors (I_1 and I_2). Beyond that the donor-acceptor pair (DAP) transitions and their phonon replicas (DAP-LO) appear. By using wide spectrum PL at low temperature, it is also possible to see another broad peak located at 1.47 eV. This peak has been shown to correspond to dislocations within the crystal. The intensity of this peak can be correlated qualitatively to the dislocation density. [18, 28–30]

Figure 4.4 shows the normalized PL spectra of CdTe samples that were grown with zero, 4, and 8 annealing cycles. The most strikingly different feature between the spectra in Figure 4.4 is the peak at 1.47 eV. The difference can be clearly seen when comparing the spectra of figure 4.4(a) with (c), which are associated with zero cycle annealing and 8 cycles

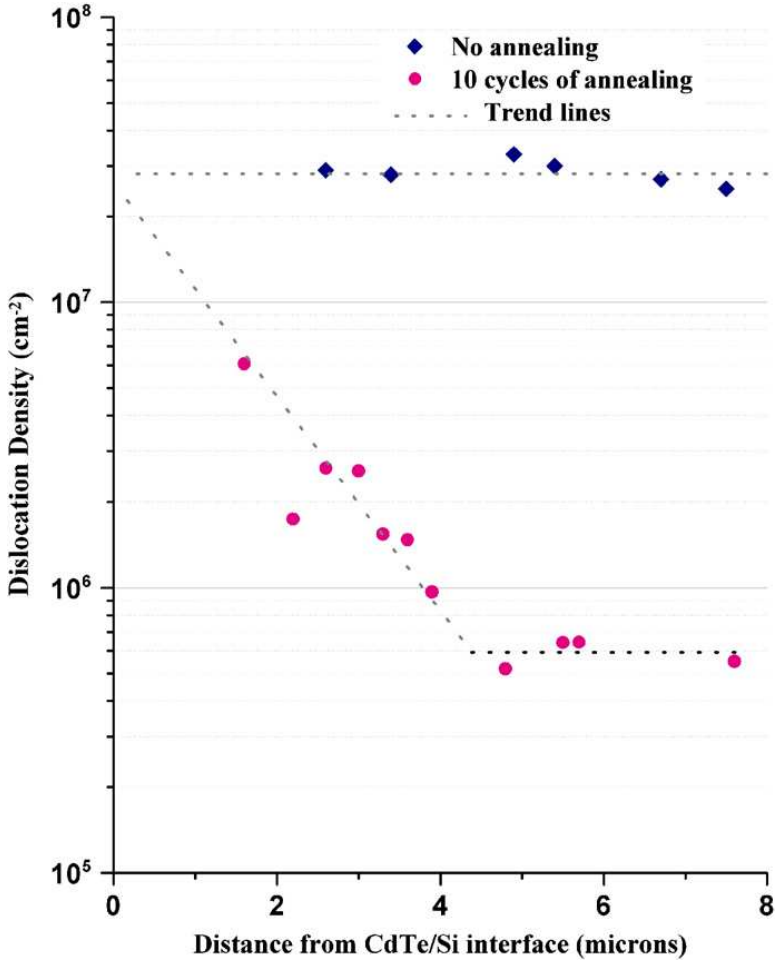

Figure 4.5: EPD verses the distance from the CdTe/Si interface for a sample with no annealing cycles compared to 10 cycles of annealing. The dotted lines show the linear and exponential trend lines that appear within the data.

annealing, respectively. It can be seen that the intensity of 1.47 eV peak also decreases as the number of annealing cycles increases. The PL results correlate well with the results obtained by EPD and XRD studies shown in figures 4.2 and 4.3, respectively.

EPD Depth Profile

EPD by its nature reveals information only about dislocations that intersect the surface. In order to understand the effects of TCA through out the bulk of the crystal more inventive techniques must be used. For this reason, EPD depth profiling was carried out on select

samples. The samples used in this study were cleaved from the same area of the wafer, care was taken that edge pieces were not used. This was done in order to minimize any effect of non-uniformity that might exist and/or edge effects. More data points were taken for the profiling of the layer with 10 annealing cycles in order to obtain a clear picture of the EPD depth profile.

The dislocation density of the layer that did not undergo any annealing cycles appears as expected. The majority of threading dislocations that form at the CdTe/Si interface extend to the free surface with little to no interaction. This can be seen in figure 4.5 where it is shown that the EPD throughout the crystal depth remains constant. In contrast, the EPD depth profile of the annealed sample shown in figure 4.5 can be divided into two distinct regions. At the CdTe/Si interface the EPD data is projected to be the same for annealed and unannealed samples. In the center of the layer, an exponential reduction of the EPD with depth is clearly seen. The top $\sim$ 3 μm of the layer has an EPD that is roughly constant.

The data in the EPD depth profiling strongly support the half-loop relaxation model of dislocation annihilation presented in section 2.5. During the annealing process dislocations are given enough energy that they move, interact, and form half-loops. Because the dislocations no longer terminate at the surface, the half-loops then attempt to minimize their energy by relaxing towards the interface. Because the material has a large number of dislocations, the half-loops will interact with each other inhibiting further relaxation. The exponential decay region of EPD in figure 4.5 supports this hypothesis. Beyond the exponential decay region, the dislocations extend to the surface. Theory suggest that these remaining dislocations did not interact with other dislocations to form half loops or they coalesced to form a single immobile dislocation, and thus the EPD remains constant throughout the top 3 μm of the layer.

Chapter 5: Ex Situ Thermal Cycle Annealing of HgCdTe

5.1 Introduction

Chapter 4 presented the effects of *in situ* TCA on CdTe/Si layers, where multiple annealing cycles are performed intermittently during the growth process itself. It is seen that TCA is an effective means to reduce EPD and improve overall crystal quality for CdTe/Si. By using cyclical *in situ* annealing, it has been observed that the dislocation density in CdTe/Si layers can be reduced down to a saturation point of mid 10^5 cm^{-2}.

A similar *in situ* cycle annealing on HgCdTe/GaAs at $350-490$ °C resulted in an EPD of $(2-4)\times10^6$ cm^{-2} from base line growth value of $(9-20)\times10^6$ cm^{-2}[31]. Due to the high mercury overpressure needed to maintain the surface morphologies and composition of HgCdTe, a cap layer of ZnTe or ZnSe was used for these annealing experiments. Shin et al[32] reported EPD reduction of HgCdTe/GaAs using ex situ TCA, where annealing is performed outside the growth system and the epilayer is not specially capped. The surface morphology was maintained using a high mercury overpressure. This method of cycle annealing was reported to be effective at reducing the EPD in HgCdTe/GaAs to mid 10^5 cm^{-2}.[32][33]

In this chapter the results of *ex situ* thermal cycle annealing (TCA) of HgCdTe/CdTe/Si is presented. In this study, the EPD and overall crystalline quality with respect to annealing temperature, number of annealing cycles, total annealing time, pre-annealed EPD/crystal quality, Cd composition, buffer layer quality and buffer layer lattice constant are examined. For comparison, the effects of TCA on the HgCdTe layer grown on lattice matched ($x \approx 0.04$) $Cd_{1-x}Se_xTe$/Si substrates and also on bulk lattice matched ($x \approx 0.04$) $Cd_{1-x}Zn_xTe$ substrates is also examined.

5.2 Experimental

The majority of samples used in this study were grown by MBE on composite CdTe/Si substrates, exceptions are noted where relevant with in the text. The HgCdTe growth was performed at $\sim$ 185 °C with a growth rate of $\sim$ 2 μm/hr. Typical HgCdTe layer thicknesses used in these experiments was between 8 and 10 μm thick. The majority of the $Hg_{1-x}Cd_xTe$ layers used in these experiments had x value of $\sim$ 0.21 (intended for LWIR application), but both $x \approx 0.33$ (for MWIR) and $x \approx 0.40$ (for SWIR) were also used for comparison.

5.2.1 *Ex Situ* TCA Process

HgCdTe/CdTe/Si samples were cleaved into small pieces ($\sim$ 7 mm $\times$ 7 mm) and sealed in a quartz ampule with enough Hg to ensure saturation pressure throughout the course of the anneal. The ampules were then placed into the center of a 4.5-inch Lindberg three-zone open tube furnace and annealed under various conditions. The furnace temperature was carefully calibrated to determine the temperature of the samples as outlined in section 3.1.2. It is worth noting that the temperatures quoted through out this work are the real temperatures according to the calibration. Though they seem arbitrary, the initial experiments were performed using the furnace set points, and were later calibrated to be the real temperatures. Furnace set points of 400, 450 and 500 °C translate to a real temperature 441, 494, and 551 °C, respectively.

The TCA process consists of raising the temperature to the maximum annealing temperature over the course of $2-5$ minutes. Using an extended ramp time ensures that Hg does not heat significantly faster than the sample and subsequently causing mercury condensation on the surface. The slow ramp rate was used mainly for the higher temperature anneals and was found to be one method of preventing surface damage due to condensation. The maximum annealing temperature was varied between 385 and 600 °C depending on the experiment. This temperature was maintained for 5 minutes. The furnace was then allowed to naturally cool to 250 °C and maintained at that temperature to ensure that equilibrium

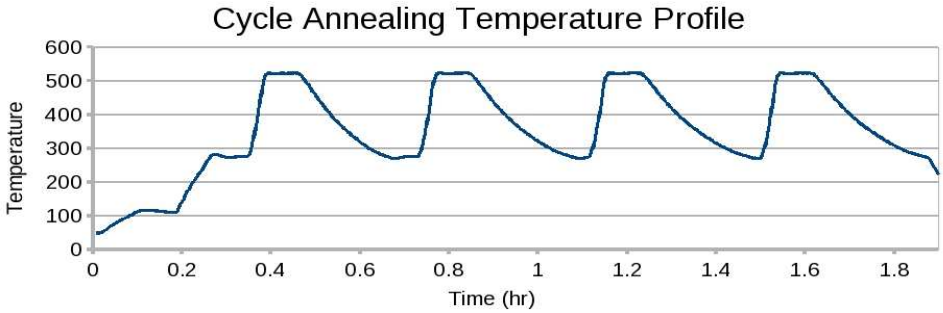

Figure 5.1: Temperature data from a standard four cycle annealing run

was reached. A typical cooling time was $10 - 20$ minutes depending on the maximum annealing temperature. The process was then repeated several times, after the final cycle the ampoule was removed, opened, and the samples characterized. The ampoules were removed by either allowing the furnace and ampoule to cool to room temperature before removing, or the ampoule was removed from the furnace at 250 °C and quenched in a water bath, no effective difference was observed between these two processes. The temperature verses time plot of a four cycle annealing process is shown in figure 5.1.

5.3 TCA - Results and Discussion

5.3.1 Surface Morphology

All TCA experiments are performed well above the HgCdTe growth temperature. In order to prevent excessive Hg outdiffusion it is necessary to anneal the samples under a high Hg overpressure. This was achieved by placing an amount of Hg in the ampoule with the samples. In order to preserve surface morphology it is necessary to have an overpressure of Hg that is roughly equal to the saturation pressure, which is $\sim$ 4, 8, and 14 atm at 450, 500 and 550 °C respectively. In order to achieve this level of Hg overpressure it is necessary to use several hundred μL of Hg. After an anneal the surface is smooth and there is a noticeable increase in cross-hatching, this can be seen in the before and after image of a sample in figure 5.2(a) and (b). This effect is believed to be a sign of strain relief within the

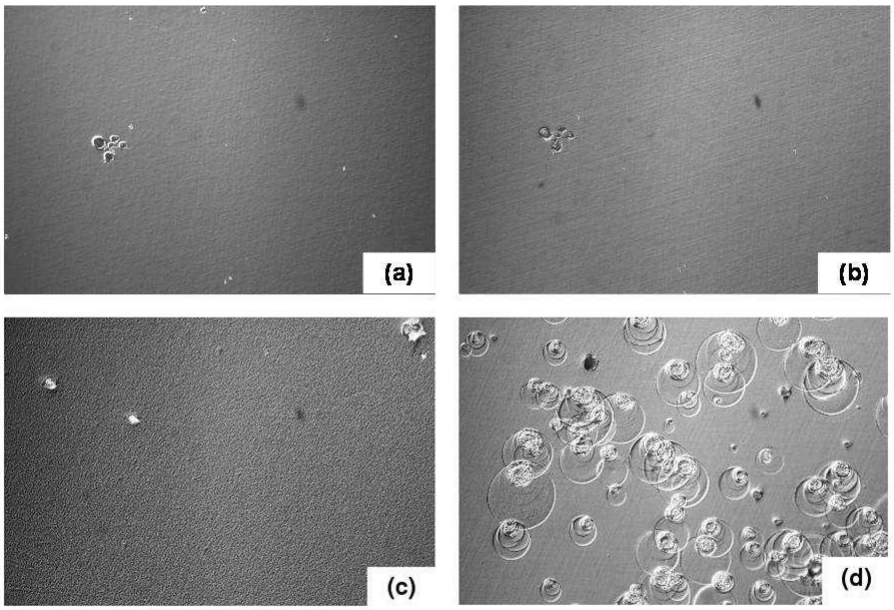

Figure 5.2: Surface morphology of HgCdTe/Si samples: (a) As-grown and (b) thermal cycle annealed with sufficient Hg overpressure of the same sample, (c) TCA with insufficient amount of Hg overpressure, (d) TCA that resulted in Hg condensation on the layer. Note, images (a) and (b) are the same sample at the same position before and after annealing.

crystal. If an anneal is performed with insufficient Hg overpressure, the surface becomes roughened by the anneal as in figure 5.2(c).

The surface morphology can also be effected by Hg droplets condensing on to the layer. This will leave concentric circular marks where the Hg drop forms and evaporates away as seen in figure 5.2(d). Hg condensation generally occur when the sample is cooler than the Hg in the ampoule. It was shown in section 3.1.2, that the annealing set up used gives a temperature difference of $5 - 10$ °C. Yet during the heating and cooling of the sample it is possible for the Hg droplet to heat faster than the sample, causing condensation to form. Several methods are commonly used to prevent this sort of damage. The use of an extended ramp rate will allow for a more uniform heating and cooling of the sample and Hg. It was also found that condensation could be partially prevented by placing the sample face down either directly on the inside bottom surface of the quartz ampoule or onto a clean piece of silicon. No detrimental effect on the EPD was observed using either of these techniques. Placing the samples face down on the ampoule inner surface typically resulted in damage to the edges where the HgCdTe layer was in contact with the quartz. By putting the sample surface in close proximity to a piece of silicon, no HgCdTe surface is exposed and hence Hg condensing during cool-down will not condense on and damage the sample's surface. This technique also did not show the edge damaging effects that we saw when the sample was placed directly on the ampoule inner surface. Using these techniques combined with an extended ramp rate, it is possible to ensure that Hg condensation will not effect the surface of the sample.

5.3.2 Dislocation Density Reduction

Saturation Limit

The goal of cycle annealing is to reduce the dislocation density in HgCdTe/Si layers to a level comparable to HgCdTe/CdZnTe. Thus one of the foremost questions to answer about TCA is to what level the dislocation density can be reduced. The resulting EPD of TCA was

Temperature	Avg. EPD (cm^{-2})	Standard Deviation
494 °C	1.2×10^6	5.2×10^5
551 °C	1.6×10^6	7.2×10^5
604 °C	1.4×10^6	3.2×10^5

Table 5.1: EPD after 4 cycle annealing at different temperatures. The as-grown EPD of the samples used for this set of experiments was in the range $6 \times 10^6 - 1 \times 10^7$ cm^{-2}.

examined as a function of annealing temperature at 494, 551, and 604 °C, using four or more annealing cycles. Experiments at each temperature were repeated many times on different samples. Table 5.1 shows the summary of the results for the three annealing temperatures, using samples with an as-grown layer EPD of $6 \times 10^6 - 1 \times 10^7$ cm^{-2}. The results of table 5.1 show that the annealing temperature (within this range) has little effect on the final EPD of a sample. While there is evidence to suggest that high temperatures might provide more consistent EPD results, the high temperatures make it difficult to maintain a good surface morphology, and it is not uncommon to have Hg condensation issues.

TCA performed at temperatures $T \geq 494$ °C showed that 4 or more annealing cycles was sufficient to reduce EPD to the saturation level of 1×10^6 cm^{-2}. TCA experiments using 8 to 16 cycles did not show further reduction beyond this point regardless of temperature.

Several different parameters were varied in order to understand the 1×10^6 cm^{-2} EPD saturation limit. Early experimentation was performed on samples cleaved from the same $2 - 3$ wafers. In order to explore the effect of the many different sample characteristics, a multitude of different samples from different growth runs were subjected to TCA experiments. The results of this comprehensive annealing study are shown in Fig. 5.3. Almost 50 samples taken from over a dozen different layers were subjected to 4 or more TCA cycles at $T \geq 494$ °C. It can be clearly seen that, the as-grown EPD of the sample has little to no effect on the post annealed EPD value that was measured, within the as-grown EPD range used in this investigation. The post anneal EPD of all samples in Fig. 5.3 has an average value of 1.5×10^6 cm^{-2} with a standard deviation of 0.5×10^6 cm^{-2}. This is in contrast to the work done by Arias et al[34] where a correlation between as-grown EPD and post annealed EPD was observed. This difference could be due to the absence of multiple

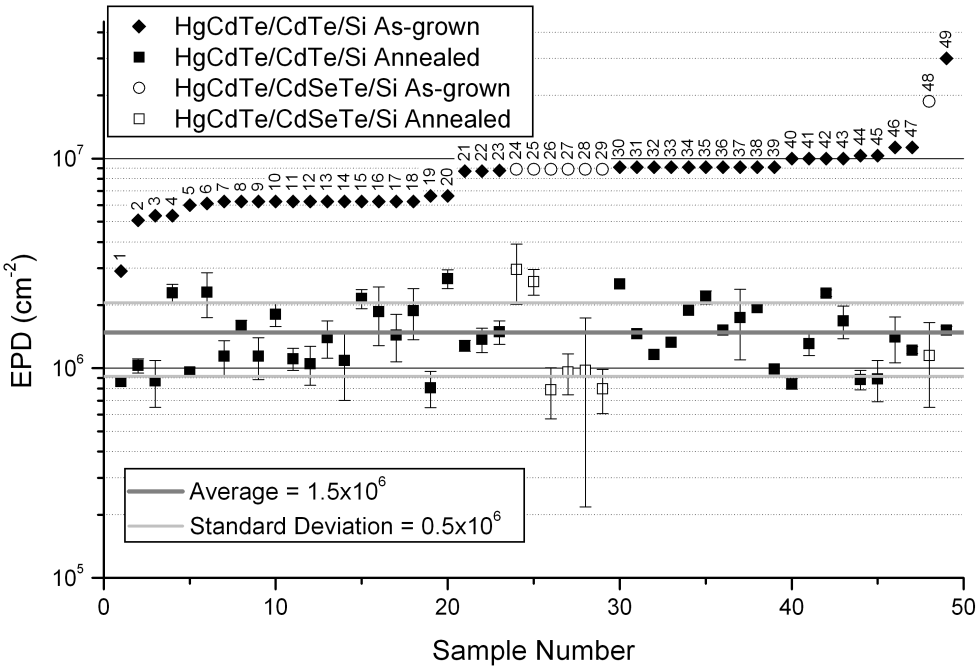

Figure 5.3: Depiction of TCA experimental data of 49 samples from 13 different layers. The EPD values before and after TCA of each sample are shown. All anneals were performed at a temperature $T \geq 494$ °C and used 4 or more cycles.

annealing cycles employed in their study. Possibly implying that those samples did not reach their final EPD saturation point.

While the variation in as-grown HgCdTe EPD ranges from 3×10^6 to 3×10^7 cm^{-2}, the variation in the as-grown CdTe buffer layer EPD is rather large ranging from 2.5×10^5 to 3×10^7 cm^{-2} as measured using the Everson etch (not shown in the figure 5.3). The EPD of a typical as-grown HgCdTe layer shows little correlation with the EPD of as-grown CdTe buffer layer, except for when the as-grown CdTe EPD is greater than mid 10^6 cm^{-2}, at which point the minimum as-grown HgCdTe EPD mimic the as-grown CdTe EPD. In spite of 2 orders of magnitude variation in the as-grown CdTe buffer layer EPD, there is no apparent correlation between the post-annealed HgCdTe EPD and the as-grown CdTe buffer layer EPD. This is evident from Fig 5.3 where the results of samples such as sample #23, with a as-grown CdTe EPD of 1.2×10^7 cm^{-2} (not shown), showed HgCdTe EPD reduction to the same range as other samples; such as 21, 22, 46 and 47; which have an as-grown CdTe buffer layer EPD of 4.6×10^5 cm^{-2} (not shown); and samples 7 through 18, which have an as-grown CdTe buffer layer EPD of 1.1×10^6 cm^{-2} (not shown). At this time, it is not clear as to what effect the TCA has on the buffer layer EPD, though *ex situ* TCA experiments on CdTe/Si show that a much higher temperature is needed in order to achieve significant dislocation motion and reduction. Based on the results of this study it appears that the dislocation reduction by TCA occurs regardless of the origin of the dislocations, whether they nucleate from the CdTe/Si interface or from the HgCdTe/CdTe interface.

Dependence of EPD on the Number of Cycles

To understand the reduction in EPD seen in TCA experiments it is necessary to examine how EPD relates to the number of annealing cycles used. Figure 5.4 shows the variation of EPD as a function of number of annealing cycles at $T = 494$ °C. An initial exponential decay followed by a saturation of the EPD at $\sim 1 \times 10^6$ cm^{-2} after 4 cycles is observed. This is in contrast to results by Shin et al[32] who saw a further reduction of EPD in

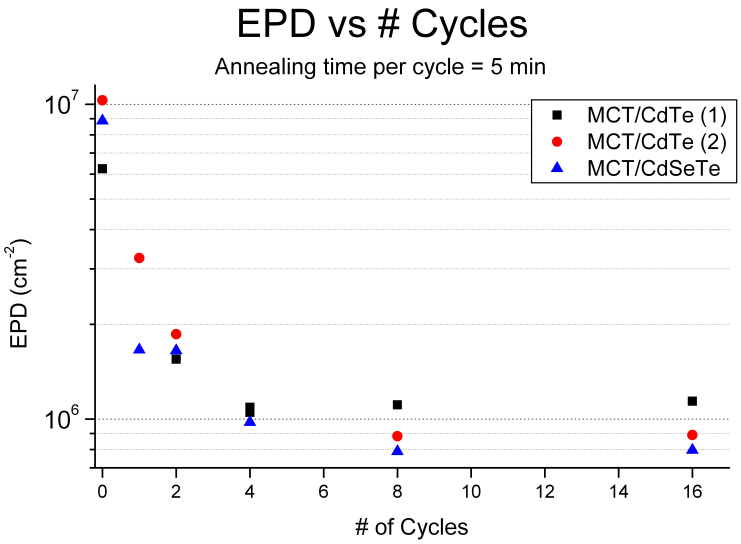

Figure 5.4: Variation of EPD with number of annealing cycles for an annealing time of 5 min per cycle and an annealing temperature of 494 °C.

HgCdTe/GaAs for 8 cycle annealing when compared to 4 cycle annealing. The additional reduction with more than 4 annealing cycles is believed to be due to the lower annealing temperature that they used. Results of cycle dependence of TCA at lower temperatures is presented later in this chapter. In addition, J. M. Arias et al[34] and S. H. Shin et al[32] used the Chen etch rather than Schaake etch for EPD measurement. A comparison between the two etches shows a difference of a half an order of magnitude[15]. The difference in the EPD etch used accounts for the lower ($\sim 5 \times 10^5$ cm^{-2}) EPD that they observed.

Figure 5.5 shows the variation of EPD as a function of number of annealing cycles at $T = 441$ °C. As with figure 5.4 an exponential reduction in EPD is observed down to the $\sim 1 \times 10^6$ cm^{-2}, though in the case of the lower temperature, 16 annealing cycles are needed in order to achieve this. The necessity of more annealing cycles to reach the saturation limit at lower temperatures suggests that fewer annealing cycles are needed at higher temperatures. This is confirmed as is shown in figure 5.6, TCA performed at $T = 551$ °C, the EPD can be seen to saturate after only $2 - 3$ annealing cycles.

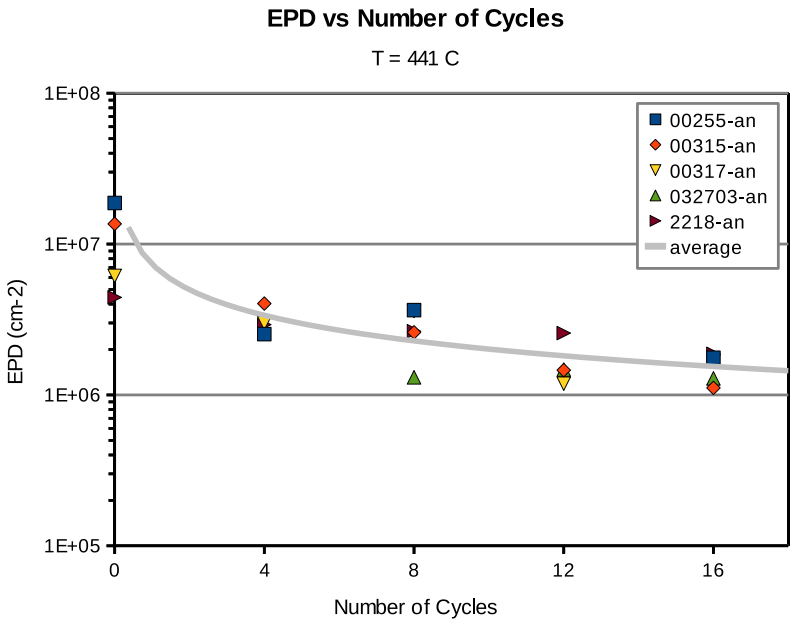

Figure 5.5: Variation of EPD with number of annealing cycles for an annealing time of 5 min per cycle and an annealing temperature of 441 °C.

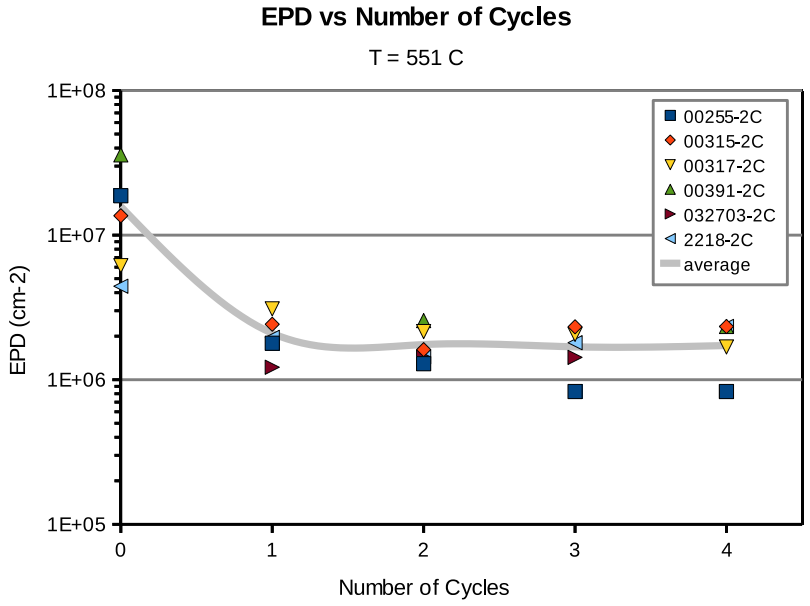

Figure 5.6: Variation of EPD with number of annealing cycles for an annealing time of 5 min per cycle and an annealing temperature of 551 °C.

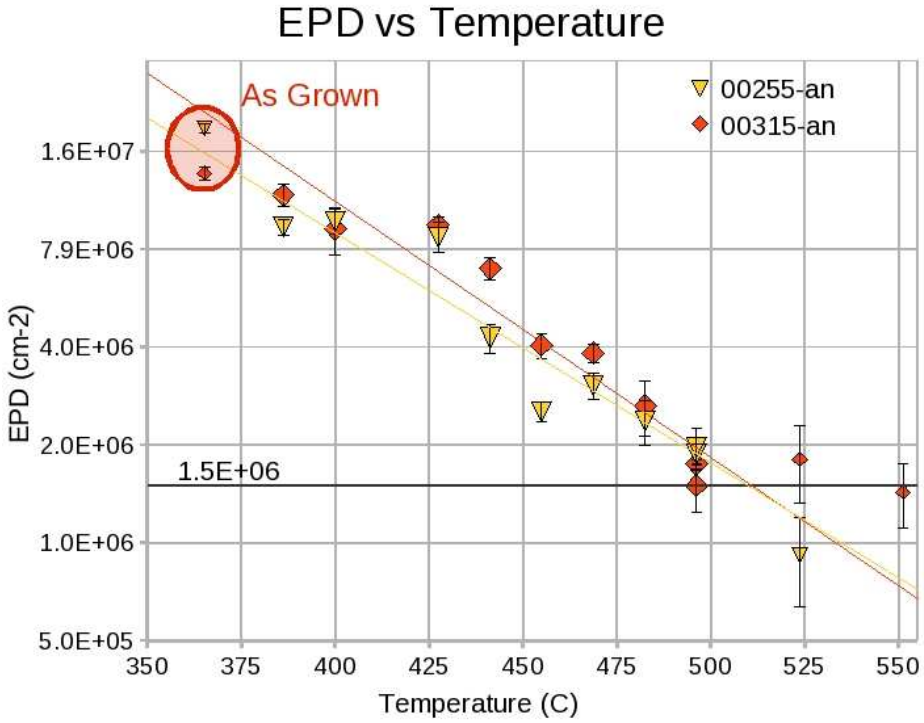

Figure 5.7: Variation of EPD with annealing temperature for four cycle TCA processed samples. The data points labeled "As Grown" do not correspond to an annealing temperature, but rather are placed in the extrapolated position of the exponential curve.

Dependence of EPD on Annealing Temperature

In order to understand and parametrize the TCA process it is necessary to systematically examine the effects of temperature on dislocation reduction. A set of experiments were performed at annealing temperatures varying from 385 to 550 °C. All anneals used four cycles and had a ramp time and wait time of 5 minutes. It is evident in figure 5.7 that there is a strong exponential relationship between annealing temperature and EPD. Extrapolation of this data suggests that dislocations are immobile for a temperature lower than $\sim$ 360 °C. Temperatures higher than $\sim$ 500 °C result in EPD values at the saturation limit, and further increases in temperature do not result in any more reduction in the EPD values.

5.3.3 First Order Modeling of Dislocation Reduction

A simple understanding of the relationship between dislocation density and temperature can be drawn from the temperature dependency of dislocation velocity. The first order reaction equation for dislocation annihilation is used as a simple model for the annealing results. The reaction equation can be written as

$$\frac{\mathrm{d}D}{\mathrm{d}t} = -k_1 D t, \tag{5.1}$$

where D and k_1 are the dislocation density and rate constant, respectively, with t being time.[35] This means that the rate of dislocation reduction is proportional to the product of current dislocation density and annealing time. Solving for the dislocation density gives

$$D = D_o e^{-k_1 t}, \tag{5.2}$$

where D_o denotes the as-grown the dislocation density and satisfies the boundary conditions. In this model t is representative of the number of annealing cycles. In this formulation, the rate constant (k_1) is proportional to the average velocity of the dislocations.[36] The average dislocation velocity can be expressed as

$$v_{avg} = v_o e^{\frac{-E_a}{k_b T}}, \tag{5.3}$$

where k_b is Boltzmann's constant, E_a is the activation energy, T is temperature in kelvin, and v_o is the intrinsic velocity of the dislocations. Generally v_o can have it's own temperature dependence but this is small compared to the exponential factor in equation (5.3). Over a small range of T, v_{avg} can be approximated as a linear function of T. The "small" temperature range present within the data set of these experiments makes this a reasonable

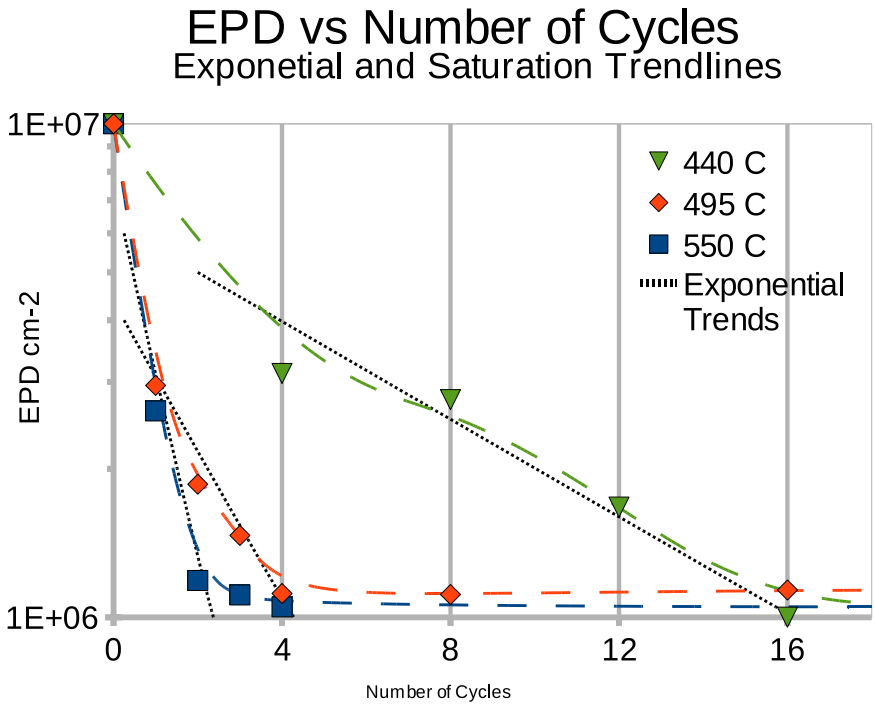

Figure 5.8: Variation of EPD with number of cycles for anneals performed at 440, 494, and 550 °C. The trend lines shown are exponential for areas where reduction is seen and constant for points beyond.

approximation. Therefore, by allowing for $k_1 \propto T$ equation (5.2) can be rewritten as

$$D = D_o e^{-\alpha T t}, \tag{5.4}$$

with all of the proportionality constants being wrapped up into α. Thus, It can be expected that the post annealed EPD has an exponential correlation to temperature when t (the number of cycles) is constant. The data shown in figure 5.7 follows the trend expected from equation (5.4).

Figure 5.8 summarizes the results presented in section 5.3.2. All data points in figure 5.8 represent the average EPD of the $4-5$ different samples in the previous figures. The rate of exponential decay is highly dependent on the annealing temperature. Thus, the higher the temperature, the fewer cycles are needed to reduce the EPD to the saturation limit.

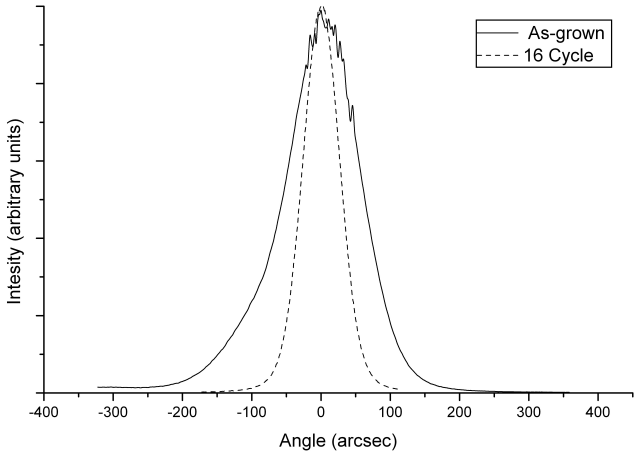

Figure 5.9: Comparison between the rocking curves recorded for an as-grown sample having an EPD of 1×10^7 cm^{-2} (solid line) and a 494 °C, 16 cycle annealed sample having an EPD of 8.9×10^5 cm^{-2} (broken line). The FWHM values for the as-grown and the annealed samples are 120 arcsec and 62 arcsec, respectively.

Equation (5.2) can be used to explain the results shown in figure 5.8. In this situation, the time t (the number of annealing cycles), is varied and the temperature (thus k_1) is held constant for each data set. It is clear that the EPD has an exponential relationship with time and the temperature controls the slope of the exponential decay. It should also be clear that this is an incomplete model as the theory does not predict the saturation regions visible in figure 5.7 and 5.8. In order to predict this aspect of the data a second order reaction equation is needed. The scope of this chapter is restricted to providing a qualitative understanding of the dislocation reduction process. A more extensive model using the second order reaction equation is presented in the next chapter.

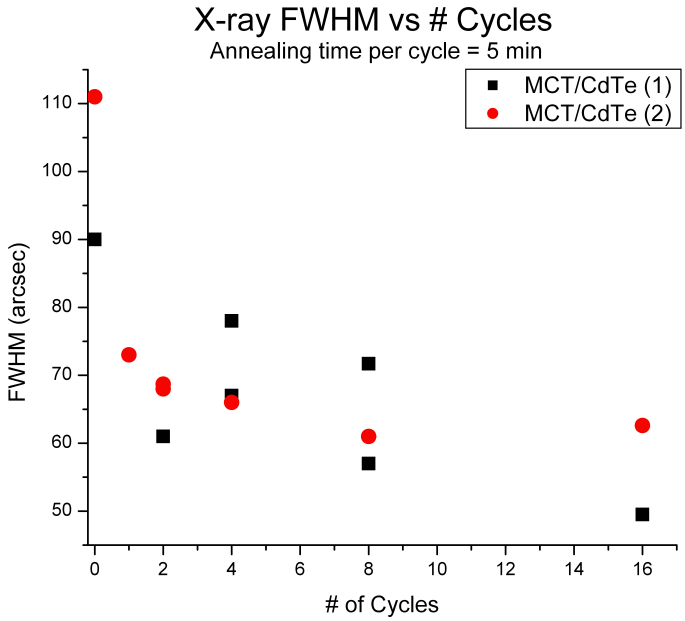

Figure 5.10: Variation of x-ray rocking curve FWHM of the [422] crystal plane with number of annealing cycles for $T = 494$ °C.

5.3.4 X-ray Diffraction Measurements of TCA Effects

Figure 5.9 shows typical x-ray rocking curves recorded for an as-grown and sample annealed for 16 cycles at 494 °C. A clear improvement in the crystalline quality can be seen via the reduction in the FWHM (from 120 to 62 arcsec). This is consistent with other studies that show correlation between x-ray FWHM and defect density[10, 11]. Variation of FWHM with the number of annealing cycles is shown in figure 5.10. The x-ray measurements were performed prior to performing the EPD etch. Figure 5.10 also shows an initial exponential decay in the FWHM of x-ray rocking curves with an increase in the number of annealing cycles, as observed earlier in figure 5.4 for EPD as a function of number of annealing cycles. But, unlike EPD vs number of annealing cycles data in figure 5.4, the x-ray rocking curve FWHM slowly continues to decrease as the number of annealing cycles increase. This might indicate that the overall quality of the crystal will continue to improve with the increase in number of annealing cycles but at a smaller rate than can be discerned using a defect

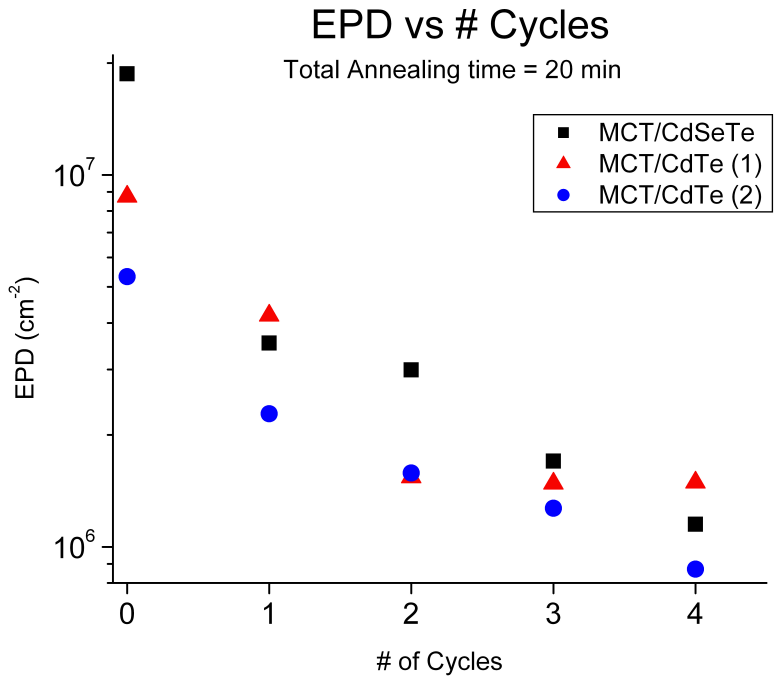

Figure 5.11: Variation of EPD with number of annealing cycles, with the total annealing time kept constant at 20 min for an annealing temperature of 494 °C.

decoration etch. Another explanation for the continued reduction in FWHM is that the subsurface dislocation density of the sample continues to decrease with further annealing cycles. Because the x-rays penetrate deeper than just the surface, the continued reduction in FWHM could be due to a further relaxation of the subsurface half-loop (see section 2.5).

5.3.5 Anneal Duration and Non-Cyclical Annealing

To ensure that the EPD reduction is related to the number of annealing cycles rather than the total duration of the anneal, experiments were conducted where the total annealing time was held constant, but the number of cycles was varied. This was done by performing 1 through 4 cycle anneals while keeping the total annealing time constant at 20 min. Specifically a single cycle annealing was held at 494 °C for 20 min, a 2 cycle anneal for 10 min each cycle, a 3 cycle anneal for 7 min each cycle, and a 4 cycle anneal for 5 min each

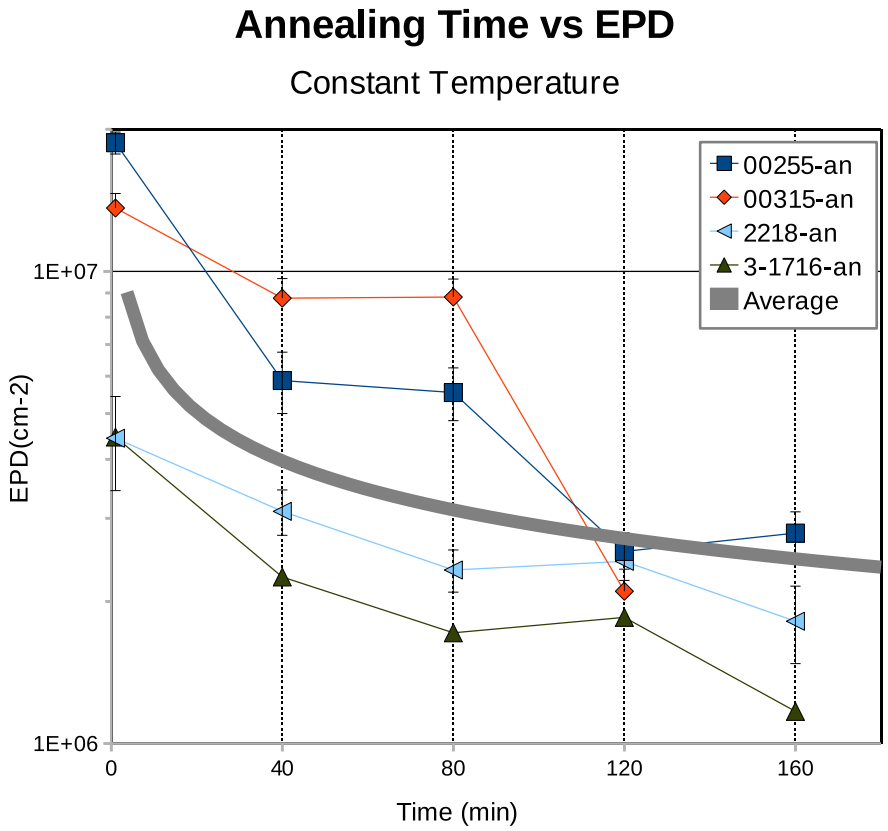

Figure 5.12: Variation in EPD with time for a constant temperature anneal at 494 °C.

cycle. The results of this study can be seen in figure 5.11. By comparing the data presented in Fig. 5.11 and Fig. 5.4, it can be clearly seen that it is not total annealing time that is the primary factor in EPD reduction, but rather the cyclical nature of the annealing. Additional experimentation of 4 cycle anneals with 10 min and 20 min duration for each cycle yielded no advantage over using 5 min cycles.

Dislocation reduction can be observed even for a single annealing cycle, though figure 5.11 suggests that the cyclical nature of annealing is the primary factor that induces dislocation reduction. Non-cyclical anneals were performed in order to investigate any difference in saturation limits and reduction rates that might exist. Figure 5.12 shows the resulting EPD of layers annealed at a constant temperature (494 °C) verses annealing time. The

trend is clearly similar that seen with TCA, though a much longer annealing time ($\sim$ 120 min) is needed to achieve the same reduction. This is in sharp contrast to cyclical annealing were the total time spent at the maximum annealing temperature, 20 min for 4 cycles at the same temperature. Once again, a saturation of the dislocation density is observed at $\sim 1 \times 10^6$ cm^{-2}. This data shows that cyclical annealing is not explicitly necessary for dislocation motion and annihilation/coalescence, but the cyclical annealing does enhance the reduction rate. Thus, it minimizes the total time that the sample is kept at high temperature. This is an important factor when dealing with materials like HgCdTe whose sublimation and diffusion temperatures are low.

The enhancement to the dislocation reduction rate is likely due to the climb related motion that is induced by the change in temperature. It was shown in section 2.3.3 that the chemical force in HgCdTe is very large because the vacancy concentration is strongly dependent on the temperature. Any significant change in temperature will induce a significant amount of climb type motion and, thus, increase the amount and rate of dislocation interaction.

5.4 Etch Pit Density Depth Profiles of TCA Layers

EPD, by it's nature, is only able to provide information about the dislocation density near the surface of the layer. To understand the behavior of the dislocations through out the bulk of the material, etch pit depth profiles were performed on select samples. For this process the Benson etch was used rather than the Schaake etch due to it's slow etch rate. In order to provide the same sized etch pits, the Benson etch removes 0.5 μm, while the Schaake etch removes 2.5 μm of material. Thus, more data points are obtained by using the Benson etch. An additional feature of the Benson etch is that it etches the CdTe layer more aggressively than the HgCdTe layer. The undercutting of the CdTe at the step edge due to this effect provides for more accurate measurements of HgCdTe layer thickness when using depth profilometry.

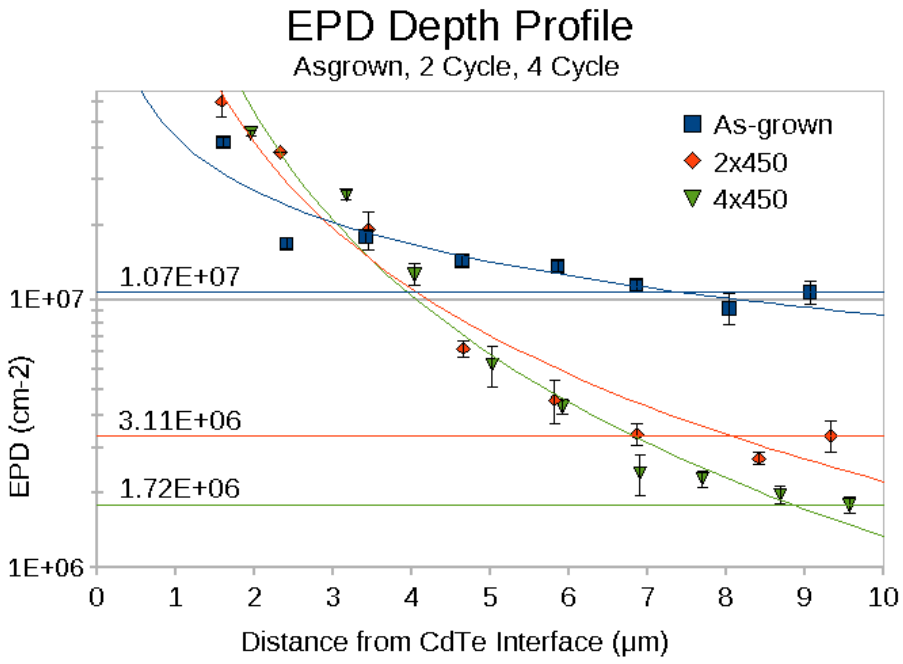

Figure 5.13: EPD depth profile for as-grown, two cycle, and four cycle anneals for an annealing temperature of 494 °C.

The EPD depth profiles data can be seen in figure 5.13. The as-grown layer profile shows that the dislocation density is roughly constant through out the bulk of the HgCdTe layer. Towards the CdTe interface, a marked increase in EPD is seen, which suggests that many more dislocations are formed at the interface that do not thread to the surface. The dislocations in the dense region near the interface have a high probability of interacting and/or annihilating with other dislocations during the growth of the layer.

Etch pit depth profiles for anneals of two and four cycles at 494 °C can be seen to show dislocation reduction through out the majority of the layer. The EPD of the layers converge to the same values as the as-grown layer, near the HgCdTe/CdTe interface. It should be noted that for a dislocation density of $D = 1 \times 10^7$ cm^{-2}, the separation of etch pits, λ, can be estimated via $\lambda = \sqrt{1/D}$. As a result the average separation is about 3 μm. Roughly a 1 μm diameter pit is needed to obtain a clearly visible pit. Thus, it is practically impossible

to accurately measure EPD values of greater than roughly 2×10^7 cm^{-2} via standard optical microscopy.

The reduced EPD near the surface of the layer suggest that the majority of dislocations recede toward the HgCdTe/CdTe interface during annealing. This is in good agreement with the half loop relaxation model as depicted in section 2.5. The population of dislocations at the surface consists of either dislocations that have gone through coalescence and are unable to move, or have not undergone any interaction, neither coalescence nor annihilation. After interaction, the half loop will quickly relax away from the surface due to it's line tension, but slows as it gets caught up in the network of other dislocation loops within the bulk of the material. This effect is observed when comparing the two and four cycle depth profiles in figure 5.13. The EPD profile is quite similar in the middle of the sample (where half loop relaxation has slowed due to half loops interacting with each other), but the area within $3-4$ μm of the surface shows a uniform reduction of $\sim 50\%$ between the two and four cycle anneals.

5.5 Further Analysis

5.5.1 Thickness

The experimental results presented in this chapter so far represent the vast majority of results observed through out this study, though a few outliers do exist. Some samples that have been annealed on multiple occasions that did not show EPD reduction to the 1×10^6 cm^{-2} limit. One such layer repeatedly showed EPD reduction to a $\sim 5 \times 10^6$ cm^{-2} saturation limit, regardless of annealing condition. This is attributed to the thickness of the sample being only 6.0 μm. The thickness of the layer used for depth profiling in figure 5.13 is ~ 10 μm, though it can be clearly seen that at a distance of 6.0 μm from the HgCdTe/CdTe interface the EPD is approximately $\sim 5 \times 10^6$ cm^{-2}. A similar experiment was performed on a layer with a thickness of 3.16 μm which showed only minimal reduction in EPD after annealing.

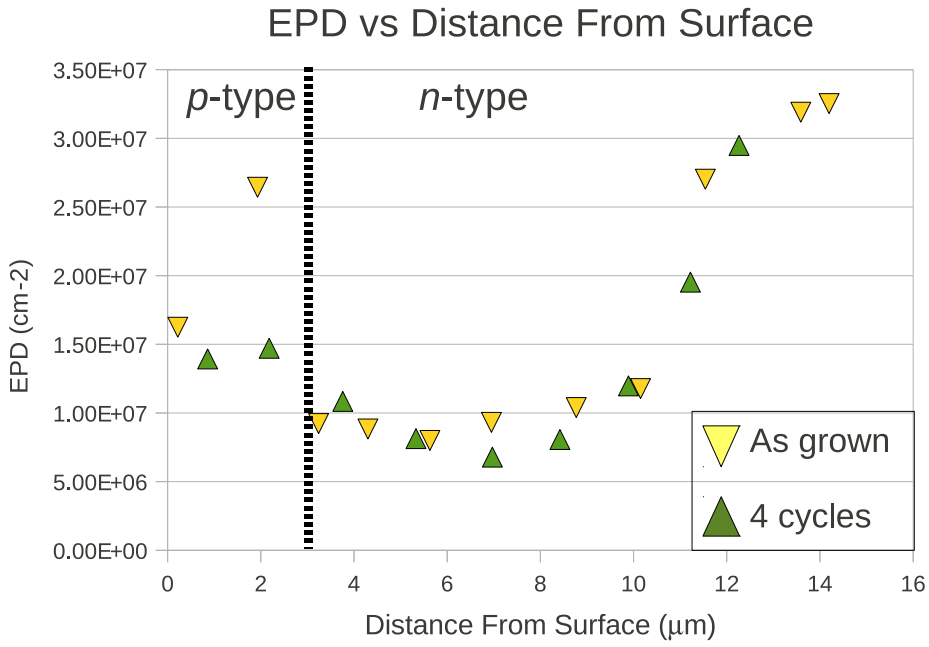

Figure 5.14: EPD depth profile for as-grown and four cycle TCA samples using an annealing temperature of 494 °C. Samples are dual layer HgCdTe/CdTe/Si.

5.5.2 Doping

Dual layer, p on n, samples were subjected to a standard TCA treatment. The p-layer being *in situ* doped with arsenic. Annealing of the layers did not show any significant reduction in EPD. Some layers were etched to remove the p-layer and subjected to TCA. Those samples which had their p layer removed behaved as expected with a reduction of EPD to the standard 1×10^6 cm^{-2} limit. These results show that arsenic doped layer inhibited dislocation motion during annealing. Etch pit depth profiles were performed on two p on n layers for an as-grown and TCA sample. The results can be seen in figure 5.14. The p-type layer is approximately $2-3$ μm thick and it's position can be observed by sudden increase in EPD. Figure 5.14 (b) shows little to no dislocation reduction due to TCA through out the layer. By contrast, samples which had the p-layer etch off showed EPD reduction to $(0.91-2.3) \times 10^6$, i.e. they behaved as expected. It is theorized that by having arsenic incorporated into the lattice, the arsenic atoms serve to block dislocation motion due to the

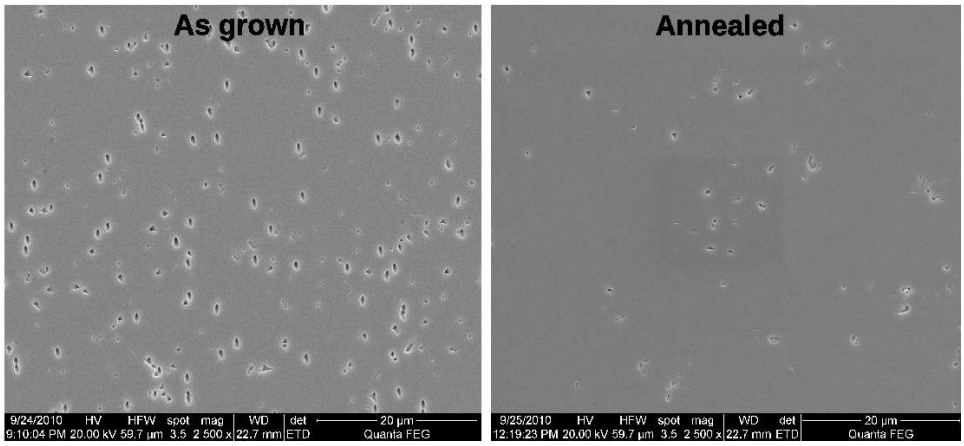

Figure 5.15: SEM micrograph of EPD etched (a) as grown surface, and (b) an annealed surface, with EPDs (as counted by SEM) of 9.3×10^6 and 2.4×10^6 cm^{-2} respectively. Note the absence of fish shaped etch pits in the annealed sample.

Pit Shape	As Grown		Annealed	
	# pits	(cm^{-2})	# pits	(cm^{-2})
Fish Shape	78	2.54×10^6	0	0
Triangular	139	4.52×10^6	40	1.30×10^6
Wedge/Narrow	58	1.89×10^6	23	7.49×10^5
Other	11	3.58×10^5	13	4.23×10^5
Total	286	9.31×10^6	76	2.47×10^6

Table 5.2: Number and densities of the different shaped pits that appear in figures 5.15 (a) and (b).

high activation energy required for the diffusion of arsenic within the crystal[4].

5.5.3 Dislocation Populations After TCA

As shown in section 2.6.4, by using scanning electron microscope (SEM) it is possible to see different classes of etch pits formed by a dislocation decoration etch. It is postulated that the shape of the etch pits can be directly related to the type of dislocation that it formed around[15–17]. This method can be highly effective and useful in developing a method of determining and counting dislocation populations with in HgCdTe layers.

The basic shapes of the etch pits are triangular, wedge shaped, fish shaped and other.

The etch pit populations based off of these 4 shapes were compared before an after annealing for the samples in figure 5.15, the results are presented in table 5.2. It can be seen that the fish shaped etch pits (which account for almost a third of the etch pits) are absence after annealing. This is in interpreted to mean that they are highly mobile and reactive. Thus, after annealing almost all of them have either annihilated or coalesced. The populations of the triangular and wedge shaped pits show a reduction of roughly 70 and 50%, respectively. The population of the pits classified as "other" is increased slightly after annealing, though this is an expected result, as they are generally believed to be the result of several dislocations in close proximity to each other.

5.5.4 TCA of Mesa Etched Samples

As a part of this work, TCA has been performed on samples that have had mesas etched into them. This work was performed to test the notion that the the steep sidewalls will allow fore enhanced dislocation motion due to image forces generated at the side walls (see section 2.3.5). The mesa structures have been created using photolithography to layout a mask of different sized shapes, and an inductively coupled plasma (ICP) reactive ion etch (RIE) to delineate mesas in an HgCdTe layer. The etching process used was able to make side walls that are very close to vertical (~ 80 °). Samples that have been etched have mesa heights that range from just a couple of microns to the full thickness of the layer (9 μm). For these experiments, a mask with many features was used in order to obtain a survey of all relevant data that could be collected. The samples were annealed under standard conditions (4 cycles at 494 °C).

Mesa tops with sizes ranging from $5-100$ μm showed little to no reduction in dislocation density. Some images of TCAed mesas are shown in figure 5.16. The EPD on top of the mesas was measured to be 4×10^6, 4×10^6, 6×10^6 and 6.4×10^6 cm^{-2} for figures 5.16 (a),(b),(c) and (d) respectively. While all of the circular and square mesas had a rather consistent EPD, diamond shaped mesas that were on the sample showed a distinctively different behavior. The diamond shapes differed by their orientation, one with the major

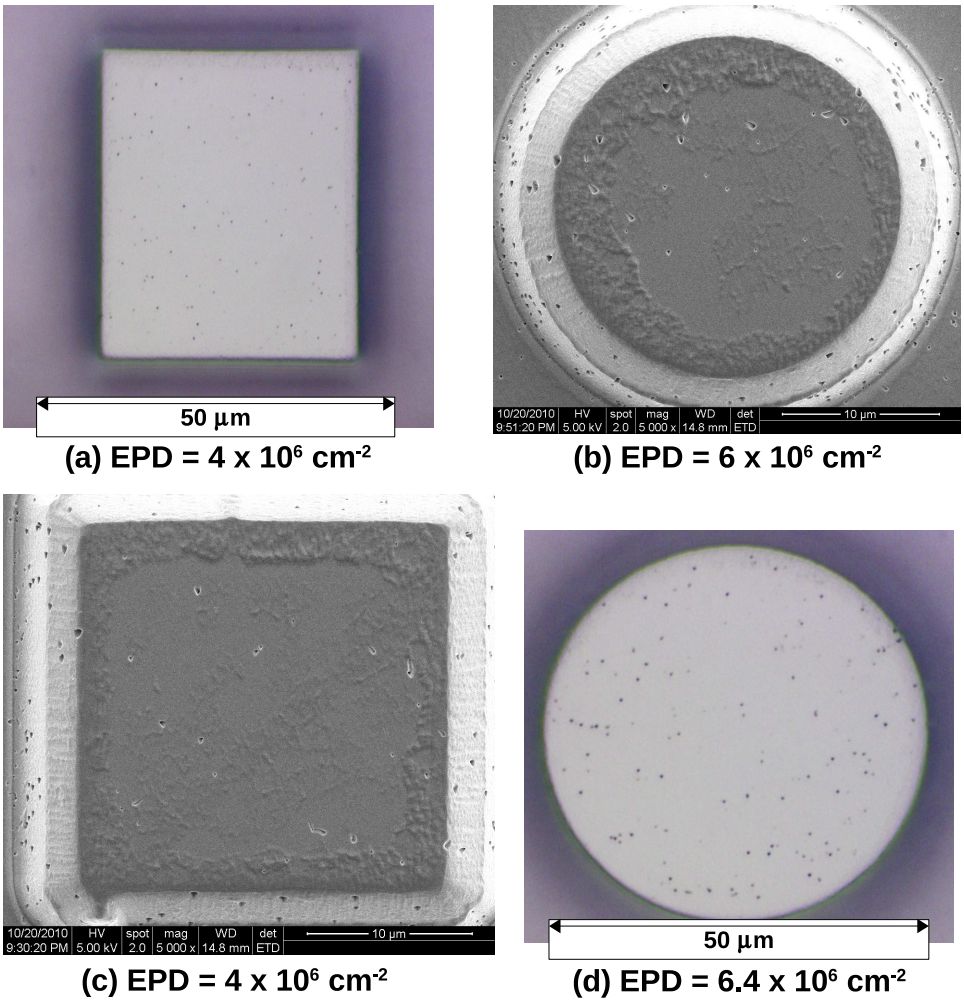

Figure 5.16: Micrographs of mesas after EPD etch of: (a) bright field 50 μm square, (b) SEM 25 μm circle, (c) SEM 25 μm square, (d) bright field 50 μm circle. (4 annealing cycles, $T = 494$ °C)

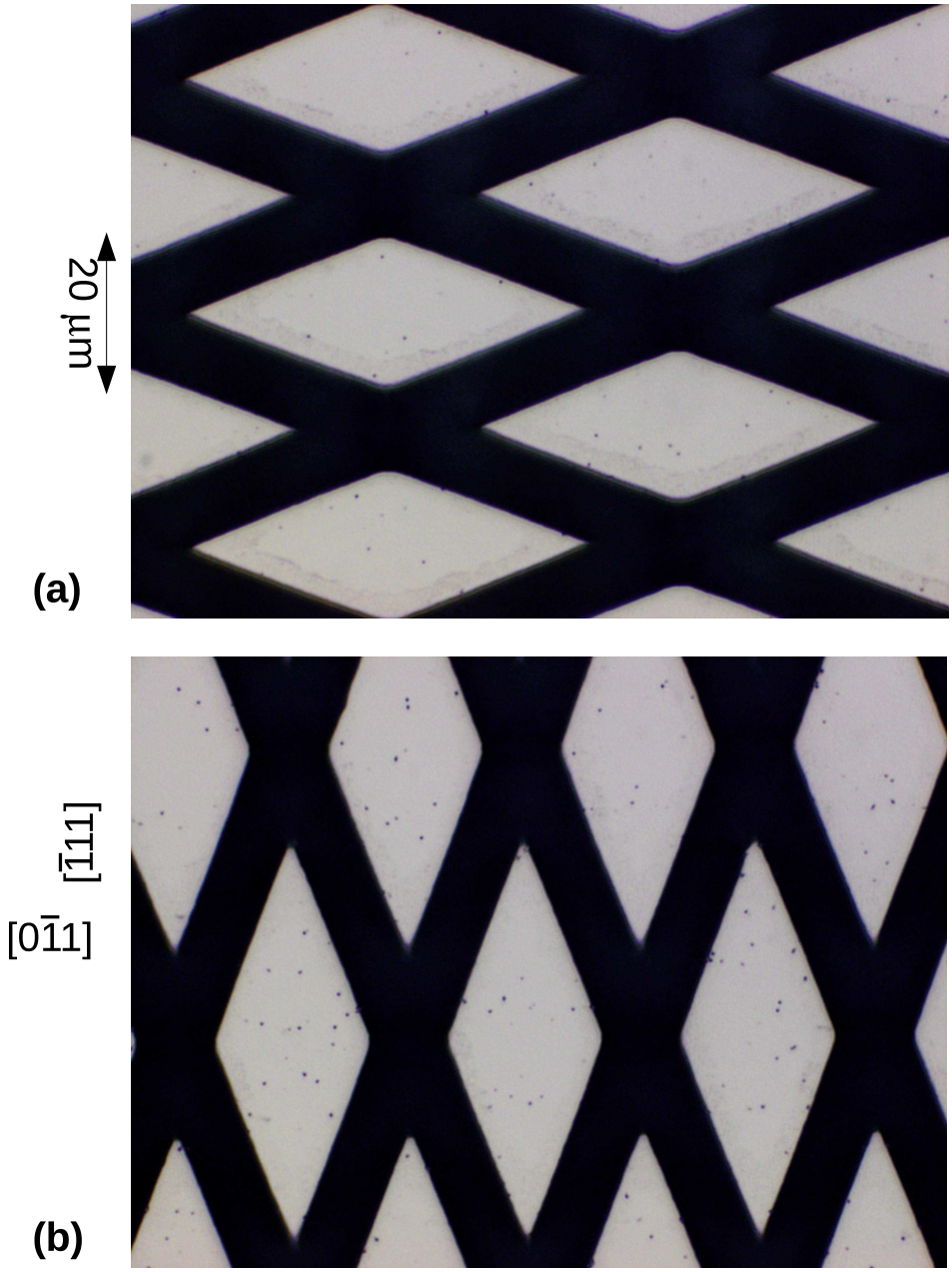

Figure 5.17: Bright field micrographs of diamond shaped mesas with different orientations. Note that the diamonds with a left-right orientation have a much lower EPD than the diamonds with an up-down orientation. (4 annealing cycles, $T = 494$ °C)

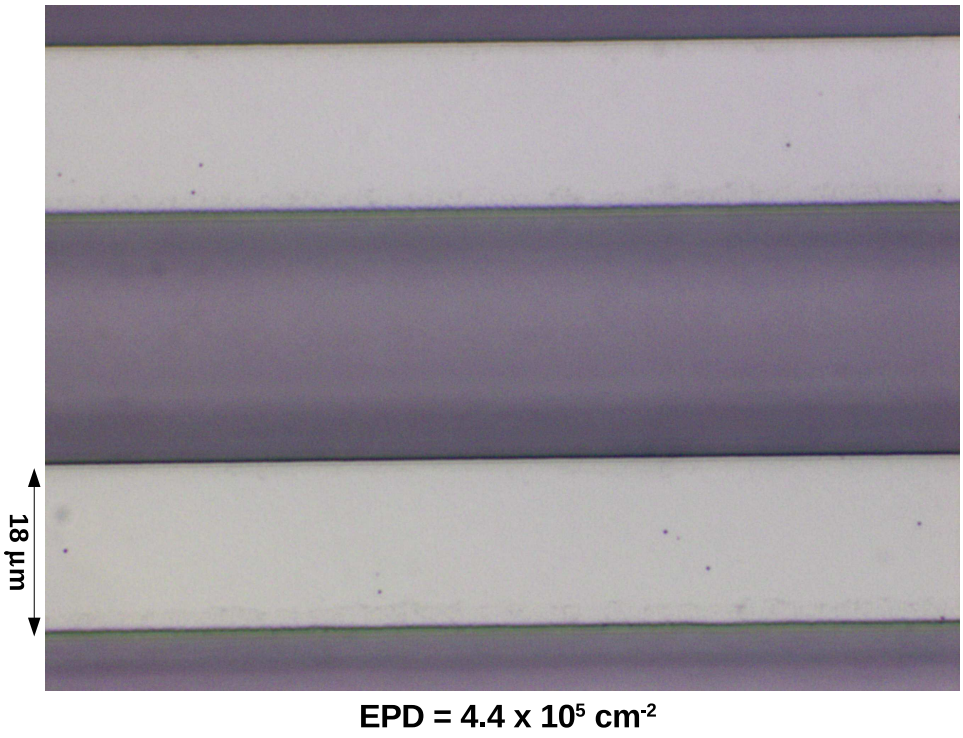

Figure 5.18: Bright field micrograph of two bars 18 μm wide. The areas on top of the bars show a dislocation density of 4.4×10^5 cm^{-2}. (4 annealing cycles, $T = 494$ °C)

axis in the $[0\bar{1}1]$ direction, as shown in figure 5.17 (a), and the other in the $[\bar{1}11]$ direction as shown in figure 5.17 (b). Though both show a dislocation density above the saturation limit, the diamonds in figure 5.17 (a) have a much lower dislocation density.

By far, the most remarkable feature in the samples that showed favorable results was a set of long bars that were included in the mask. The bars are 18 μm wide and several millimeters long. This is long enough to be considered infinite in length. These, unlike the other mesa features, showed a large amount of dislocation reduction. As can be seen in figures 5.18 and 5.19, the EPD in the bars is in the low to mid 10^5 cm^{-2} range. It should be noted that these areas are not of a trivial size. Some bars that had a macro defect present in them still had a large number of dislocations near the defect, but areas far enough away ($10 - 15$ μm) were almost defect free.

The reasons why all of the mesa shapes other than the bars seem to inhibit dislocation

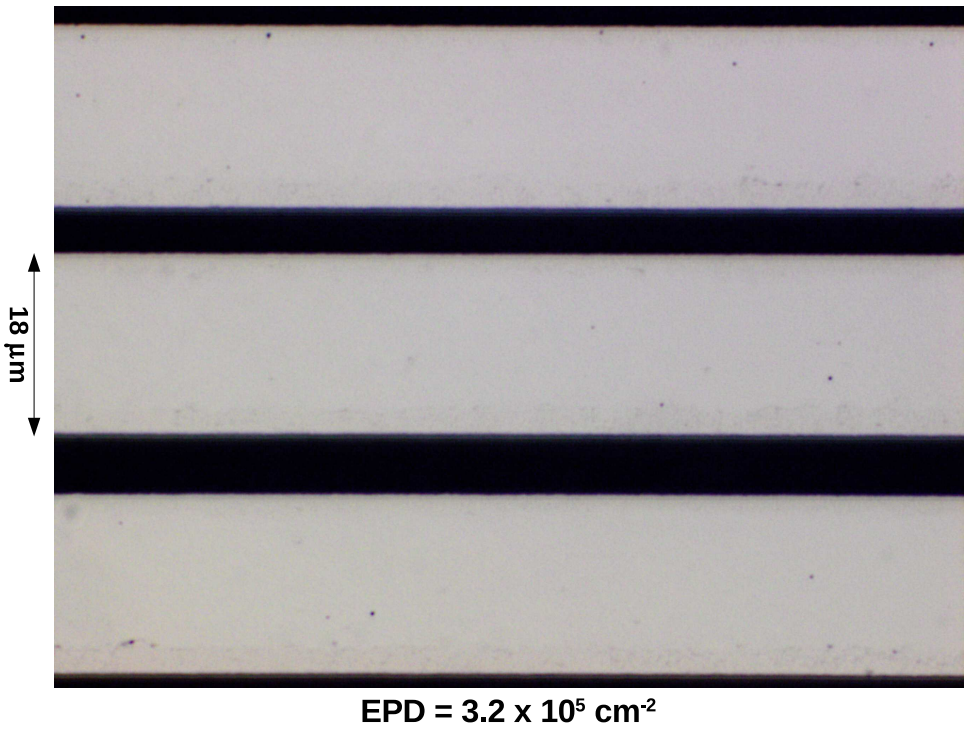

Figure 5.19: Bright field micrograph of three bars 18 μm wide. The areas on top of the bars show a dislocation density of 3.2×10^5 cm^{-2}. (4 annealing cycles, $T = 494$ °C)

motion/reduction is unknown at this time. This is also the case with the long bars which showed the ability to enhance dislocation reduction to a level lower than the saturation limit seen in planar HgCdTe. The current hypothesis is that dislocations that generally move in the $[0\bar{1}1]$ direction (across the length of the bar) interact with side walls in a repulsive manner. While dislocations that move in other directions, like the $[\bar{1}11]$, feel an attractive force are able to "fall off" the edge sidewall.

Picture the situation where there are two families of dislocations present in the material. This is a simplified case where there are two types of misfit dislocations that lead to two types threading dislocations. One of these families, call it $\alpha_{\pm}$, moves in the $\pm[0\bar{1}1]$ direction and the other family, $\beta_{\pm}$, in the $\pm[\bar{1}11]$ direction. The two threading components from the same misfit dislocation will have opposite Burgers vectors (ie, $\alpha_{-} \Rightarrow -b_{\alpha}$, $\alpha_{+} \Rightarrow b_{\alpha}$, and similarly with the β family). Thus, the dislocation reactions $\alpha_{-} + \alpha_{+} = 0$ and $\beta_{-} + \beta_{+} = 0$. For simplicities sake, also assume that $b_{\alpha} + b_{\beta} = b_{sessile}$, where the result is a sessile dislocation. Finally, stipulate that when is near a side wall, α dislocations feel repulsive image force, while β dislocations feel an attractive image force. While this is an over simplification of the actual dislocation dynamics with in HgCdTe, it is a reasonable toy model.

Applying the above model to a standard small circular or square shaped mesa (like those in figure 5.16), it is clear that the α dislocations would be trapped on top of the mesa due to the repulsive image force. Although there is the rather rare case of two dislocations that travel in opposite direction across the length of the mesa to interact with each other in the center. Due to their being trapped on the mesa top, they will quickly become stationary, and therefore their chances of interacting with β dislocations and forming a sessile dislocation increases. By this model the square and circular mesas would have a very high dislocation density of sessile dislocations, and trapped α dislocations.

In the case of the long bars, α dislocations are free move in the $\pm[0\bar{1}1]$ without being stopped by side walls. Because (theoretically) there are infinite dislocations that are capable of moving infinite distance, lots of annihilation in that family will occur. Additionally, the

β dislocations will quickly fall off the side wall and leave little chance for $\alpha \leftrightarrow \beta$ interaction to occur. Clearly in this case the majority of α dislocations would annihilate, β dislocations would leave the mesa, and there would be few occurrences of coalescence.

This experiment is, thus far, the first experiment that has shown enhanced dislocations reduction. That makes it very important because by using long mesa etch bars in combination with TCA it is possible to reduce dislocation densities in HgCdTe grown on Si to a level which is comparable to HgCdTe grown on bulk CdZnTe.

Chapter 6: Modeling of TCA

6.1 The Reaction Equation and TCA Modeling

Dislocation reduction occurs in one of two ways: coalescence or annihilation. When mobile dislocations move to within the annihilation radius of each other, they interact to form another dislocation with a burgers vector equal to their sum. If the sum of the two Burgers vectors is zero, the dislocation is annihilated and forms a sub-surface half loop that relaxes to the interface due to line tension (see section 2.5). In HgCdTe an example of such an annihilation is :

$$\frac{a}{2}[01\bar{1}] + \frac{a}{2}[0\bar{1}1] \rightarrow 0. \tag{6.1}$$

If the sum of the two Burgers vectors is non zero, then they are said to coalesce, and result is that two dislocations transform into a single dislocation. When two 60 ° dislocations coalesce the resulting dislocation can be a sessile edge dislocation. Examples of such dislocation coalescence are the Lomer lock

$$\frac{a}{2}[01\bar{1}] + \frac{a}{2}[101] \rightarrow \frac{a}{2}[110], \tag{6.2}$$

or a Lomer-Cottrell lock

$$\frac{a}{6}[\bar{1}2\bar{1}] + \frac{a}{6}[2\bar{1}1] \rightarrow \frac{a}{6}[110]. \tag{6.3}$$

While not all dislocation reactions with a non zero sum result in a sessile type dislocation, for the purpose of this analysis we shall assume that they do.

In this section, dislocation densities reduction is described using *collision theory*. The TCA process causes the dislocations to move and collide with each other. The frequency

of their collisions is dependent on temperature (as it relates to velocity) and density of the the dislocations, while the chance and type of interaction (reaction) is dictated by the relive Burgers vectors of the two dislocations in question. Collision theory can be used to derive the *rate equation* for simple reactions. Dislocation reactions will be used to describe this phenomena in such a way that it can be modeled using the rate equation.

Dislocation annihilation and coalescence can be described as reaction using the following equations:

$$D_1 \xrightarrow{k_1} 0 \quad \text{(spontaneous annihilation)}, \tag{6.4}$$

$$D_1 + D_1 \xrightarrow{k_2} 0 \quad \text{(annihilation)}, \tag{6.5}$$

$$D_1 + D_1 \xrightarrow{k_2} D_2 \quad \text{(coalescence)}. \tag{6.6}$$

Where D_1 and D_2 are the mobile dislocation density and sessile dislocation density respectively, and k_1 and k_2 are the corresponding rate coefficients. The first equation represents dislocation reduction due to interactions with the edges of the crystal, grain boundaries, or other macro type defects. Equations (6.5) and (6.6) represent the case of two glissile dislocations that interact with each other and either annihilate completely or coalescing into a sessile type dislocation. The reaction equations for these reactions are

$$\frac{\mathrm{d}D_1}{\mathrm{d}t} = -k_1 D_1 - k_2 D_1^2 \tag{6.7}$$

and

$$\frac{\mathrm{d}D_2}{\mathrm{d}t} = \frac{n}{2} k_2 D_1^2, \tag{6.8}$$

Where n is the fraction of dislocations reactions that participate in reaction (6.6) rather than (6.5). The boundary conditions for these equations are $D_1 = D_0$ and $D_2 = 0$ at time $t = 0$, where D_0 is the as-grown dislocation density. The assumption $D_2 \approx 0$ is validated by

the depth profile data presented in section 5.4 where the dislocation density can be seen to be roughly constant through out the layer, thus indicating little to no dislocation interaction throughout the bulk of the layers.

Solving for D_1 and D_2 in equations (6.7) and (6.8) gives

$$D_1 = \left[-\frac{k_2}{k_1} + \left(\frac{1}{D_0} + \frac{k_2}{k_1} \right) e^{k_1 t} \right]^{-1} \tag{6.9}$$

$$D_2 = D_0^2 n \frac{k_2}{k_1} \left[1 - e^{-k_1 t} \right]^2 . \tag{6.10}$$

Performing a first order expansion on the exponents and the exponential terms and noting that $k_1/D_0 \ll k_2$, the equations can be simplified to

$$D_1 = \frac{D_0}{1 + D_0 k_2 t} \tag{6.11}$$

$$D_2 = 2 n D_0^2 k_2 t. \tag{6.12}$$

Another benefit of this approximation is that the rate constant k_1 drops out of equations (6.11) and (6.12), and leaves one less parameter that needs to be fit in this model. A second method of arriving at the same conclusion is to assume that the sample is an infinite plane and is a perfect crystal. Thus, spontaneous annihilation is impossible and $k_1 = 0$ in equation (6.7). The total dislocation density after an annealing cycle is given by

$$D_{tot}(\text{cycle 1}) = D_1(\text{cycle 1}) + D_2(\text{cycle 1}) = \frac{D_0}{1 + D_0 k_2 t} + 2 n D_0^2 k_2 t. \tag{6.13}$$

For the second annealing cycle, the as-grown dislocation density, D_0, would be replaced by the density of mobile dislocation remaining after the first cycle, $D_1(\text{cycle1})$. The total

dislocation density after two cycles is given by

$$D_{tot}(\text{cycle 2}) = D_1(\text{cycle 2}) + D_2(\text{cycle 1}) + D_2(\text{cycle 2}), \tag{6.14}$$

where the total number of immobile dislocations is the sum of those generated in both the first and second cycle. With this in mind, the total dislocation density for N annealing cycles is

$$D_{tot}(\text{cycle N}) = D_1(\text{cycle N}) + D_2(\text{cycle 1}) + D_2(\text{cycle 2}) + \ldots + D_2(\text{cycle N}). \tag{6.15}$$

The result in equation (6.15) shows that after many annealing cycles the density of mobile dislocations can be reduced to an arbitrarily low value. After all mobile dislocations have been removed, a number of sessile dislocations will remain which cannot be annihilated with TCA. This result is consistent with the experimental evidence reported in section 5.3. Further examination of this model will focus on the determination of the constants k_2 and n.

6.1.1 Determination of Rate Equation Constants

The rate constant k_2 in equations (6.11) and (6.12) is known to be proportional to the velocity v of the dislocations in the crystal. It has been shown that the velocity has an exponential dependence on temperature[36], so the rate constant can be written as

$$k_2 = av = ae^{-\frac{E_a}{k_b T}}, \tag{6.16}$$

where a is the proportionality constant, E_a is the activation energy, k_b is Boltzmann's constant and T is temperature in Kelvin. This description of the rate constant is equivalent to the Arrhenius equation commonly used to determine the rate of a chemical reaction. In order to determine the rate constant, k_2, it is necessary to determine both a and E_a.

In the cases where the density of mobile dislocations is much much greater than the

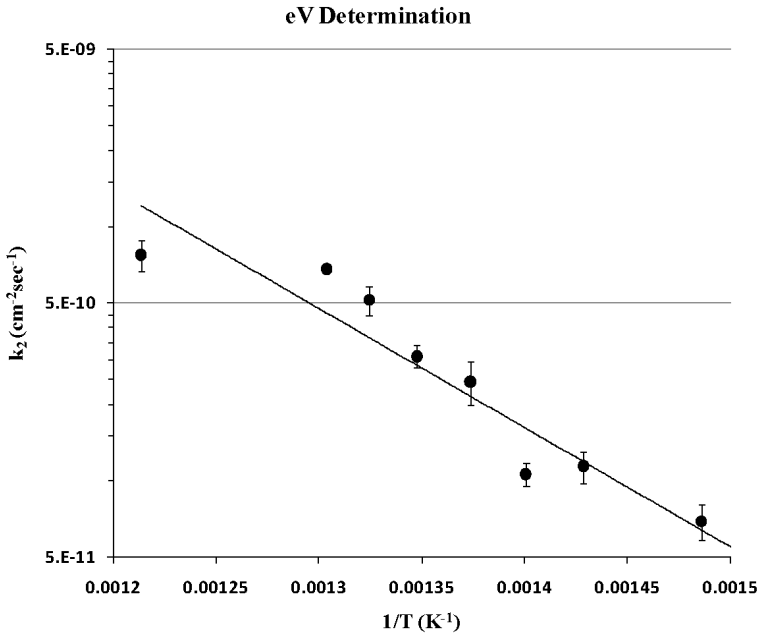

Figure 6.1: Experimental determination of k_2 as a function of T^{-1}.

density of the sessile dislocations, it is clear that equation (6.15) reduces to

$$D_{tot}(\text{cycle N}) \approx D_1(\text{cycle N}).$$

Thus, it is possible to disregard equation (6.12) and simply get

$$D_{tot} \approx D_1 = \frac{D_0}{1 + D_0 k_2 t}. \tag{6.17}$$

This approximation is accurate in the case of TCA performed with low temperature and/or few cycles that result in layers that have dislocation densities much greater than the saturation limit. Rewriting equation (6.17) as

$$\frac{1}{D_0} - \frac{1}{D_1} = k_2 t = k_2 t_a N, \tag{6.18}$$

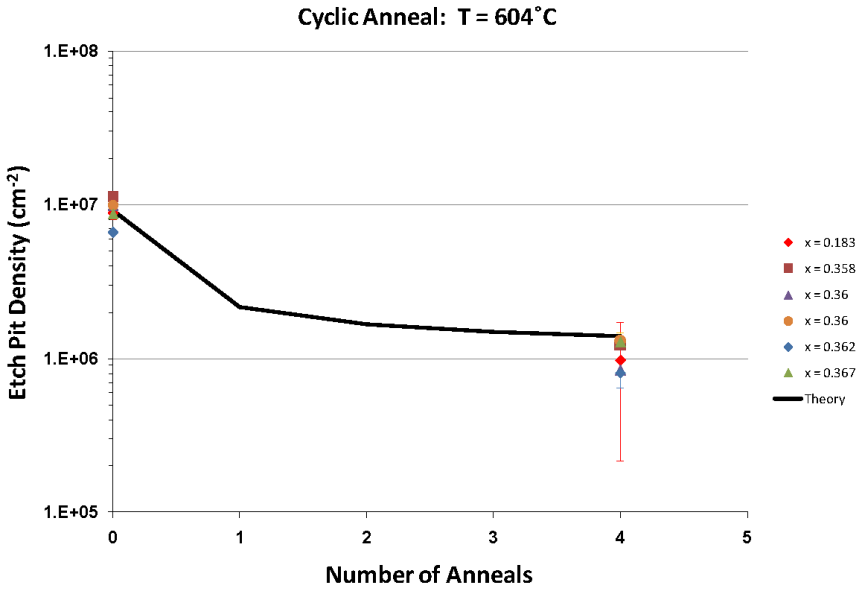

Figure 6.2: Determination of n by empirically fitting experimental data with the TCA at 604 °C at $N = 4$.

where t_a is the time spent at the annealing temperature. The value of k_2 for different annealing temperatures can be determined by plotting $1/D_0 - 1/D_1$ vs $t_a N$. Using the values of k_2 and T, it is possible to determine the activation energy (E_a) and proportionality constant (a) using an Arrhenius plot as shown in figure 6.1. By rewriting equation (6.16) as

$$\ln(k_2) = \ln(a) - \frac{E_a}{k_b}\left(\frac{1}{T}\right), \tag{6.19}$$

it is clear that the slope of figure 6.1 corresponds to E_a/k_b and the projected y-intercept is $\ln(a)$. This results in an activation energy for dislocation motion in HgCdTe/ CdTe/ Si of 0.93 ± 0.1 eV with a proportionality constant of $a = (6 \pm 1) \times 10^{-4}$ cm$^{-2}s^{-1}$. It should be noted that result for the activation energy obtained here is similar to the value reported by Sasaki and Oda[33] for HgCdTe/ GaAs.

The remaining constant n can be determined empirically through a similar fitting. For

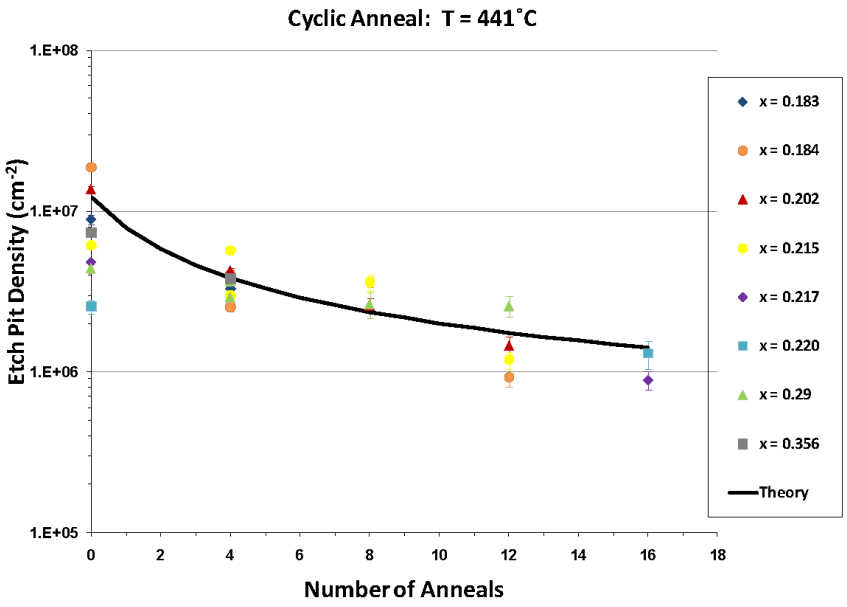

Figure 6.3: Experimental and theoretical results for dislocation density as revealed by EPD for (112)B HgCdTe/CdTe/Si as a function of the number of *ex situ* thermal annealing cycles at 441 °C.

high temperature anneals the total dislocation density can be approximated as

$$D_{tot}(\text{cycle N}) \approx D_{saturation} \approx 2nD_0^2k_2t. \tag{6.20}$$

Thus

$$n \approx \frac{D_{saturation}}{2D_0^2k_2t_aN}, \tag{6.21}$$

with the value of k_2 having been determined previously. Figure 6.2 shows the experimental data for TCA at 604 °C with 4 annealing cycles. The value of n has been determined by empirically fitting for $N = 4$ using equation (6.21) which yields a result of $n = (8\pm2)\times10^{-3}$.

6.1.2 Results and Discussion

Having determined all of the parameters in equations (6.11) and (6.12), it is possible to test the TCA model against the experimental data presented in section 5.3.

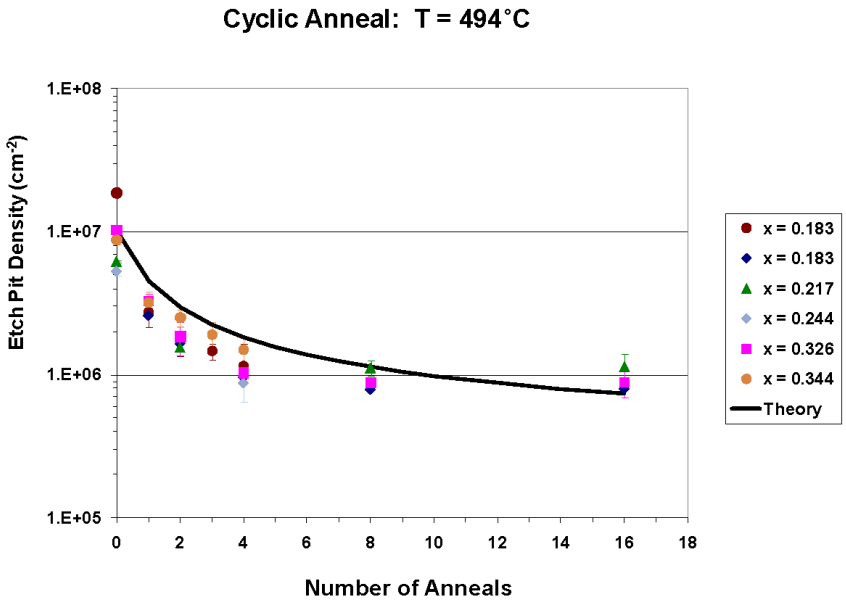

Figure 6.4: Experimental and theoretical results for the dislocation density as a function of the number of *ex situ* thermal annealing cycles at 494 °C.

It can be seen in figure 6.3 that the theoretical results agree well for TCA performed at a low temperature ($T = 441$). The theory predicts that an EPD of $\sim 1 \times 10^6$ cm^{-2} is reached after 16 cycles. The theory also predicts that if a sample was put through 32 annealing cycles, it would see a further reduction of only 0.3×10^6 cm-2. Figures 6.4 and 6.5 also show a strong correlation between the theoretical and experimental results at 494 and 551 °C. The models predict that the EPD will reach $\sim 1 \times 10^6$ cm^{-2} after 4 and 2 cycles, respectively.

Figure 6.6 shows the theoretical and experimental results for 4 annealing cycles at various temperatures. For this particular fit starting EPD of $D_0 = 1.1 \times 10^7$ cm^{-2} is used, this corresponds to a standard as-grown EPD for HgCdTe/Si. The model predicts a minimal reduction of dislocations for temperatures below 375 °C as can be seen in figure 6.6. Above a temperature of ~ 500 °C, the dislocation density is saturated and further reduction is not possible with an increase in the annealing temperature. The slight curve upwards towards the high temperature regime is attributed to the effect of the time step t_a that represents

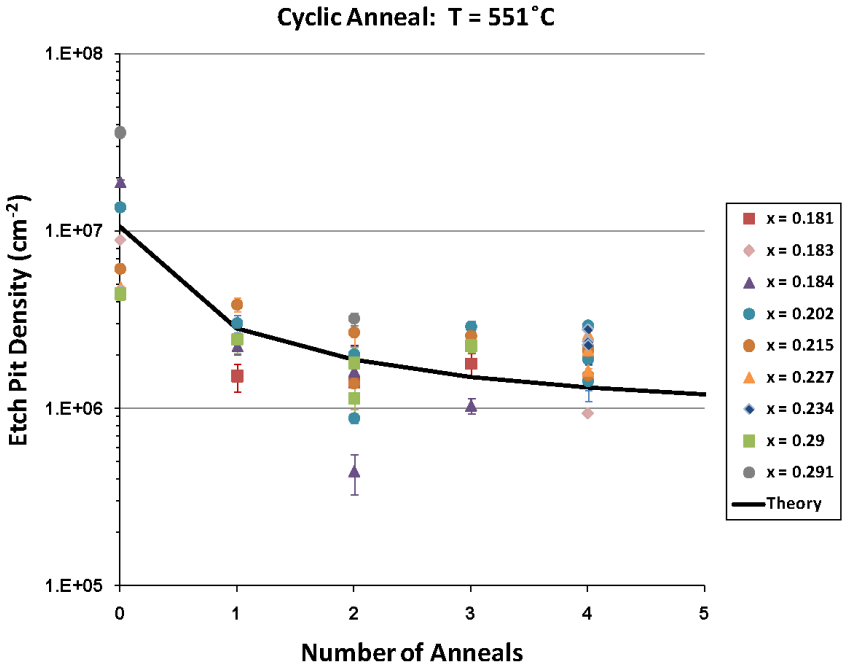

Figure 6.5: Experimental and theoretical results for the dislocation density as a function of the number of *ex situ* thermal annealing cycles at 551 °C.

each annealing cycle. As the number of cycles needed to approach the saturation limit gets close to or less than 1 cycle, the model breaks down because a smaller time step is needed to maintain stability.

This model can also be used to predict the number of cycles needed for lower temperatures. Based on the results, it is believed that $\sim$ 64 annealing cycles would be needed to reach the saturation limit at 400 °C. At this time there has been no verification of this prediction.

In chapter 5.5, it was shown that samples that were *in situ* doped with arsenic did not show dislocation reduction like undoped and indium doped sample. This is currently attributed to the As atoms in the crystal that block dislocation motion. The activation energy for diffusion of As in HgCdTe is 1.28 eV as opposed to indium which has an activation energy of $0.55 - 0.95$eV[4]. In As doped layers, the As atoms need to be mobile prior to the dislocations being able to move. Thus, the minimum activation energy for dislocation

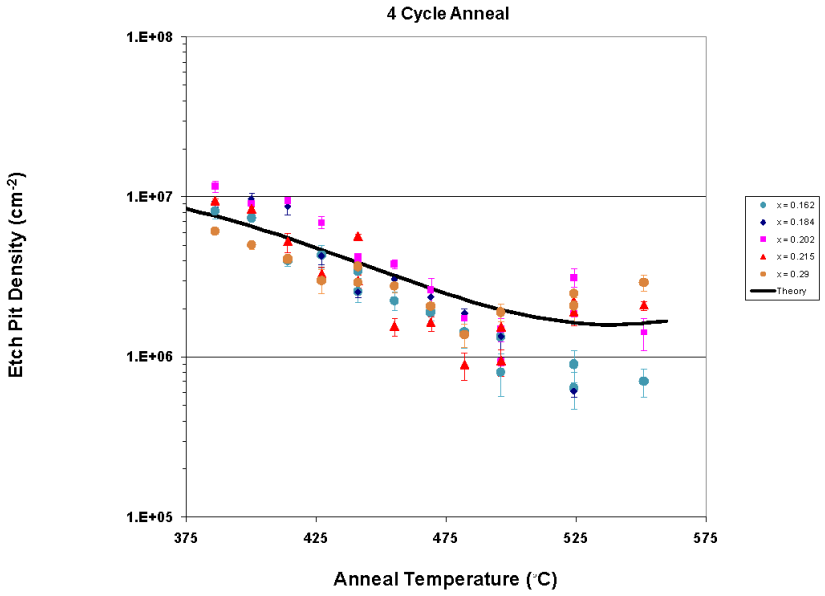

Figure 6.6: Experimental and theoretical results for the dislocation density as a function of temperature for 4 *ex situ* thermal annealing cycles.

motion should be equal to the As activation energy. Using $E_a = 1.28$eV instead of using 0.93 eV, the curve in figure 6.6 is shifted by nearly 200 °C. Thus, it is predicted that using a $\sim$ 700 °C anneal, saturation could be obtained after 4 cycles, unfortunately, the maximum temperature that HgCdTe can sustain is around 650 °C.

6.1.3 Further Refinements and Future Work

The model presented in this chapter has shown that it is capable of predicting both dislocation reduction and saturation to a high degree of accuracy. Greater accuracy could be obtained by including a temperature dependence on the proportionality constant a, which would transform equation 6.16 from an Arrhenius type to what is commonly called the modified Arrhenius equation

$$k_2 = a\left(\frac{T}{T_o}\right)^n e^{-E_a/k_bT}, \tag{6.22}$$

where T_0 is a reference temperature, and n is a constant exponent. The addition of this factor could be used to perfect the fit of the model to the data, though without more precise data this addition is not necessary.

TEM observations of HgCdTe/CdTe report an estimated dislocation density of 3×10^8 cm^{-2} at the HgCdTe/CdTe interface[37], while the EPD depth profile of an as-grown sample in section 5.4 show a rather constant dislocation density of 1×10^7 cm^{-2}. So there is a legitimate reason to question the assumption $D_2(t = 0) = 0$, as an order of magnitude reduction in dislocation density has already occurred within the as-grown layer. The as-grown EPD of HgCdTe samples can also vary between $5 - 10 \times 10^6$ cm^{-2} thus adding up to a half order of magnitude of dislocations that have already interacted and annihilated during growth. This aspect of the theory was (for good reason) not addressed in this work due to inability of differentiating the sessile and mobile dislocation densities. All theoretical results presented here are based off of an initial dislocation density of $D_0 = 1.1 \times 10^7$ cm^{-2}. In order to properly take into account the initial density of sessile dislocations, the density would need to be counted via some other means such as TEM or an SEM analysis of etch pit shapes (see section 2.6.4).

While the above refinements to this theory of cycle annealing would provide for more accurate results and further refinement of the constants used in the theory, there is also a fundamental problem with the theory itself. The time step used for the computational model is $t_a N$ and is used to draw a parallel between the time and number of cycles. But the theory does not explicitly state that the annealing is cyclical. It was shown in section 5.3.5 dislocation reduction can be achieved with an extended single cycle of annealing but annealing time must be greatly increased (almost an order of magnitude) in order to obtain the same effect. A true model of TCA must take this fact in to account. Unfortunately this is beyond the scope of this work, as an understanding of the exact mechanisms behind dislocation motion are still uncertain.

Further research into how the dislocations move and why TCA enhances that motion

over constant temperature annealing is needed. It is clear that both types of dislocation motion, glide and climb, need to be accounted for separately in order to produce a more accurate model, this is in addition to using a more detailed account of the dislocation populations and the reactions between them.

Chapter 7: Conclusion

The experiments in this work show that the dislocation density in HgCdTe and CdTe can be reliably reduced via thermal cycle annealing. In the case of CdTe, it is possible to perform cyclical annealing *in situ* and obtain dislocation densities in the mid 10^5 cm^{-2} range. Because it can be done during growth, this technique is a scalable process that can be used to make high quality composite substrates of any size. The knowledge gained through this study of *in situ* TCA of CdTe has greatly furthered the development and optimization of CdTe/Si composite substrates.

Experimental results of *ex situ* TCA of HgCdTe show that dislocation density can be reduced to $(1.5 \pm 0.5) \times 10^6$ cm^{-2} in a reproducible manner with no inexplicable outliers. The effects of TCA on HgCdTe/CdTe/Si layers has been studied in much greater detail than the effects of TCA on CdTe/Si. The study was performed not only to observe and measure the lower limit on dislocation density that could be achieved but additionally all control-able parameters involved in TCA were studied in detail. As a result, it has been shown that dislocation density varies exponentially with both annealing temperature and number of annealing cycles. Several other parameters, such as the as-grown EPD, the substrate EPD, the cadmium composition, etc, did not play a significant role in dislocation reduction. Thus it has been shown that any undoped or indium doped HgCdTe epilayer can be annealed to obtain a low dislocation density. In addition, ICP etched bar mesas have shown that the saturation limit observed in planar HgCdTe can be overcome. By using these structures it is believed to be possible to develop HgCdTe layers that have dislocation density comparable to those grown on CdZnTe.

TCA of both CdTe and HgCdTe have provided strong evidence to support the half-loop relaxation model. Particularly strong evidence was provided by the EPD depth profiles of

CdTe and HgCdTe samples. In both cases the EPD increases exponentially in the region near the interface. In the half loop relaxation model, the EPD increase corresponds to a web of half-loops that have piled up during annihilation/coalescence. Near the surface of the layer, there is a roughly constant EPD in the top several microns.

The model based on of the second order reaction equations, has been shown to fit and predict dislocation density reduction and the saturation limit with a high degree of accuracy. By using the wealth of data generated experimentally, all free parameters in the model were fitted and only have a small error. One of the more important of these parameters is the activation energy for dislocation motion that was determined to be 0.93 eV. This is very close to the Hg vacancy activation energy, and gives good insight into the mechanisms behind dislocation motion. [3]

Chapter 8: Future Work

In the opinion of the author further work is needed in several areas. A brief outline of some such projects is provided here:

In an effort to find novel ways to enhance dislocation motion and reduction, a more detailed computational model of dislocation reduction than that present in this work needs to be developed. This model needs to account for more than just dislocation density, temperature, and time, but also include change in temperature and various microscopic quantities such as dislocation populations based on Burgers vector, and line vector. Dislocation motion will need to be described using both glide and climb type motion and the effects of point defects within the material must be considered.

The work presented in section 2.6.4 needs to be extended in order to further assess the dislocation populations that exist within the crystal. More TEM investigations are needed to determine precisely what dislocation line vectors and associated Burgers vectors are present within the crystal. Unfortunately, TEM is limited by it's ability to examine only a very small region of the crystal. To gain a good idea of what the populations of dislocations are within the crystal, the most likely source is use the different shapes of the etch pits present in the material when examined with SEM (see section 2.6.4).

The characterization of the shape of etch pits and their associated dislocation is currently an ongoing project. It was shown by TEM in section 2.6.4 that the "fish shaped" etch pits can be clearly linked to a single dislocation type. At this time several other etch pits have been linked to different types of dislocations, though the correlation is not as solid as with the fish shaped pits. Additionally, modeling of the effects of EPD etches can be performed in order to determine the link between dislocations and their etch pits. Though the modeling of dislocations would help with the determination of etch pit-dislocation correlation, TEM

surveys of dislocations is still necessary to develop and confirm a picture of what dislocations actually exist within the crystal.

The work done on using TCA on ICP etched bars in HgCdTe layers has shown that dislocation reduction to the level of HgCdTe/CdZnTe is possible. There are several aspects to the function of these mesas that are unknown. The effects of several parameters must be established to understand why and how lower saturation can be achieved. Namely, how does the width correspond to the saturation limit, how far from the edge of the bars can a low dislocation density be achieved and how deep and wide do the trenches between bars need to be. These are just a few of the testable parameters that should be examined.

As of this point and as a direct result of this work, the effect of thermal cycle annealing has been established. On planar HgCdTe dislocation density can be reduced to 1×10^{6} cm^{-2}, but this requires annealing for 4 cycles at 494 °C, 16 cycles at 441 °C or some other combination. For single layer devices this is a perfectly feasible option. But one of the goals for third generation IRFPAs is to also include dual color (combination MWIR and LWIR) detector arrays. For applications such as these, the amount of diffusion that occurs during the TCA process is unacceptable. Thus one of the main goals for the coming research in thermal cycle annealing is to determine new and novel methods of enhancing dislocation motion so that dislocation reduction can be achieved at lower temperatures and with less annealing time.

Bibliography

Bibliography

[1] S. M. Johnson, D. R. Rhiger, J. P. Rosbeck, J. M. Peterson, S. M. Taylor, and M. E. Boyd, "Effect of dislocations on the electrical and optical properties of long-wavelength infrared hgcdte photovoltaic detectors," *J. Vac. Sci. Technol. B*, vol. 10, no. 4, pp. 1499–1506, 1992. [Online]. Available: http://link.aip.org/link/?JVB/10/1499/1

[2] Y. Chen, "Molecular beam epitaxy growth of high quality cadmium telluride on silicon," Ph.D. dissertation, University of Illinois at Chicago, Chicago, Illinois, 1995.

[3] D. Shaw and P. Capper, "Conductivity type conversion in $hg_{1-x}cd_xte$," *Journal of Materials Science: Materials in Electronics*, vol. 11, pp. 169–177, 2000, 10.1023/A:1008989701564. [Online]. Available: http://dx.doi.org/10.1023/A:1008989701564

[4] P. Capper and J. Garland, *Mercury Cadmium Telluride: Growth, Properties, and Applications*. The Atrium, Southern Gate, Chichester, West Sussex, PO19 8SQ, United Kingdom: John Wiley & Sons Ltd, 2010.

[5] H. R. Vydyanath and C. H. Hiner, "Annealing behavior of undoped $hg_{0.8}cd_{0.2}te$ epitaxial films at low temperatures," *Journal of Applied Physics*, vol. 65, no. 8, pp. 3080–3088, 1989. [Online]. Available: http://link.aip.org/link/?JAP/65/3080/1

[6] A. Sher, M. A. Berding, M. van Schilfgaarde, and A.-B. Chen, "Hgcdte status review with emphasis on correlations, native defects and diffusion," *Semiconductor Science and Technology*, vol. 6, no. 12C, p. C59, 1991. [Online]. Available: http://stacks.iop.org/0268-1242/6/i=12C/a=012

[7] J. Weertman and J. R. Weertman, *Elementary Dislocation Theory*. Oxford University Press, 1992.

[8] D. Hull and D. J. Bacon, *Introduction to Dislocations*, 3rd ed. Pergamon Press, 1984.

[9] A. E. Romanov, W. Pompe, S. Mathis, G. E. Beltz, and J. S. Speck, "Threading dislocation reduction in strained layers," *Journal of Applied Physics*, vol. 85, no. 1, pp. 182–192, 1999. [Online]. Available: http://link.aip.org/link/?JAP/85/182/1

[10] J. E. Ayers, "The measurement of threading dislocation densities in semiconductor crystals by x-ray diffraction," *Journal of Crystal Growth*, vol. 135, no. 1-2, pp. 71 – 77, 1994. [Online]. Available: http://www.sciencedirect.com/science/article/B6TJ6-46FJ3WG-89/2/804b83a03058b06600682a58aa9cd190

[11] J. Benson, R. Jacobs, J. Markunas, M. Jaime-Vasquez, P. Smith, L. Almeida, M. Martinka, M. Vilela, and U. Lee, "Structural analysis of cdte hetero-epitaxy on (211) si," *Journal of Electronic Materials*, vol. 37, pp. 1231–1236, 2008, 10.1007/s11664-008-0469-5. [Online]. Available: http://dx.doi.org/10.1007/s11664-008-0469-5

[12] W. Everson, C. Ard, J. Sepich, B. Dean, G. Neugebauer, and H. Schaake, "Etch pit characterization of cdte and cdznte substrates for use in mercury cadmium telluride epitaxy," *Journal of Electronic Materials*, vol. 24, pp. 505–510, 1995, 10.1007/BF02657954. [Online]. Available: http://dx.doi.org/10.1007/BF02657954

[13] J. Benson, P. Smith, R. Jacobs, J. Markunas, M. Jaime-Vasquez, L. Almeida, A. Stoltz, L. Bubulac, M. Groenert, P. Wijewarnasuriya, G. Brill, Y. Chen, and U. Lee, "Topography and dislocations in (112)b hgcdte/cdte/si," *Journal of Electronic Materials*, vol. 38, pp. 1771–1775, 2009, 10.1007/s11664-009-0758-7. [Online]. Available: http://dx.doi.org/10.1007/s11664-009-0758-7

[14] J. Benson, L. Bubulac, P. Smith, R. Jacobs, J. Markunas, M. Jaime-Vasquez, L. Almeida, A. Stoltz, P. Wijewarnasuriya, G. Brill, Y. Chen, U. Lee, M. Vilela, J. Peterson, S. Johnson, D. Lofgreen, D. Rhiger, E. Patten, and P. Goetz, "Characterization of dislocations in (112)b hgcdte/cdte/si," *Journal of Electronic Materials*, vol. 39, pp. 1080–1086, 2010, 10.1007/s11664-010-1262-9. [Online]. Available: http://dx.doi.org/10.1007/s11664-010-1262-9

[15] J. Yang, X. Cao, Y. Wei, and L. He, "Traces of hgcdte defects as revealed by etch pits," *Journal of Electronic Materials*, vol. 37, pp. 1241–1246, 2008, 10.1007/s11664-008-0465-9. [Online]. Available: http://dx.doi.org/10.1007/s11664-008-0465-9

[16] Y.-C. Lu, R. K. Route, D. Elwell, and R. S. Feigelson, "Etch pit studies in cdte crystals," *Journal of Vacuum Science & Technology A: Vacuum, Surfaces, and Films*, vol. 3, no. 1, pp. 264–270, 1985. [Online]. Available: http://link.aip.org/link/?JVA/3/264/1

[17] Y. Jianrong, G. Huiming, C. Xinqiang, F. Weizheng, and H. Li, "Dislocation assessment of cdznte by chemical etching on both 111b and 211b faces," *Journal of Crystal Growth*, vol. 234, no. 2-3, pp. 337 – 342, 2002. [Online]. Available: http://www.sciencedirect.com/science/article/B6TJ6-442Y6HM-K/2/80b1853e0d8272ccc858bcd1d30f3b75

[18] R. Sporken, S. Sivananthan, K. K. Mahavadi, G. Monfroy, M. Boukerche, and J. P. Faurie, "Molecular beam epitaxial growth of cdte and hgcdte on si (100)," *Applied Physics Letters*, vol. 55, no. 18, pp. 1879–1881, 1989. [Online]. Available: http://link.aip.org/link/?APL/55/1879/1

[19] Y. Chen, G. Brill, and N. Dhar, "Mbe growth of cdsete/si composite substrate for long-wavelength ir hgcdte applications," *Journal of Crystal Growth*, vol. 252, no. 1-3, pp. 270 – 274, 2003. [Online]. Available: http://www.sciencedirect.com/science/article/B6TJ6-48068J8-4/2/fc156136451af7cd4d7bb7d236443676

[20] Y. Chen, S. Sivananthan, and J. Faurie, "Structure of cdte(111)b grown by mbe on misoriented si(001)," *Journal of Electronic Materials*, vol. 22, pp. 951–957, 1993, 10.1007/BF02817509. [Online]. Available: http://dx.doi.org/10.1007/BF02817509

[21] P. Wijewarnsuriya, M. Zandian, D. Edwall, W. McLevige, C. Chen, J. Pasko, G. Hildebrandt, A. Chen, J. Arias, A. DSouza, S. Rujirawat, and S. Sivananthan, "Mbe p-on-n hgcdte heterostructure detectors on silicon substrates," *Journal of Electronic Materials*, vol. 27, pp. 546–549, 1998, 10.1007/s11664-998-0013-7. [Online]. Available: http://dx.doi.org/10.1007/s11664-998-0013-7

[22] N. K. Dhar, C. E. C. Wood, A. Gray, H. Y. Wei, L. Salamanca-Riba, and J. H. Dinan, "Heteroepitaxy of cdte on 211 si using crystallized amorphous znte templates," *J. Vac. Sci. Technol. B*, vol. 14, no. 3, pp. 2366–2370, 1996. [Online]. Available: http://link.aip.org/link/?JVB/14/2366/1

[23] T. J. de Lyon, S. M. Johnson, C. A. Cockrum, O. K. Wu, W. J. Hamilton, and G. S. Kamath, "Cdznte on si(001) and si(112): Direct mbe growth for large-area hgcdte infrared focal-plane array applications," *Journal of The Electrochemical Society*, vol. 141, no. 10, pp. 2888–2893, 1994. [Online]. Available: http://link.aip.org/link/?JES/141/2888/1

[24] N. K. Dhar, M. Zandian, J. G. Pasko, J. M. Arias, and J. H. Dinan, "Planar p-on-n hgcdte heterostructure infrared photodiodes on si substrates by molecular beam epitaxy," *Applied Physics Letters*, vol. 70, no. 13, pp. 1730–1732, 1997. [Online]. Available: http://link.aip.org/link/?APL/70/1730/1

[25] J. Varesi, A. Buell, J. Peterson, R. Bornfreund, M. Vilela, W. Radford, and S. Johnson, "Performance of molecular-beam epitaxy-grown midwave infrared hgcdte detectors on four-inch si substrates and the impact of defects," *Journal of Electronic Materials*, vol. 32, pp. 661–666, 2003, 10.1007/s11664-003-0049-7. [Online]. Available: http://dx.doi.org/10.1007/s11664-003-0049-7

[26] Y. Chen, S. Farrell, G. Brill, P. Wijewarnasuriya, and N. Dhar, "Dislocation reduction in cdte/si by molecular beam epitaxy through in-situ annealing," *Journal of Crystal Growth*, vol. 310, no. 24, pp. 5303 – 5307, 2008. [Online]. Available: http://www.sciencedirect.com/science/article/B6TJ6-4TGHNKD-3/2/fea5b126d72c1876746540481078c997

[27] S. Rujirawat, "The cdte/si(111):as interface," Ph.D. dissertation, University of Illinois at Chicago, Chicago, Illinois, 2000.

[28] Z. C. Feng, M. G. Burke, and W. J. Choyke, "Structural defect related donor-bound exciton spectra in cdte epitaxial films," *Applied Physics Letters*, vol. 53, no. 2, pp. 128–130, 1988. [Online]. Available: http://link.aip.org/link/?APL/53/128/1

[29] N. C. Giles-Taylor, R. N. Bicknell, D. K. Blanks, T. H. Myers, and J. F. Schetzina, "Photoluminescence of cdte: A comparison of bulk and epitaxial material," *Journal of Vacuum Science & Technology A: Vacuum, Surfaces, and Films*, vol. 3, no. 1, pp. 76–82, 1985. [Online]. Available: http://link.aip.org/link/?JVA/3/76/1

[30] G. Badano, I. Robin, B. Amstatt, F. Gemain, and X. Baudry, "Reduction of the dislocation density in molecular beam epitaxial cdte(211)b on ge(211),"

Journal of Crystal Growth, vol. 312, no. 10, pp. 1721 – 1725, 2010. [Online]. Available: http://www.sciencedirect.com/science/article/B6TJ6-4YC2XP3-B/2/0aae106437aecac5230a09d6c664a6fc

[31] L. He, S. L. Wang, J. R. Yang, M. F. Yu, Y. Wu, X. Q. Chen, W. Z. Fang, Y. M. Qiao, Y. Gui, and J. Chu, "Molecular beam epitaxy (mbe) in situ high-temperature annealing of hgcdte," *Journal of Crystal Growth*, vol. 201-202, pp. 524 – 529, 1999. [Online]. Available: http://www.sciencedirect.com/science/article/B6TJ6-3Y9GVV8-40/2/7c7409ec670a643eab6969c296742573

[32] S. H. Shin, J. M. Arias, D. D. Edwall, M. Zandian, J. G. Pasko, and R. E. DeWames, "Dislocation reduction in hgcdte on gaas and si," *J. Vac. Sci. Technol. B*, vol. 10, no. 4, pp. 1492–1498, 1992. [Online]. Available: http://link.aip.org/link/?JVB/10/1492/1

[33] T. Sasaki and N. Oda, "Dislocation reduction in hgcdte on gaas by thermal annealing," *Journal of Applied Physics*, vol. 78, no. 5, pp. 3121–3124, 1995. [Online]. Available: http://link.aip.org/link/?JAP/78/3121/1

[34] J. M. Arias, M. Zandian, S. H. Shin, W. V. McLevige, J. G. Pasko, and R. E. DeWames, "Dislocation density reduction by thermal annealing of hgcdte epilayers grown by molecular beam epitaxy on gaas substrates," *Journal of Vacuum Science & Technology B: Microelectronics and Nanometer Structures*, vol. 9, no. 3, pp. 1646–1650, 1991. [Online]. Available: http://link.aip.org/link/?JVB/9/1646/1

[35] M. Yamaguchi, M. Tachikawa, Y. Itoh, M. Sugo, and S. Kondo, "Thermal annealing effects of defect reduction in gaas on si substrates," *Journal of Applied Physics*, vol. 68, no. 9, pp. 4518–4522, 1990. [Online]. Available: http://link.aip.org/link/?JAP/68/4518/1

[36] S. K. Choi, M. Mihara, and T. Ninomiya, "Dislocation velocities in gaas," *Japanese Journal of Applied Physics*, vol. 16, no. 5, pp. 737–745, 1977. [Online]. Available: http://jjap.jsap.jp/link?JJAP/16/737/

[37] R. A. Wood, J. L. Schmit, H. K. Chung, T. J. Magee, and G. R. Woolhouse, "Summary abstract: Liquid-phase epitaxial growth of (hgcd)te on cd(tese) substrates," *Journal of Vacuum Science & Technology A: Vacuum, Surfaces, and Films*, vol. 3, no. 1, pp. 93–94, 1985. [Online]. Available: http://link.aip.org/link/?JVA/3/93/1

Curriculum Vitae

Stuart B. Farrell graduated from The Field School, Washington, DC in 2001. He received his Bachelor of Science at Lynchburg College in 2006. At Lynchburg College he obtained a triple major in mathematics, physics and philosophy. He was employed as a graduate research assistant at George Mason University while he was pursuing a Masters of Science in Physics, which he obtained in 2008.